ДОКЛАДЫ БГУИР

Выходит два раза в квартал

Научный журнал издается с января 2003 года

Журнал зарегистрирован в Министерстве информации Республики Беларусь, свидетельство о регистрации № 1087 от 23.01.2010 г.

Входит в Перечень научных изданий Республики Беларусь
для опубликования результатов диссертационных исследований,
включен в базу данных Российского индекса научного цитирования (РИНЦ)

Адрес редакции: ул. П. Бровки, 6, к. 326, г. Минск, 220013, Беларусь
Телефон редакции: +375-17-293-88-41
Web-сайт: www.doklady.bsuir.by; e-mail: doklady@bsuir.by

СОДЕРЖАНИЕ

ЭЛЕКТРОНИКА, РАДИОФИЗИКА, РАДИОТЕХНИКА, ИНФОРМАТИКА

Ответственный за выпуск Т.В. МИРОНЕНКО
Корректура и верстка Л.В. КОНДАКОВА
Компьютерный дизайн А.Д. ГУРБО

Подписано в печать 24.12.2021. Формат 60×84 ⅛. Бумага офсетная. Отпечатано на ризографе.
Усл. печ. л. 11,86. Уч.-изд. л. 10,0. Тираж 100 экз. Заказ 209.
Индекс для индивидуальной подписки 00787.
Индекс для ведомственной подписки 007872.

Издатель: учреждение образования «Белорусский государственный университет информатики и радиоэлектроники».
Свидетельство о государственной регистрации средства массовой информации № 1087 от 23.01.2010.

Отпечатано в БГУИР. ЛП № 02330/264 от 24.12.2020. 220013, г. Минск, ул. П. Бровки, 6.

DOKLADY BGUIR

Published twice quarterly

The journal is being published since January, 2003

The journal was registered on January 23, 2010 by the Ministry of Information of the Republic of Belarus in the State Registry of Mass Media, reg. No. 1087.

The journal included in the List of Scientific Editions for Publication of the Results of Dissertation Researches in the Republic of Belarus and in the Database of Russian Science Citation Index (RSCI)

Editor office address:
P. Brovka St., 6, off. 326, Minsk, 220013, Republic of Belarus
Editor office phone number: +375-17-293-88-41
Web-site: www.doklady.bsuir.by; e-mail: doklady@bsuir.by

TABLE OF CONTENTS

ELECTRONICS, RADIOPHYSICS, RADIOENGINEERING, INFORMATICS

http://dx.doi.org/10.35596/1729-7648-2021-19-8-5-9

Original paper

UDC 621.794.61

AB-INITIO SIMULATION OF HYDROGENATED GRAPHENE PROPERTIES

VALENTIN V. MURAV'EV, VALERY M. MISHCHENKA

Belarusian State University of Informatics and Radioelectronics (Minsk, Republic of Belarus)

Submitted 16 November 2021

Abstract. Ab-initio simulation of hydrogenated graphene properties was performed. At present, graphene is considered one of the most promising materials for the formation of new semiconductor devices with good characteristics. Graphene has been the subject of many recent investigations due to its peculiar transport, mechanical and others properties [1]. The chemical modification of graphene named as graphane has recently entered the investigation as a possible candidate to solve problems connected with the lack of a graphene bandgap. Graphane is a compound material consisting of two-dimensional graphene bonded by some atoms of hydrogen. The investigation shows that graphane has the three valley Γ-M-K band structure with the Γ valley, which has the smallest energy gap between the conductivity zone and the valence zone. The calculation of relative electron masses and non-parabolic coefficients in Γ, M and K valleys was performed. Based on the obtained characteristics, it is possible to implement a statistical multi-particle Monte Carlo method to determine the characteristics of electron transfer in heterostructure semiconductor devices. A research on modified graphene structures is important for fundamental science and technological applications in high-speed transistor structures operating in the microwave and very high frequency ranges.

Keywords: graphene, hydrogen, Quantum Espresso, ab-initio method, graphane.

Conflict of interests. The authors declare no conflict of interests.

For citation. Murav'ev V.V, Mishchenka V.M. Ab-initio simulation of hydrogenated graphene properties. Doklady BGUIR. 2021; 19(8): 5-9.

Introduction

A new promising material, graphene, which is a two-dimensional allotropic modification of carbon atoms, has attracted a lot of attention from scientists and researchers. Graphene can be thought of as a single thin layer of graphite, technologically separated from the bulk area of the structure (Fig. 1). Carbon atoms, usually one atomic layer thick, form a hexagonal crystal lattice and are connected via σ- and π-bonds. A number of researchers estimate that this material has high mechanical rigidity and record high thermal conductivity. The high mobility of charge carriers (maximum electron mobility among all known materials) makes it a promising material for use in a wide variety of applications, in particular, as a future basis for nanoelectronics and a possible replacement for silicon in integrated circuits [1]. The lack of a gap in the zone diagram can be solved by developing modified graphene structures by adding a number of atoms, such as hydrogen, fluorine and so on. Developments of modified graphene using hydrogen atoms are already known, one of which is called graphane [2–3]. Graphane is already a three-dimensional structure, in which a two-dimensional layer of carbon atoms is connected with hydrogen atoms, which can be positioned either above or below the layer of carbon atoms. Graphane is a semiconductor, which has a novel

structure and new properties. It is possible to create similar structures using other atoms, such as fluorine or lithium. A research on modified graphene structures will provide practical results for the development of high-speed transistor structures. To this purpose, the main objective of this work is to investigate parameters and characteristics of the hydrogenated graphene by the ab-initio method.

Method and peculiarities of a simulation of hydrogenated graphene properties

Ab-initio calculations have been performed by means of the Quantum Espresso [4] code, using the Perdew-Burke-Ernzerhof (PBE) parametrization of the generalized gradient approximation (GGA). A 40 Ry (1 Ry ≈ 13,605 eV) wave function cutoff and 160 Ry charge density cutoff have been considered. Brillouin zone has been sampled using a 24×24×1 Monkhorst–Pack grid. A 20 bohr (1 bohr ≈ $5{,}29 \cdot 10^{-11}$ cm) layer of vacuum is considered to separate the sheet from its periodical images.

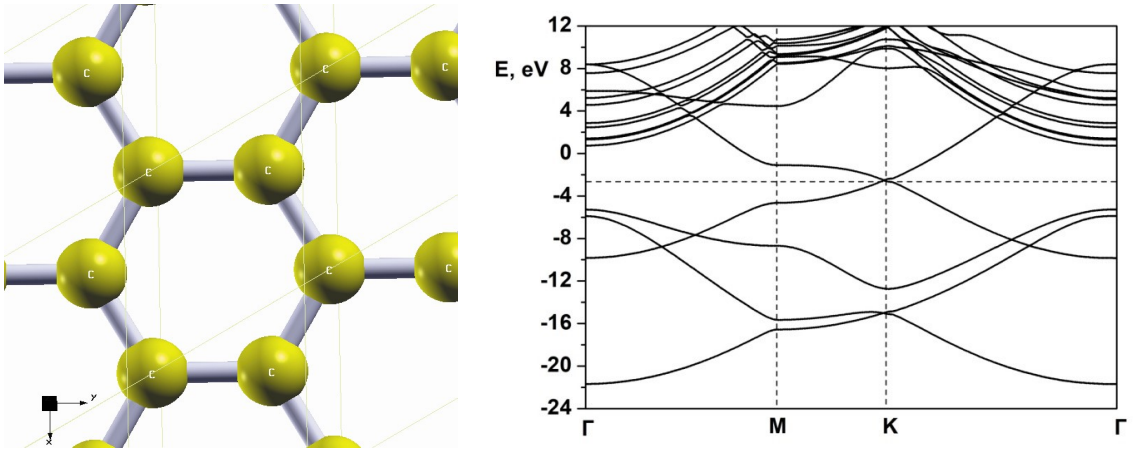

a *b*

Fig. 1. Graphene: *a* – features of arrangement of carbon (C) atoms; *b* – zone diagram

Results of modeling of parameters and characteristics of the hydrogenated graphene by the ab-initio method

Relaxed structures for 100 % and 50 % hydrogenated and fluorinated graphene (from here on H100%, H50%, F100%, and F50%, respectively) are in agreement with the results already shown in the literature [2–3]. We show the results of modeling for the considered H50% and H100% structures in the Fig. 2 and 3.

Fig. 2, *a* shows the peculiarities of the arrangement of carbon (C) and hydrogen (H) atoms and Fig. 2, *b* – the zone diagram in the structure of 50 % hydrogenated graphene (or graphane of C2H1 type). The results are in good agreement with simulation data obtained by the GW (G is the Green function, W is the screened Coulomb potential) method (within 5 % accuracy, according to [3]). All the materials considered, with the exception of a number of modifications using fluorine atoms, are semiconductors and have non-degenerate conduction band minimum at the Γ point. We have extracted the effective mass and other parameters from the results of the density functional theory DFT-GGA simulations. Fig. 3, *a* shows the peculiarities of the arrangement of carbon (C) and hydrogen (H) atoms and Fig. 3, *b* – the zone diagram in the structure of 100 % hydrogenated graphene (or graphane of C2H2 type). From the analysis of these figures, which shows the dependences of the energy values E (eV) on the normalized value of the wave vector k, it is clear that the hydrogenated graphene is characterized by a three-valley Γ-M-K band diagram. Valley Γ is characterized by the smallest energy gap between the conduction and valence bands. When you are modeling the electronic characteristics and parameters of hydrogenated graphene it is necessary to analyze the parameters of all three valleys Γ, M, and K. The analysis of the data presented in Fig. 2 and 3 shows that the C2H2 graphene provides a larger energy gap between the conduction and valence valleys than the C2H1 graphene does.

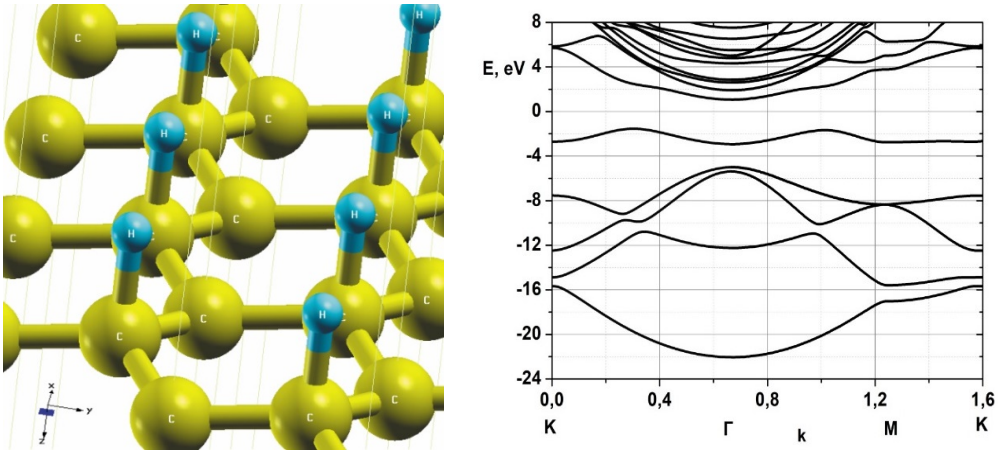

a *b*

Fig. 2. 50 % hydrogenated graphene (graphane of C2H1 type): *a* – features of carbon (C) and hydrogen (H) atoms arrangement of; *b* – zone diagram

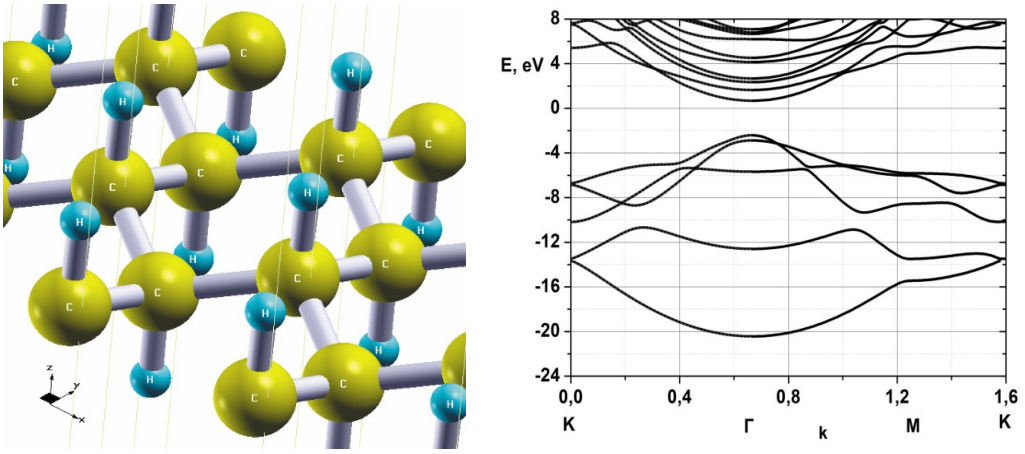

a *b*

Fig. 3. 100% hydrogenated graphene (graphane of C2H2 type): *a* – features of carbon (C) and hydrogen (H) atoms arrangement; *b* – zone diagram

The peculiarities of the total electrostatic potential distribution of $V_{bare} + V_H + V_{xc}$, where V_{bare}, V_H, and V_{xc} are the representation of bare potential, Hartree potential, and exchange-correlation potential, respectively, in the structure of 50 % hydrogenated graphene (C2-H1 graphane) are presented in Fig. 4.

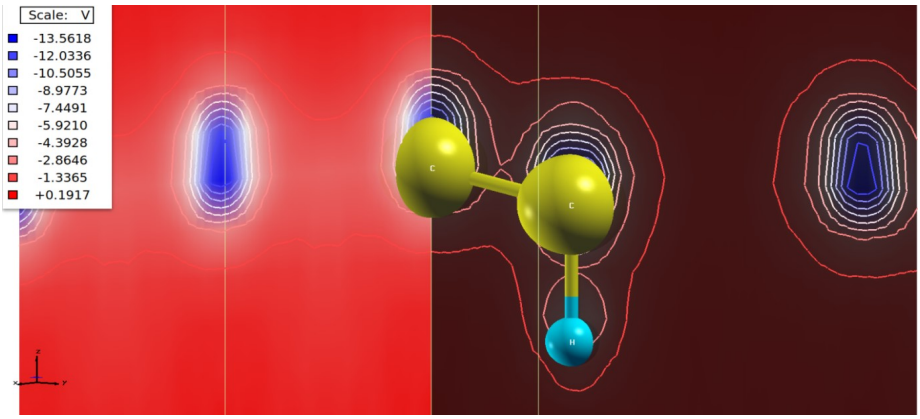

Fig. 4. Peculiarities of $V_{bare} + V_H + V_{xc}$ total electrostatic potential distribution in the structure of 50 % hydrogenated graphene (C2-H1 graphane)

The peculiarities of electrostatic potential distribution of only potential distribution $V_{bare} + V_H$ in the structure of 50 % hydrogenated graphene (graphane) C2-H1 are presented in Fig. 5. A comparison of the modelling results shown in Fig. 4 and 5 allows to estimate the exchange-correlation potential V_{xc}.

Effective electron masses for graphane of C2H1 and C2H2 have been calculated taking into account the value of the energy gap between the conduction and valence bands for the Γ-M-K valleys [5]. Effective electron mass for C2H1 and C2H2 graphane of the Γ-valley equals 0,787 and 0,838, respectively. The calculation of the non-parabolic coefficients for C2H1 and C2H2 materials for the Γ-valley gave the values of 0,0958 eV^{-1} and 0,0521 eV^{-1}, respectively.

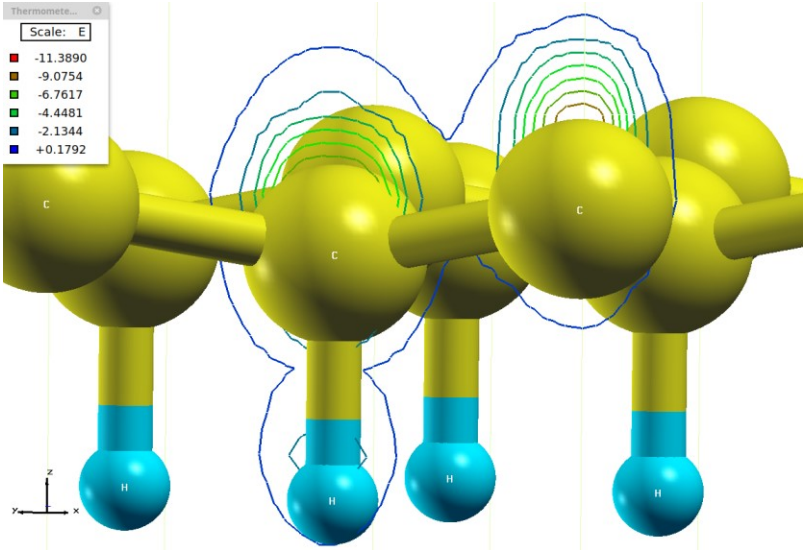

Fig. 5. Peculiarities of $V_{bare} + V_H$ electrostatic potential distribution in the structure of 50 % hydrogenated graphene (C2-H1 graphane)

Conclusion

Ab-initio simulation of hydrogenated graphene properties was performed. Ab-initio calculations have been performed by means of the Quantum Espresso code, using the Perdew-Burke-Ernzerhof parametrization of the generalized gradient approximation GGA.

Basic electrophysical parameters and characteristics of hydrogenated graphene material characterized by Γ-M-K band structure are considered. It is noted that Γ-valley is characterized by the smallest energy gap between conduction and valence zones. The calculated values of the effective electron mass and the non-parabolic coefficients for the Γ-M-K band structure valleys are obtained. Based on the obtained characteristics, it is possible to implement the parameters of hydrogenated graphene in a statistical multi-particle Monte Carlo program to determine the characteristics of electron and hole transfer in heterostructure semiconductor devices.

The investigation of modified graphene with hydrogen and other substances is important for fundamental science and technical applications in high-speed transistor structures operating in the microwave and very high frequency ranges.

References

1. Elias D.C., Nair R.R., Mohiuddin T.M.G., Morozov S.V., Blake P., Halsall M.P., Ferrari A.C., Boukhvalov D.W., Katsnelson M.I., Geim A.K. and Novoselov K.S. *Control of Graphene's Properties by Reversible Hydrogenation: Evidence for Graphane, Science*. 2009;323:610-613.
2. Sahin H., Leenaerts O., Singh S.K. and Peeter F.M. GraphAne: From Synthesis to Applications. *WIRES Computational Molecular Science.* 2015;5(3).
3. Bruzzone S., Fiori G. Ab-initio simulations of deformation potentials and electron mobility in chemically modified graphene and two dimensional hexagonal boron-nitride. *Appl. Phys. Lett*. 2011;99.

4. Giannozzi P., Baroni S., Bonini N., Calandra M., Car R., Cavazzoni C., Ceresoli D., Chiarotti G.L., Cococcioni M., Dabo I. QUANTUM ESPRESSO: a modular and open-source software project for quantum simulations of materials. *J. Phys.: Condens. Matter*. 2009;21(39).
5. Shur M. *Modern devices based on gallium arsenide*. Moscow: Mir; 1991:632.

Authors' contribution

Murav'ev V.V. proposed the idea of investigation of hydrogenated graphene.
Mishchenka V.N. carried out the simulation of hydrogenated graphene properties.

Information about the authors

Murav'ev V.V., Member-Corr. of the National Academy of Sciences of Belarus, PhD., Professor at the Belarusian State University of Informatics and Radioelectronics.

Mishchenka V.N., PhD., Associate Professor at the Belarusian State University of Informatics and Radioelectronics.

Address for correspondence

220013, Republic of Belarus,
Minsk, P. Brovka St., 6,
Belarusian State University
of Informatics and Radioelectronics;
e-mail: mishchenko@bsuir.by;
tel. +375-29-394-55-58; +375-17-293-80-70
Mishchenka Valery Nikolaevich

http://dx.doi.org/10.35596/1729-7648-2021-19-8-10-14

Original paper

UDC 539.143.5

CHARGE PROPERTIES AND CURRENTS IN THE SILICON/NANOPARTICLES OF ZINC OXIDE HETEROSTRUCTURE IRRADIATED BY THE SOLAR LIGHT

ANNA A. KURAPTSOVA, ALEXANDER L. DANILYUK

Belarusian State University of Informatics and Radioelectronics (Minsk, Republic of Belarus)

Submitted 16 November 2021

Abstract. Silicon/zinc oxide heterostructures have shown themselves to be promising for use in photovoltaics. This paper presents the results of modeling the charge properties and currents in a Si/nanosized ZnO particle with different types of conductivity under sunlight irradiation. The simulation was carried out using the Comsol Multiphysics software package. The energy diagrams of the investigated heterostructures were plotted, the charge properties and currents flowing in the structure were investigated, the dependences of the rate of generation of charge carriers on wavelength on the surfaces of silicon, zinc oxide, and at the interface between silicon and zinc oxide, the rate of recombination of charge carriers at various wavelengths of incident radiation was obtained. The regularities of the influence of wavelength of the incident radiation on the charge density and electric potential on the surface of heterostructures have been established. It is shown that the potential on the surface of the p-Si / n-ZnO heterostructure is positive, depends on the wavelength of the incident radiation and reaches the maximum of 0.68 V. For other structures, it is negative and does not depend on the wavelength: n-Si / p-ZnO –0.78 V, p-Si / p-ZnO –0.65 V, n-Si / n-ZnO –0.25 V.

Keywords: nanoparticle; zinc oxide; silicon; heterostructure; charge properties; modeling; photovoltaics.

Conflict of interests. The authors declare no conflict of interests.

Gratitude. This work was supported by the Belarusian Republican Foundation for Fundamental Research (Grant F20MS-027).

For citation. Kuraptsova A.A., Danilyuk A.L. Charge properties and currents in the silicon/nanoparticles of zinc oxide heterostructure irradiated by the solar light. Doklady BGUIR. 2021; 19(8): 10-14.

Introduction

Zinc oxide is a wide-gap (3.37 eV) semiconductor that is used in a variety of fields of photovoltaics, such as photocatalytic water and air purification, photolysis of water, optoelectronics, and gas sensors [1]. Zinc oxide has a number of advantages over other materials used in photocatalysis: low cost, non-toxicity, low reflectance in the solar spectrum, the ability to create low-dimensional structures using chemical etching (amphotericity), resistance to high-energy radiation, flexible change of electrophysical and optical properties by doping with various impurities [2].

The conductivity of zinc oxide depends significantly on the stoichiometric composition of the material. The deviation from the stoichiometric ratio [Zn]:[O] = 1 causes the formation of point defects: interstitial atoms and vacancies of oxygen and zinc atoms. An excess of zinc or oxygen vacancies is a characteristic of the n-type conductivity of ZnO obtained under nonequilibrium conditions or due to the partial transition of oxygen to the gas phase. Moreover, hydrogen atoms [3]

injected into the material during growth or deposition in a hydrogen-containing enviroment or during post-processing of the sample with water solutions can be responsible for the n-type conductivity.

At the same time, attention is now focused on obtaining and studying the properties of the p-type zinc oxide. Obtaining the p-type conductivity is complicated by the presence of natural oxygen vacancies, which act as donor states [4]. Today the following elements are acceptors for ZnO: Zn vacancies; IA group: Li, Na, K; IB group: Cu, Ag, Au; VA group: N, P, As, Sb [5]. On the other hand, much attention is paid to the creation and study of silicon/zinc oxide heterostructures containing ZnO nanoparticles. This is important for the formation of composite materials with a developed surface for photovoltaics.

Charge properties modeling methodic

Modeling of currents, charge properties, and electron-hole processes were carried out using the Comsol Multiphysics package, a two-dimensional diffusion-drift model for calculating current transfer in semiconductors, as well as the Maxwell system of equations. The main properties of silicon [6] and zinc oxide [2, 7–9] used in the simulation are presented in Tab. 1.

Table 1. Material parameters (temperature 300 K)

Parameter	n,p-Si	n,p-ZnO
Bandgap, eV	1.12	3.37
Affinity, eV	4.05	4.3
Permittivity	11.7	8.5
Effective density of states, cm^{-3} *– conduction band* *– valence band*	 $2.8 \cdot 10^{19}$ $1.04 \cdot 10^{19}$	 $4.124 \cdot 10^{18}$ $1.138 \cdot 10^{19}$
Charge carries lifetime, μs	10	$9.7 \cdot 10^{-4}$
Impurity concentration, cm^{-3}	10^{17}	10^{16}
Electron mobility, $cm^2/(V \cdot s)$	1450	200
Hole mobility, $cm^2/(V \cdot s)$	500	50

The real parts of the refractive index for silicon and zinc oxide n(Si) and n(ZnO), as well as the imaginary parts of the refractive index k(ZnO) and k(Si) are given in a table depending on the wavelength [10, 11]. The heterostructure is a zinc oxide nanoparticle with a size of 500×500 nm in a silicon substrate.

Results and discussion

Fig. 1 shows the energy diagrams of heterostructures for various combinations of types of conductivity of a silicon substrate and zinc oxide nanoparticles.

The barrier height for electrons from the silicon side in the n-Si/n-ZnO heterostructure is 0.133 eV, after passing through which, they enter the depletion region for electrons in zinc oxide, thereby creating an excess negative charge at the edge (length ≈ 70 nm) of the oxide nanoparticle zinc. The hole barrier on the zinc oxide side is 0.092 eV. In the n-Si/p-ZnO heterostructure, the barrier for electrons on the silicon side is 0.104 eV, and for holes on the zinc oxide side it is 0.567 eV. For the p-Si/p-ZnO heterostructure, these values are 0.028 eV and 0.57 eV, respectively. For the p-Si/n-ZnO heterostructure, there are no such barriers, it allows electrons generated in silicon and holes generated in zinc oxide to flow freely into another semiconductor.

Fig. 2 shows the dependences of the generation rate G of charge carriers on the wavelength of incident radiation on the surface of a zinc oxide nanoparticle (curve 3), the surface of a silicon substrate (curve 1), and silicon under a zinc oxide nanoparticle under the radiation transmitted through a ZnO nanoparticle (curve 2).

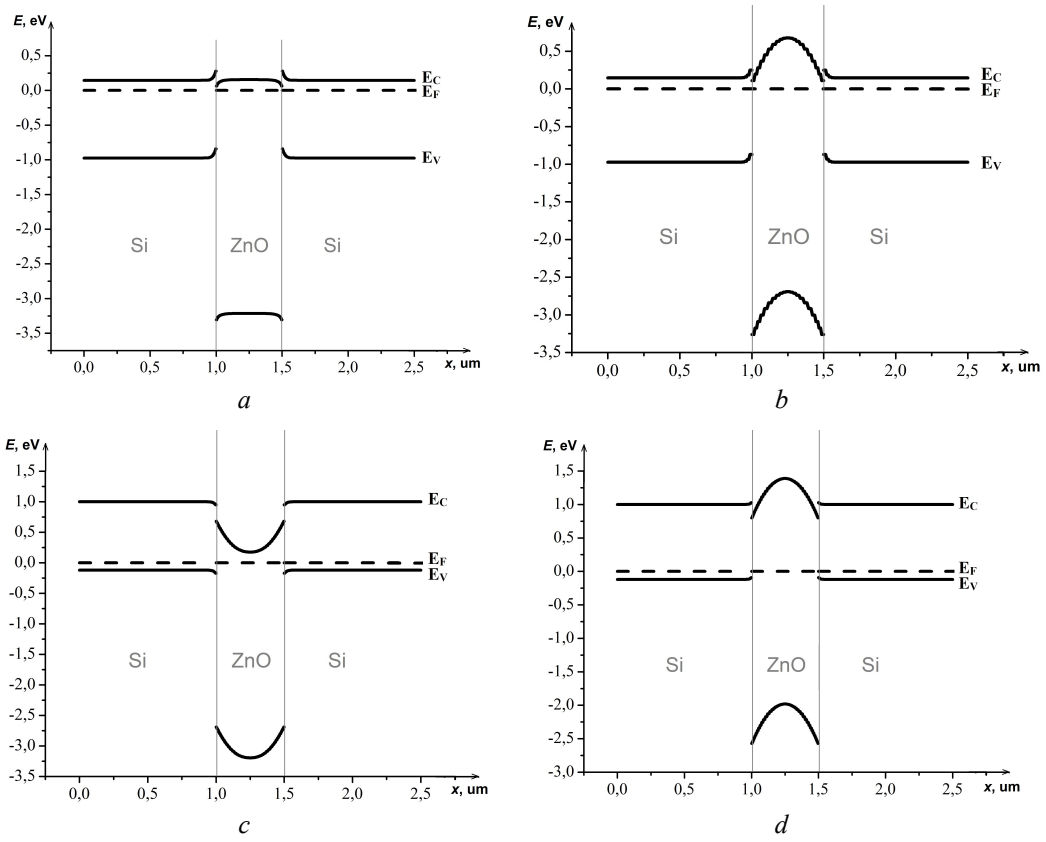

Fig. 1. Energy diagrams of heterostructures: *a* – n-Si/n-ZnO; *b* – n-Si/p-ZnO; *c* – p-Si/n-ZnO; *d* – p-Si/p-ZnO

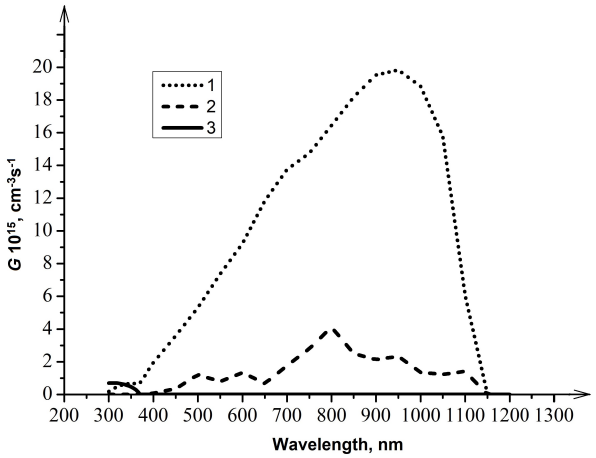

Fig. 2. The rate of generation of charge carriers on the surface of a silicon substrate (1), in silicon after the passage of radiation through a zinc oxide nanoparticle (2), and on the surface of a zinc oxide nanoparticle (3)

Due to the charge carriers redistribution during irradiation an excess electric charge is formed on the surface of heterostructures, the bulk density of which is shown in Fig. 3. The charge density slightly depends on the wavelength of incident radiation in the p-Si/n-ZnO heterostructure on the surface of the ZnO nanoparticle as can be seen from Fig. 3, *b*.

The electric charge is generated on the surface of a zinc oxide nanoparticle and its boundary is with silicon during irradiation, which leads to the potential difference and the emergence of the current of charge carriers generated by the radiation. For the n-Si/n-ZnO structure the potential difference ΔV between the ZnO/Si interface and the ZnO nanoparticle volume is 0.11 V, and for the n-Si/p-ZnO heterostructure it is $\Delta V = 0.63$ V. The difference in values of the negative electric potential V_{surf} on the surface of n-Si/n-ZnO and n-Si/p-ZnO heterostructures (Fig. 4) is the cause. In these structures the observed hole current density from the surface is about 10^{-6} A/m^2. The current density of electrons from the surfaces of the n-Si/p-ZnO and n-Si/n-ZnO heterostructures is

also about 10^{-6} A/m^2. In the p-Si/p-ZnO heterostructure the potential difference ΔV is 0.61 V. It forms the current of holes generated in zinc oxide from the surface of the heterostructure (hole current density is about 10^{-5} A/m^2).

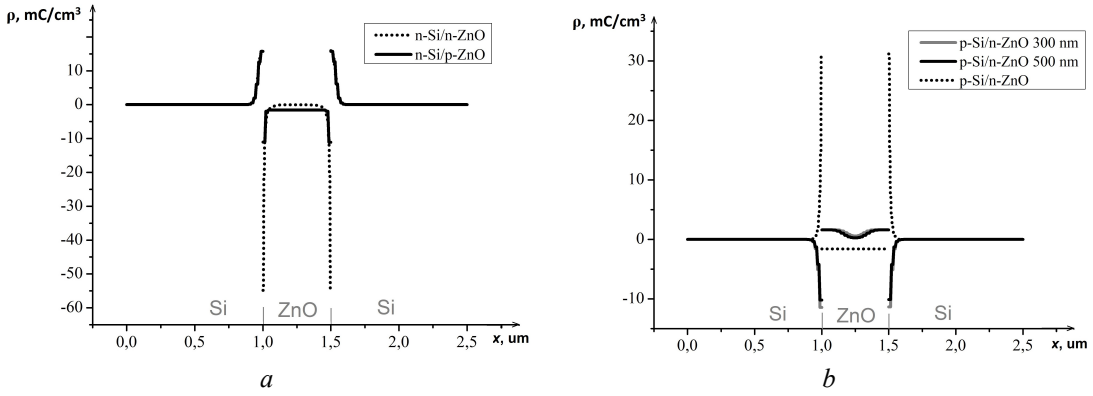

a *b*

Fig. 3. Electric charge density on the surface of the structures: *a* – n-Si/n-ZnO and n-Si/p-ZnO; *b* – p-Si/n-ZnO and p-Si/p-ZnO under irradiation

The electron current density at the surface of the structure at the wavelengths of 300 nm and 350 nm is about 10^{-7} A/m^2. In the p-Si/n-ZnO heterostructure the potential difference ΔV depends on the wavelength of the incident radiation: –0.47 V (λ = 300 nm), –0.43 V (λ = 400 nm), –0.38 V (λ = 500 nm), and –0.35 V (λ = 1000 nm). Due to the absence of potential barriers for electrons from the silicon side at the p-Si/n-ZnO interface (Fig. 1, *c*) the electron current density reaches 7 A/m^2 at the radiation wavelength of 600 nm. The hole current density at the radiation wavelengths of 300 nm and 350 nm on the surface is about 10^{-6} A/m^2.

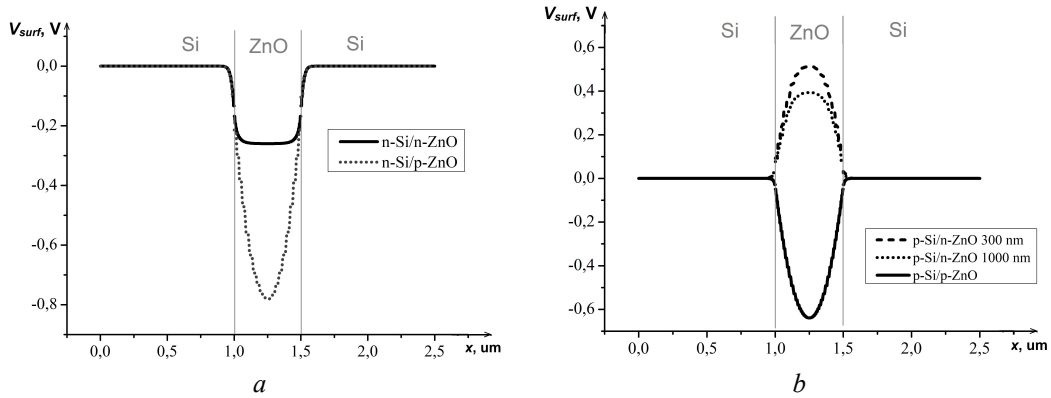

a *b*

Fig. 4. Electric potential on the surface of structures: *a* – n-Si/n-ZnO and n-Si/p-ZnO; *b* – p-Si/n-ZnO and p-Si/p-ZnO at different radiation wavelengths

The positive electric potential depends on the wavelength of the incident radiation and occurs only in the p-Si/n-ZnO heterostructure. Its value reaches 0.68 V in the absence of incident radiation and decreases in the presence of radiation by 0.06 V at the wavelength of 300 nm by 0.1 V at λ = 400 nm, by 0.15 V at λ = 500 nm, and by 0.18 V at λ = 1000 nm. In other cases, the potential on the surface of a zinc oxide nanoparticle is negative, but in the n-Si/p-ZnO structure, it is higher in modulus (–0.78 V) than in the n-Si/n-ZnO structures (–0.25 V) and p -Si/p-ZnO (–0.65V).

Conclusions

The simulation of the charge properties and currents in a zinc oxide nanoparticle in silicon heterostructures for the cases of n- and p-types of conductivity demonstrated differences in the electric charge and potential on the surface of heterostructures without significant differences depending on the wavelength of incident radiation. It is shown that the silicon/p-type zinc oxide nanoparticle heterostructure provides a negative potential and a negative surface charge on the surface of a zinc

oxide nanoparticle regardless of the wavelength of the solar radiation. It opens up additional possibilities for the photocatalytic use of zinc oxide in a wider emission spectrum than its own absorption spectrum. Achieving stable p-type conductivity of zinc oxide opens up many possibilities for creating optoelectric devices based on wide gap semiconductor materials. This will require better control over the natural n-type conductivity of zinc oxide which can compensate acceptor impurities.

References

1. Vorobyeva N.A., Rumyantseva M.N., Forsh P.A., Gaskov A.M. Conductivity of nanocrystalline ZnO(Ga). *Semiconductors*. 2013;47(5):650–654. DOI: 10.1134/S1063782613050242.
2. Özgür U., Allivov Ya. I., Lui C., Teke A., Reshchnikov M. A., Doğan S., Avrutin V., Cho S.-J., Morkoç H. A comprehensive review of ZnO materials and devices. *Journal of applied physics.* 2005;98(4):041301-041403. DOI: 10.1063/1.1992666.
3. Van de Walle C.G. Hydrogen as a Cause of Doping in Zinc Oxide. *Physical review letters*. 2000;85(5):1012-1015. DOI: 10.1103/PhysRevLett.85.1012.
4. Tsay C.Y., Chiu W.Y. Enhanced Electrical Properties and Stability of P-Type Conduction in ZnO Transparent Semiconductor Thin Films by Co-Doping Ga and N. *Coatings*. 2020;10(11):1069-1081. DOI: 10.3390/coatings10111069.
5. Mosca M., Macaluso R., Caruso F., Lo Muzzo V., Calì C. The p-type doping of ZnO: Mirage or reality? *Advances in Semiconductor Research: Physics of Nanosystems, Spintronics and Technological Applications.* New York: Nova Science Publishers Inc. 2014:245-282.
6. Sze S.M., Kwok K.Ng. *Physics of Semiconductor Devices.* 3rd edition. Hoboken: John Wiley & Sons; 2006.
7. Gupta V., Sreenivas K. *Chapter 4 Pulsed Laser Deposition of Zinc Oxide (ZnO).* In: Jagadish C., Pearton S., editors. *Zinc Oxide Bulk, Thin Films and Nanostructures.* Oxford: Elsevier Science & Technology; 2006.
8. Coleman V.A., Jagadish C. Chapter 1 Basic Properties and Applications of ZnO. *Zinc Oxide Bulk, Thin Films and Nanostructures.* Oxford: Elsevier Science & Technology; 2006.
9. Zhang An, Zhao Xiao-Ru, Duan Li-Bing, Liu Jin-Ming, Zhao Jian-Lin. Numerical study on the dependence of ZnO thin-film transistor characteristics on grain boundary position. *Chinese Physics B.* 2011;20(5):057201-057205. DOI: 10.1088/1674-1056/20/5/057201.
10. Green M.A. Self-consistent optical parameters of intrinsic silicon at 300K including temperature coefficients. *Solar Energy Materials and Solar Cells.* 2008;92(11):1305-1310. DOI: 10.1016/j.solmat.2008.06.009.
11. Aguilar O., de Castro S., de Godoy M., Dias M. Optoelectronic characterization of $Zn_{1-x}Cd_xO$ thin films as an alternative to photonic crystals in organic solar cells. *Optical Materials Express.* 2019;9(9):3638-3648.

Authors' contribution

Kuraptsova A.A justified the choice of physical parameters, performed numerical solutions of the current transport equations and participated in the interpretation of the results.

Danilyuk A.L. defined the tasks that needed to be solved during the research and participated in the interpretation of the results.

Information about the authors

Kuraptsova A.A., Postgraduate student at the Department of Micro- and Nanoelectronics of the Belarusian State University of Informatics and Radioelectronics.

Danilyuk A.L., PhD., Associate Professor, Associate Professor at the Department of Micro- and Nanoelectronics of the Belarusian State University of Informatics and Radioelectronics.

Address for correspondence

220013, Republic of Belarus,
Minsk, P. Brovka St., 6,
Belarusian State University
of Informatics and Radioelectronics;
tel. +375-17-293-22-24;
e-mail: anku21qwerty@gmail.com
Kuraptsova Anna Andreevna

http://dx.doi.org/10.35596/1729-7648-2021-19-8-15-19

Original paper

UDC 535.343:541.1

MODELING OF OPTICAL PROPERTIES OF HYBRID METAL-ORGANIC NANOSTRUCTURES

ALINA N. PONYAVINA, KATSIARYNA A. BARBARCHYK, ANATOLY D. ZAMKOVETS, SERGEY A. TIKHOMIROV

B.I. Stepanov Institute of Physics of the National Academy of Sciences of Belarus (Minsk, Republic of Belarus)

Submitted 16 November 2021

Abstract. To model spectral characteristics of hybrid metal-organic nanostructures, the extended Mie theory was used, which makes it possible to calculate the extinction efficiency factor (Q_{ext}) and the scattering efficiency factor in the near zone (Q_{NF}) of two-layer spherical particles placed in an absorbing matrix. Two-layer plasmon nanospheres consisting of a metallic core (Ag, Cu) coated with dielectric shells and located into the copper phthalocyanine (CuPc) matrix were considered. The influence of dielectric shell thickness and refractive index on the characteristics of the surface plasmon resonance of absorption (SPRA) was studied. The possibility of the SPRA band tuning by changing the optical and geometrical parameters of dielectric shells was shown. It was established that dielectric shells allow to shift the surface plasmon resonance band of plasmonic nanoparticles absorption both to short- and long-wavelength spectral range depending on the relation between shell and matrix refractive indexes.

Keywords: surface plasmon resonance, hybrid nanostructures.

Conflict of interests. The authors declare no conflict of interests.

Gratitude. The work was partially supported by the Belarusian Republican Foundation for Basic Research (grant № F20EA-006).

For citation. Ponyavina A.N., Barbarchyk K.A., Zamkovets A.D., Tikhomirov S.A. Modeling of optical properties of hybrid metal-organic nanostructures. Doklady BGUIR. 2021; 19(8): 15-19.

Introduction

Hybrid nanostructures which include both plasmonic and organic components are now under intensive investigation because of their great perspectives for the development and creation of effective modern nanophotonics, nanoplasmonics, and nanoelectronics devices [1, 2]. Among hybrid nanostructures there are ultradisperse plasmonic nanocomposites that consist of metal-containing nanoparticles embedded in a matrix of organic semiconductors. The unique properties of plasmonic nanoparticles are connected with the surface plasmon resonance of absorption (SPRA) and with a strong increase of electromagnetic fields near the plasmonic nanoparticle surface in this spectral region. Optical properties of densely packed arrays of plasmonic nanoparticles depend on interparticle electrodynamic coupling associated with near-field scattering and coherent reirradiation by particles of each other. The extent of the near-field interparticle coupling is connected with the spectral position of the SPRA maxima and may be regulated by a special choice of a metal

nanoparticle material and concentration as well as their morphological parameters such as nanoparticle size, shape, and its internal structure. The promising way to control the internal structure of plasmonic nanoparticles and in such way the SPRA spectra and the near-field scattering efficiency is an application of so-called two-layer nanoparticles with a metal core and a dielectric shell (M@D). Modeling and investigation of the optical properties of the M@D plasmonic nanoparticles was made based on the example of a spherical silver or copper core covered by a dielectric shell and embedded into a matrix of copper phthalocyanine.

Method

To model the spectral characteristics of such nanostructures, the extended Mie theory was used, which made it possible to calculate the extinction efficiency factor (Q_{ext}) and the scattering efficiency factor in the near zone (Q_{NF}) of two-layer spherical particles placed in an absorbing matrix [3, 4]:

$$Q_{ext} = \frac{4m_i^2}{m_r\left[1+e^{\eta}(\eta-1)\right]}\mathrm{Re}\left\{\frac{1}{m_i - im_r}\sum_{n=1}^{\infty}\left[\left(2n+1\right)\left(\psi_n^*\psi_n' - \psi_n\psi_n'^* + b_n\psi_n'^*\xi_n + b_n^*\psi_n\xi_n'^* - a_n\psi_n^*\xi_n' - a_n^*\psi_n'\xi_n^*\right)\right]\right\},$$

$$Q_{NF} = \frac{\left(4\pi m_i R\right)^2}{\lambda_0^2\left[1+e^{\eta}(\eta-1)\right]}\sum_{n=1}^{\infty}\left\{\left|a_n\right|^2\left[\left(n+1\right)\left|h_{n-1}\right|^2 + n\left|h_{n+1}\right|^2\right] + \left(2n+1\right)\left|b_n\right|^2\left|h_n\right|^2\right\}.$$

Here λ_0 is the wavelength of the incident radiation, $m = m_r - im_i$ is complex refractive index of the matrix, a_n, b_n – Mie coefficients, a – particle radius, $\eta = 4\pi a m_i / \lambda_0$. Riccati-Bessel functions and their derivatives (ψ_n, ξ_n, ψ_n', ξ_n'), as the spherical Hankel function of the first kind of order h_n depend on the diffraction parameter $\rho = 2\pi a/\lambda_0$. In the case of two-layer spherical particles, the Mie coefficients are functions of the complex refractive indices of the nucleus and shell, the diffraction parameters of the particle as a whole and its nucleus.

The Q_{ext} value determines the attenuation of incident light beam intensity caused by the absorption in the particle and scattering on it. The Q_{NF} factor characterizes an increase in the intensity of the field along the surface of a sphere of radius R when nanoparticles are introduced into the center of this sphere.

Results

The spectral dependences of Q_{ext} and Q_{NF} factors for two-layer plasmon nanospheres consisting of a metallic core (Ag, Cu) coated with a dielectric shell, placed in the organic semiconductor matrix of copper phthalocyanine (CuPc) are shown in Fig. 1–3. The near-field scattering efficiency factor was calculated for $R = R_2$, where R_2 is an external radius of a two-layer nanosphere. The Ag and Cu optical constants, used at the calculations, are given in [5].

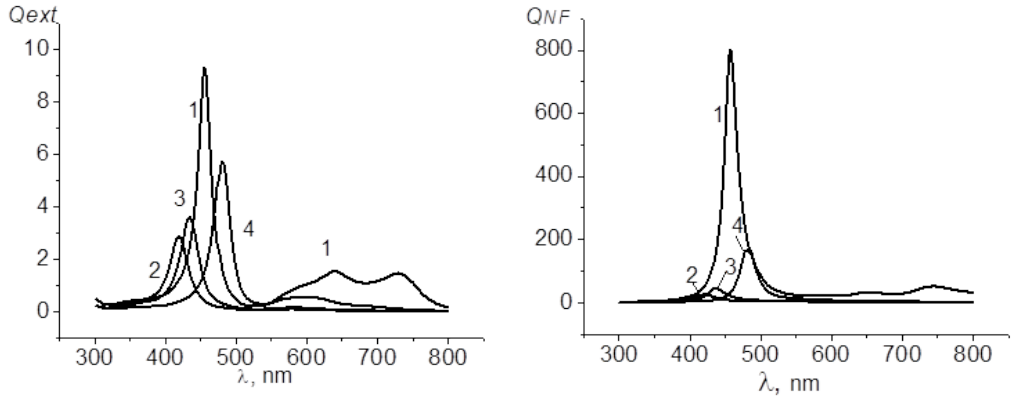

a *b*

Fig. 1. Spectral dependence of the extinction efficiency factor (*a*) and the near-field scattering efficiency factor (*b*) for silver nanoparticle (curve 1) and two-layer nanospheres with silver core and dielectric shell (curves 2–4) placed in the CuPc matrix. The radius of the silver core R_1 = 10 nm, the outer radius of the two-layer sphere R_2 = 15 nm. Refractive index of a dielectric shell n = 1.35, 1.5, 2.0 (curves 2, 3, 4 correspondingly)

As can be seen from Fig. 1, the maximum of the SPRA band of a homogeneous silver nanosphere with a radius $R_1 = 10$ nm placed in the CuPc matrix is located near the wavelength of 450 nm. In this spectral region, copper phthalocyanine absorbs insignificantly and its complex refractive index varies from $m_{CuPc} = 2 - i\ 0.12$ for $\lambda = 400$ nm to $m_{CuPc} = 1.6 - i\ 0.02$ for $\lambda = 500$ nm. The CuPc absorption band maxima is located in the wavelength range of 370, 624, and 690 nm; the value of $m_{CuPc} = 1.7 - i\ 0.06$ for $\lambda = 450$ nm [3]. As it is known, the presence of a shell on a small metal ball shifts the Frelich frequency, which determines the spectral position of the SPRA band dipole maximum [6].

The comparison of the curves 2–4 shows that at fixed core sizes and shell thicknesses the SPRA spectral shift may depend on the shell refractive index n. Using the Ag sphere nanoparticles in the CuPc matrix as an example, one can see that on covering the Ag core by a dielectric shell with $n < 1.7$ the SPRA band moves to a short-wavelength region relatively to the SPRA band of a homogeneous silver nanosphere (see curves 2, 3). On covering by the dielectric shell with $n > 1.7$, on the other hand, the SPRA band maximum moves to the long-wavelength region of the spectrum (see curve 4). This fact allows to conclude that both the value and the direction of the SPRA band spectral shift depend on the relative refractive index of the dielectric shell into the matrix surrounding the two-layer nanoparticle.

Fig. 2 demonstrates the possibility of controlling the value of the spectral shift by changing the thickness of the shell on the metal core. First of all, we note that the maximum of the SPRA band for a homogeneous silver nanosphere $R_1 = 25$ nm is shifted by the wavelength $\lambda_{max} = 480$ nm due to the size effects. Herewith, $Q_{ext} = 12.5$, $Q_{NF} = 320$ at the maximum of the SPRA band. The application of quartz shells, for which the refractive index is $n \approx 1.45$ in the spectral range 400 nm – 600 nm, leads to a short-wave shift λ_{max}, which increases with the quartz shell thickness increasing. As can be seen from Fig. 2, *a*, the spectral position of the SPRA maximum varies from 470 nm for a shell with a thickness of 5 to 450 nm for a shell with a thickness of 25 nm. For a given $R_1 = 25$ nm of silver nanoparticles placed in CuPc, the available range of variation λ_{max},due to the changes in the thickness of the quartz shell, is 480–440 nm. The values of Q_{ext} and Q_{NF} in the maximum of the SPRA band decrease with the quartz shell thickness increase.

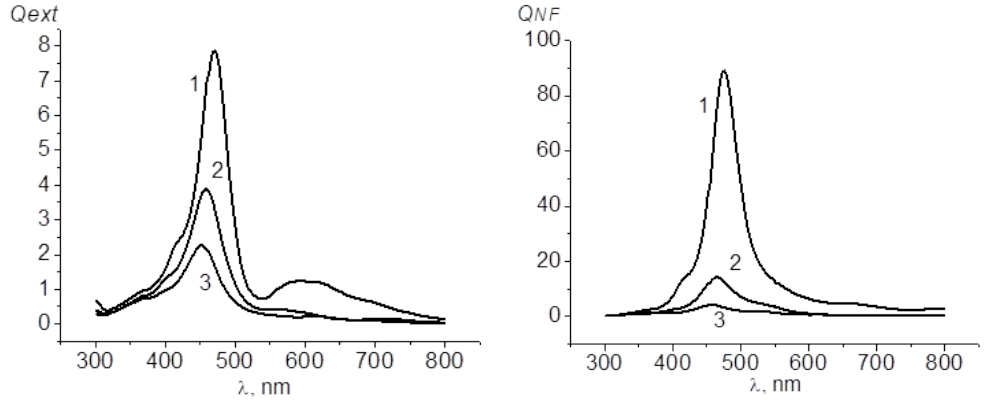

a *b*

Fig. 2. Spectral dependence of the extinction efficiency factor (*a*) and the near-field scattering efficiency factor (*b*) for two-layer Ag @SiO_2 nanospheres placed in the CuPc matrix. The radius core $R_1 = 25$ nm, the outer radius of the two-layer sphere $R_2 = 30$ nm (curve 1), 40 nm (curve 2), 50 nm (curve 3)

Comparison of the data shown in Fig. 1 and 2 allows us to evaluate the effect of the metal core size on the SPRA band characteristics and the amplification of the scattered field near the two-layer plasmon nanoparticle Ag@SiO_2 placed in the CuPc matrix. As it was already noted, the growth of the silver core radius from 10 to 25 nm leads to a long-wave shift of the SPRA band of the homogeneous silver nanosphere from 450 to 480 nm, as well as to the increase in the Q_{ext} values in the maximum of the SPRA band (from $Q_{ext} = 9.3$ to $Q_{ext} = 12.5$). It is interesting to note that Q_{NF} decreases at the maximum of the SPRA band (from $Q_{NF} = 800$ to $Q_{NF} = 320$).

Fig. 3 shows the results of calculations for Cu@SiO_2 two-layer nanoparticles placed in the CuPc matrix. Comparison of Fig. 2 and 3 allows to estimate the effect of a plasmonic

nanoparticle material on the ability to control the characteristics of their SPRA band by applying dielectric shells to the surface of metal nuclei. Unlike silver, copper has strong interband absorption.

Therefore, surface plasmon resonances in copper nanoparticles are less intense, and the SPRA bands are characterized by a large half-width. Besides, the peculiarities of the dispersion of the Cu and CuPc refractive indices lead to the possibility of the manifestation of two wide overlapping SPRA bands in the spectral range of 400–700 nm, with maxima $\lambda_{max} \approx 480$ nm and $\lambda_{max} \approx 580$ nm. As it can be seen from Fig. 3, when quartz shells are applied to a copper core with $R_1 = 25$ nm, the SPRA bands are even more blurred. At the same time, the maximum attenuation is realized in the region of 460–540 nm.

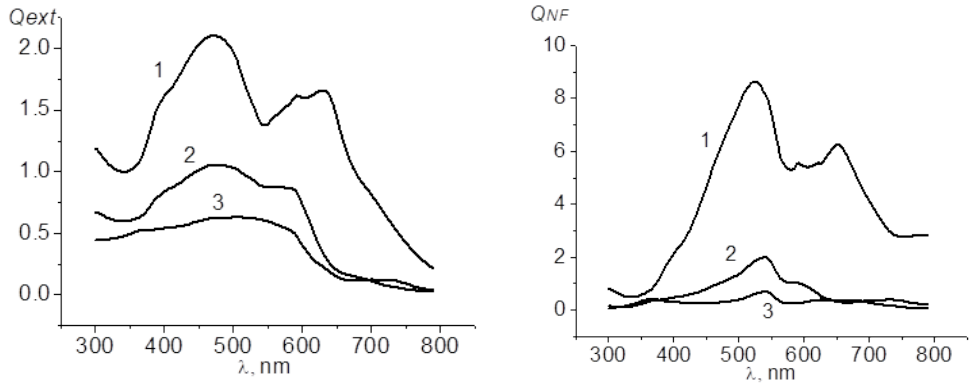

Fig. 3. Spectral dependence of the extinction efficiency factor (*a*) and the near-field scattering efficiency factor (*b*) for two-layer Cu@SiO_2 nanospheres placed in the CuPc matrix. The radius of the copper core $R_1 = 25$ nm, the outer radius of the two-layer sphere $R_2 = 30$ nm (curve 1), 40 nm (curve 2), 50 nm (curve 3)

Conclusion

The results of numerical simulations show that the attenuation spectra of hybrid metal-organic nanostructures, as well as the near field effects at the spectral range of absorption bands of organic component, can be regulated by changing the plasmonic nanoparticle material, their size or shell refractive index and thickness. As one can see, a dielectric shell allows to shift the surface plasmon resonance band of plasmonic nanoparticles absorption both to short- and long-wavelength spectral range depending on the relation between shell and matrix refractive indexes. However, for cases under consideration, the appearance of dielectric shells on the plasmonic core leads to strong decrease of the Q_{ext} *and* Q_{NF} values. Besides, the degree of near-field interactions with dense packaging can be regulated by the choice of the matrix in which the nanoparticles are placed.

References

1. Lepeshov S., Krasnok A., Belov P., Miroshnichenko A. Hybrid Nanophotonics. *Physics Uspekhi*. 2018;188(11):1137-1154.
2. Zamkovets A.D., Aksiment'eva E.I., Ponyavina A.N. Spectral manifestation of surface plasmon resonance in polyparaphenylene–silver nanostructures. *J. of Optical Technology*. 2011;78(2):84-87.
3. Sudiarta I.W., Chylek P. Mie scattering formalism for spherical particles embedded in an absorbing medium. *J. Opt. Soc. Am. A*. 2001;18:1275-1278.
4. Dunich R.A., Ponyavina A.N., Filippov V.V. Local field enhancement near spherical nanoparticles in absorbing media. *J. Appl. Spectr.* 2009;76:705-710.
5. Palik E.D. *Handbook of Optical Constants of Solids*. Orlando: Academic Press Inc.; 1985.
6. Kreibig U., Volmer M. *Optical Properties of Metal Clusters. Springer-Verlag*. Berlin; 1995.

Authors' contribution

Ponyavina A.N. proposed the method for modeling, made numerical simulation.
Barbarchyk K.A. made numerical simulation, prepared the manuscript.
Zamkovets A.D. chose the objects for the investigation.
Tikhomirov S.A. performed the task for the study.

Information about the authors

Ponyavina A.N., D.Sc., Principal Researcher at the Center of Photonics of Atoms and Molecules Structures of B.I. Stepanov Institute of Physics of the National Academy of Sciences of Belarus.

Barbarchyk K.A., Researcher at the Center of Photonics of Atoms and Molecules Structures of B.I. Stepanov Institute of Physics of the National Academy of Sciences of Belarus.

Zamkovets A.D., PhD., Leading Researcher at the Center of Photonics of Atoms and Molecules Structures of B.I. Stepanov Institute of Physics of the National Academy of Sciences of Belarus.

Tikhomirov S.A., D.Sc., Corresponding Member, Scientific Head of the Center of Photonics of Atoms and Molecules Structures of B.I. Stepanov Institute of Physics of the National Academy of Sciences of Belarus.

Address for correspondence

220072, Republic of Belarus,
Minsk, Nezavisimosti Ave., 68-2,
B.I. Stepanov Institute of Physics
of the National Academy of Sciences of Belarus;
tel. +375-17-270-87-53;
e-mail: kananovich.ek@gmail.com
Barbarchyk Katsiaryna Alexandrovna

http://dx.doi.org/10.35596/1729-7648-2021-19-8-20-25

Original paper

UDC 530.145:538.915:538.958

ENERGY LEVELS OF AN ELECTRON IN A CIRCULAR QUANTUM DOT IN THE PRESENCE OF SPIN-ORBIT INTERACTIONS

ALEXANDR V. BARAN, VLADIMIR V. KUDRYASHOV

B.I. Stepanov Institute of Physics of the National Academy of Science of Belarus (Minsk, Republic of Belarus)

Submitted 17 November 2021

Abstract. The two-dimensional circular quantum dot in a double semiconductor heterostructure is simulated by a new axially symmetric smooth potential of finite depth and width. The presence of additional potential parameters in this model allows us to describe the individual properties of different kinds of quantum dots. The influence of the Rashba and Dresselhaus spin-orbit interactions on electron states in quantum dot is investigated. The total Hamiltonian of the problem is written as a sum of unperturbed part and perturbation. First, the exact solution of the unperturbed Schrödinger equation was constructed. Each energy level of the unperturbed Hamiltonian was doubly degenerated. Further, the analytical approximate expression for energy splitting was obtained within the framework of perturbation theory, when the strengths of two spin-orbit interactions are close. The numerical results show the dependence of energy levels on potential parameters.

Keywords: circular quantum dots, confinement potential, spin-orbit interactions, energy levels.

Conflict of interests. The authors declare no conflict of interests.

For citation. Baran A.V., Kudryashov V.V. Energy levels of an electron in a circular quantum dot in the presence of spin-orbit interactions. Doklady BGUIR. 2021; 19(8): 20-25.

Introduction

The motion of an electron in an inner layer of a double semiconductor heterostructure is usually treated as two-dimensional in the (x, y) plane. In addition, the planar motion is also restricted if an electron is placed in a quantum dot localized in the middle layer of heterostructure. The Rashba V_R [1] and Dresselhaus V_D [2] interactions are presented by the formulas

$$V_R = \alpha_R(\sigma_x p_y - \sigma_y p_x)/\hbar, \quad V_D = \alpha_D(\sigma_x p_x - \sigma_y p_y)/\hbar, \tag{1}$$

where σ_x and σ_y are the standard Pauli spin-matrices. The strengths of these interactions depend on the materials used. The contributions of two spin-orbit interactions can be measured within various experimental methods [3, 4]. In the general case the whole spin-orbit interaction has the form $V_R + V_D$. At the same time, considerable attention is paid to the special case [3, 5, 6], when the spin-orbit interactions of Rashba and Dresselhaus have equal strength $\alpha_R = \alpha_D$. It can be experimentally achieved due to the fact that the Rashba interaction strength can be controlled by an external electric field, and the Dresselhaus interaction strength can be varied by changing the width of quantum well along the z axis [3, 7].

As a rule, circular quantum dots are simulated with the help of axially symmetric confinement potentials $V(x,y)=V(\rho)$, where $\rho=\sqrt{x^2+y^2}$. In [8, 9], a simple but sufficiently adequate rectangular potential of finite depth was proposed. This model with a discontinuous potential describes the main properties of circular quantum dots but without taking into account the individual characteristics. In [10], the smooth confinement potential of a new type which has finite depth and width was applied in the case of equal strengths $\alpha_R=\alpha_D$. The presence of additional potential parameters allows us to simulate different kinds of circular quantum dots. In the actual paper, we use this potential in order to calculate the energy levels of electron for unequal but close strengths $\alpha_R\neq\alpha_D$.

Methods and results

The circular quantum dot of radius ρ_0 is described by means of the confinement potential $V(\rho)=V_0 v(r)$, where V_0 is the depth of the potential well. The function $v(r)$ depends on ratio $r=\rho/\rho_0$ in the following way

$$v(r)=\begin{cases}0, & 0<r<g,\\ v_1(r), & g<r<s,\\ v_2(r), & s<r<1,\\ 1, & r>1.\end{cases} \tag{2}$$

The functions $v_1(r)$ and $v_2(r)$ have the following forms:

$$v_1(r)=d_1\left(r-\frac{g^2}{r}\right)^2,\quad d_1=\frac{1}{2}\frac{(1+s^2)}{(1-g^2)(s^2-g^2)}, \tag{3}$$

$$v_2(r)=1-d_2\left(r-\frac{1}{r}\right)^2,\quad d_2=\frac{1}{2}\frac{(g^2+s^2)}{(1-g^2)(1-s^2)}. \tag{4}$$

The parameters g and s change within ranges $0<g<1$ and $g<s<1$. The function $v(r)$ and its first derivative are continuous in the inflection points $r=g$, $r=s$ and $r=1$.

The total Hamiltonian of the problem can be written as a sum $H=H_0+H_1$, where

$$H_0=\frac{p_x^2+p_y^2}{2M_{eff}}+\frac{(\alpha_R+\alpha_D)}{2\hbar}(\sigma_x-\sigma_y)(p_x+p_y)+V(\rho), \tag{5}$$

$$H_1=\gamma\frac{(\alpha_R+\alpha_D)}{2\hbar}(\sigma_x+\sigma_y)(p_y-p_x),\quad \gamma=\frac{\alpha_R-\alpha_D}{\alpha_R+\alpha_D}, \tag{6}$$

M_{eff} is the effective electron mass which characterizes the motion in a semiconductor.

We shall solve the full Schrödinger equation $H\Psi=E\Psi$ in two stages. First, we obtain an exact solution of the unperturbed Schrödinger equation $H_0\Psi_0=E_0\Psi_0$ and then we shall take into account the perturbation H_1 within the framework of the perturbation theory.

By analogy with [10] it is easy to show that the required solutions of the unperturbed Schrödinger equation admit a factorization

$$\Psi_0^{\pm}(x,y)=\frac{1}{\sqrt{2}}\begin{pmatrix}1\\ \pm e^{-i\pi/4}\end{pmatrix}\exp\left(\mp i\frac{(\alpha_R+\alpha_D)M_{eff}(x+y)}{\sqrt{2}\hbar^2}\right)e^{im\phi}w(\rho), \tag{7}$$

where $m=0,\pm1,\pm2,\ldots$ is the angular momentum quantum number. Here we use the polar coordinates ρ,ϕ ($x=\rho\cos\phi, y=\rho\sin\phi$).

Introducing dimensionless quantities

$$e_0 = \frac{2M_{eff}\rho_0^2}{\hbar^2}E_0, \quad v_0 = \frac{2M_{eff}\rho_0^2}{\hbar^2}V_0, \quad a = \frac{M_{eff}\rho_0}{\hbar^2}(\alpha_R + \alpha_D), \tag{8}$$

we get the radial equation

$$\frac{d^2w}{dr^2} + \frac{1}{r}\frac{dw}{dr} - \frac{m^2w}{r^2} + \left(e_0 + a^2 - v_0 v(r)\right)w = 0. \tag{9}$$

It is seen that the wave function depends only on the combination $e_0 + a^2$.

In the region $0 < r < g$, the finite at $r \to 0$ solution of radial equation is expressed via the Bessel function [11] by means of the formula $w_1(r) = J_m\left(\sqrt{e_0 + a^2}\, r\right)$.

In the region $g < r < s$, it is simple to obtain two solutions in terms of the confluent hypergeometric functions [11]:

$$w_2(r) = r^B \exp\left(-\frac{\sqrt{d_1 v_0}}{2}r^2\right) M\left(A, 1+B, \sqrt{d_1 v_0}\, r^2\right), \tag{10}$$

$$w_3(r) = r^B \exp\left(-\frac{\sqrt{d_1 v_0}}{2}r^2\right) U\left(A, 1+B, \sqrt{d_1 v_0}\, r^2\right), \tag{11}$$

where

$$A = \frac{1+B}{2} - \frac{e_0 + a^2 + 2d_1 g^2 v_0}{4\sqrt{d_1 v_0}}, \quad B = \sqrt{m^2 + d_1 g^4 v_0}. \tag{12}$$

In the region $s < r < 1$, it is easy to show that two solutions are

$$w_4(r) = \frac{w_+(r) + w_-(r)}{2}, \quad w_5(r) = \frac{w_+(r) - w_-(r)}{2i}, \tag{13}$$

$$w_\pm(r) = r^{B_\pm} \exp\left(\mp\frac{\sqrt{-d_2 v_0}}{2}r^2\right) M\left(A_\pm, 1+B_\pm, \pm\sqrt{-d_2 v_0}\, r^2\right), \tag{14}$$

where

$$A_\pm = \frac{1+B_\pm}{2} \pm \frac{v_0 - e_0 - a^2 + 2d_2 v_0}{4\sqrt{-d_2 v_0}}, \quad B_\pm = \pm\sqrt{m^2 - d_2 v_0}. \tag{15}$$

Note that the functions $w_4(r)$ and $w_5(r)$ are real if $d_2 v_0 > m^2$.

In the region $r > 1$, the decreasing solution is expressed via the modified Bessel function [11] with the help of the formula $w_6(r) = K_m\left(\sqrt{v_0 - e_0 - a^2}\, r\right)$.

Thus, we obtain the radial wave function

$$w(r) = \begin{cases} c_1 w_1(r), & 0 < r < g, \\ c_2 w_2(r) + c_3 w_3(r), & g < r < s, \\ c_4 w_4(r) + c_5 w_5(r), & s < r < 1, \\ c_6 w_6(r), & r > 1. \end{cases} \tag{16}$$

The coefficients c_i are found from the continuity condition for function $w(r)$ and its first derivative $w'(r)$ at three inflection points $r = g$, $r = s$, and $r = 1$. The fulfilment of this condition and the continuity of the potential and its first derivative guarantee the continuity of the second and the third derivative of the wave function.

Six coefficients c_i satisfy six linear algebraic equations

$$T(g,s,v_0,m,a,e_0)\boldsymbol{X}=0, \tag{17}$$

where $\boldsymbol{X}=\{c_1,c_2,c_3,c_4,c_5,c_6\}$ and matrix T has the form

$$T(g,s,v_0,m,a,e_0)=\begin{pmatrix} w_1(g) & -w_2(g) & -w_3(g) & 0 & 0 & 0 \\ w_1'(g) & -w_2'(g) & -w_3'(g) & 0 & 0 & 0 \\ 0 & -w_2(s) & -w_3(s) & w_4(s) & w_5(s) & 0 \\ 0 & -w_2'(s) & -w_3'(s) & w_4'(s) & w_5'(s) & 0 \\ 0 & 0 & 0 & w_4(1) & w_5(1) & -w_6(1) \\ 0 & 0 & 0 & w_4'(1) & w_5'(1) & -w_6'(1) \end{pmatrix}. \tag{18}$$

Then the dependence of dimensionless energy $e_0(g,s,v_0,m,a)$ on three dimensionless potential parameters g, s, and v_0 is determined by the transcendental equation

$$k(g,s,v_0,m,a,e_0)=\det T(g,s,v_0,m,a,e_0)=0. \tag{19}$$

This equation is solved numerically. Each level of energy is degenerate with two eigenfunctions $\Psi_0^+(x,y)$ and $\Psi_0^-(x,y)$.

When the exact values of $e_0(g,s,v_0,m,a)$ are found it is not hard to obtain the values of coefficients c_i from the system (17) and the standard normalization condition.

So, the exact solution of the unperturbed Schrödinger equation is constructed for an electron in a circular quantum dot which is simulated by the smooth potential (2).

We introduce the dimensionless perturbation $h_1=2M_{eff}\rho_0^2H_1/\hbar^2$ and consider the contribution of h_1 with the help of the perturbation theory in the degenerate case for the small value of γ.

In the basis of the eigenvectors $|\Psi_0^+\rangle$ and $|\Psi_0^-\rangle$ of the unperturbed Hamiltonian we have the following equalities $\langle\Psi_0^\pm|h_1|\Psi_0^\pm\rangle=0$ for the diagonal matrix elements. Off-diagonal matrix elements are given by $\langle\Psi_0^+|h_1|\Psi_0^-\rangle=\langle\Psi_0^-|h_1|\Psi_0^+\rangle=\gamma\delta(m,v,a),$ where

$$\delta=-2ma\int_0^\infty J_1(2ar)w^2(r)dr\Big/\int_0^\infty w^2(r)r\,dr. \tag{20}$$

Then we get splitting $e^\pm=e_0\pm\gamma\delta$ for the energy levels. Normalized eigenfunctions in zero-order approximation, which correspond to the eigenvalues $e^\pm$, are described by the formula $\Psi^\pm=\left(\Psi_0^+\pm\Psi_0^-\right)/\sqrt{2}$. The distinctive feature of the used approximation is zero correction for zero angular momentum ($m=0$).

Now we present some numerical illustrations in addition to the analytical results. If we choose the value of effective electron mass $M_{eff}=0.067M_e$ related to GaAs, where M_e is the electron mass in vacuo, and assume $\rho_0=30$ nm, then the following correspondences $a=1\rightarrow(\alpha_R+\alpha_D)/2=18.9579$ meV nm, $e=1\rightarrow E=0.631933$ meV between the dimensionless and dimensional quantities are obtained.

Tab. 1, 2 demonstrate the dependence of energy levels on potential parameters at the following angular quantum numbers $m=0,\pm1,\pm2$. First of all we emphasize that the number of discrete levels is finite. This number increases if the parameters v_0 and g grow and decreases if m grows. The energy level decreases if the parameter s grows. The ratio δ/e_0 decreases if e_0 grows.

Table 1. The dependence of e_0 and δ on potential parameters for $a = 1$ and $v_0 = 100$

$\lvert m \rvert$	e_0, (δ)			
	$g = 0.1$		$g = 0.9$	
	$s = 0.325$	$s = 0.775$	$s = 0.925$	$s = 0.975$
0	37.8202 (0.00000)	21.1503 (0.00000)	4.36674 (0.00000)	4.20242 (0.00000)
	98.3459 (0.00000)	66.4228 (0.00000)	27.0087 (0.00000)	26.158 (0.00000)
	–	–	66.1516 (0.00000)	64.1934 (0.00000)
1	78.2272 (1.87550)	43.1724 (1.83448)	12.5861 (1.66374)	12.1710 (1.65410)
	–	87.9681 (1.61613)	43.8652 (1.65402)	42.5166 (1.64521)
	–	–	89.2195 (1.54573)	86.8404 (1.55437)
2	–	66.3115 (3.50209)	23.3249 (3.17680)	22.5838 (3.15368)
	–	–	62.8864 (3.22045)	61.0017 (3.20327)

Table 2. The dependence of e_0 and δ on potential parameters for $a = 1$ and $v_0 = 400$

$\lvert m \rvert$	e_0, (δ)			
	$g = 0.1$		$g = 0.9$	
	$s = 0.325$	$s = 0.775$	$s = 0.925$	$s = 0.975$
0	68.4065 (0.00000)	37.9282 (0.00000)	4.97095 (0.00000)	4.78748 (0.00000)
	248.296 (0.00000)	130.485 (0.00000)	30.4112 (0.00000)	29.4418 (0.00000)
	374.034 (0.00000)	223.558 (0.00000)	75.9617 (0.00000)	73.569 (0.00000)
	–	315.804 (0.00000)	141.174 (0.00000)	136.714 (0.00000)
	–	394.955 (0.00000)	225.085 (0.00000)	217.952 (0.00000)
	–	–	325.146 (0.00000)	315.041 (0.00000)
1	154.175 (1.95605)	82.8206 (1.91536)	14.1512 (1.69837)	13.6850 (1.68944)
	324.261 (1.87921)	176.327 (1.83530)	49.6767 (1.70195)	48.1080 (1.69318)
	398.235 (1.16738)	269.601 (1.75627)	105.147 (1.69960)	101.834 (1.69064)
	–	359.397 (1.64424)	179.906 (1.69342)	174.211 (1.68430)
	–	–	272.482 (1.67878)	263.873 (1.67029)
	–	–	377.369 (1.59580)	366.451 (1.61028)
2	244.117 (3.86453)	129.076 (3.74964)	26.2025 (3.26501)	25.3643 (3.24341)
	380.222 (3.53219)	222.626 (3.59204)	71.8550 (3.35158)	69.5931 (3.33240)
	–	315.315 (3.42475)	137.158 (3.36809)	132.829 (3.34919)
	–	396.324 (2.76619)	221.216 (3.36065)	214.206 (3.34202)
	–	–	321.637 (3.31530)	311.605 (3.30183)

Conclusion

The confinement model potential for a quantum dot considered in the present paper is smooth, has finite depth and width and permits the exact solutions of the separated unperturbed Schrödinger equation for electron states in the presence of the spin-orbit interaction of Rashba and Dresselhaus. The contribution of perturbation is really small in comparison with the unperturbed energy e_0 if the strength α_R is sufficiently close to the strength α_D ($\gamma \ll 1$). Further, we intend to construct higher-oder corrections to the energy levels.

References

1. Bychkov Yu.A., Rashba E.I. Oscillatory effects and the magnetic susceptibility of carriers in inversion layers. *J. Phys. C.* 1984;17:6039-6046.
2. Dresselhaus G. Spin-orbit coupling effects in zinc blende structures. *Phys. Rev.* 1955;100:580-586.
3. Li J., Chang K. Direct detection of the relative strength of Rashba and Dresselhaus spin-orbit interaction: Utilizing the SU(2) symmetry. *Phys. Rev. B.* 2010;82.
4. Meier L., Salis G., Shorubalko I., Gini E., Schon S., Ensslin K. Measurement of Rashba and Dresselhaus spin-orbit magnetic fields. *Nature Physics.* 2007; 3:650-654.
5. Schliemann J., Egues J.C., Loss D. Anisotropic transport in a two-dimensional electron gas in the presence of spin-orbit coupling. *Phys. Rev. Lett.* 2003;90.

6. Bernevig B.A., Orenstein J., Zhang S.C. Exact SU(2) symmetry and persistent spin helix in a spin-orbit coupled system. *Phys. Rev. Lett.* 2006;97.
7. Val´ın-Rodr´ıguez M., Puente A., Serra L. Collective oscillations in quantum rings: A broken symmetry case. *Eur. Phys. J. B*. 2004;39:87-92.
8. Kudryashov V.V. Electron in a quantum dot with account of the Rashba spin-orbit interaction. *Proc. of the XIII Intern. School-Conference "Foundations and Advances in Nonlinear Science"*. Minsk, 2006: 125-131.
9. Chaplik A.V., Magarill L.I. Bound states in a two-dimensional short range potential induced by the spin-orbit interaction. *Phys. Rev. Lett.* 2006; 96.
10. Kudryashov V.V., Baran A.V. Influence of Rashba and Dresselhaus Spin-Orbit Interactions of Equal Strengths on Electron States in Circular Quantum Dot. *Nonlinear Dynamics and Applications.* 2021;27:24-30.
11. Abramovitz M. and Stegun I.A. *Handbook of Mathematical Function.* Dover, New York; 1970.

Authors' contribution

Both authors equally contributed to the writing of the article.

Information about the authors

Baran A.V., PhD., Senior Researcher at the B.I. Stepanov Institute of Physics of the National Academy of Sciences of Belarus.

Kudryashov V.V., PhD., Leading Researcher at the B.I. Stepanov Institute of Physics of the National Academy of Sciences of Belarus.

Address for correspondence

220072, Republic of Belarus,
Minsk, Nezavisimosti Ave., 68-2,
B.I. Stepanov Institute of Physics
of the National Academy of Sciences of Belarus;
tel. 8-029-568-98-11;
e-mail: a.baran@dragon.bas-net.by
Baran Aleksandr Valer'evich

http://dx.doi.org/10.35596/1729-7648-2021-19-8-26-30

Original paper

UDC 539.12

GEOMETRIZATION OF THE THEORY OF ELECTROMAGNETIC AND SPINOR FIELDS ON THE BACKGROUND OF THE SCHWARZSCHILD SPACETIME

NINA G. KRYLOVA[1, 2], VICTOR M. RED'KOV[3]

[1]*Belarusian State Agrarian Technical University (Minsk, Republic of Belarus)*

[2]*Belarusian State University (Minsk, Republic of Belarus)*

[3]*B.I. Stepanov Institute of Physics of the National Academy of Science of Belarus (Minsk, Republic of Belarus)*

Submitted 18 November 2021

Abstract. The geometrical Kosambi–Cartan–Chern approach has been applied to study the systems of differential equations which arise in quantum-mechanical problems of a particle on the background of non-Euclidean geometry. We calculate the geometrical invariants for the radial system of differential equations arising for electromagnetic and spinor fields on the background of the Schwarzschild spacetime. Because the second invariant is associated with the Jacobi field for geodesics deviation, we analyze its behavior in the vicinity of physically meaningful singular points $r = M$, ∞. We demonstrate that near the Schwarzschild horizon $r = M$ the Jacobi instability exists and geodesics diverge for both considered problems.

Keywords: electromagnetic field, spinor field, Schwarzschild spacetime, Kosambi–Cartan–Chern invariants, Jacobi stability.

Conflict of interests. The authors declares no conflict of interests.

For citation. Krylova N.G, Red'kov V.M. Geometrization of the theory of electromagnetic and spinor fields on the background of the Schwarzschild spacetime. Doklady BGUIR. 2021; 19(8): 26-30.

Introduction

The behavior of material fields in the vicinity of cosmological objects such as black holes or neutron stars is of great interest [1, 2]. Relevant spacetime models describe gravitational potentials of these objects. However, the search for analytical solutions under the background of curved spacetimes remains to be a complicated problem that stipulates the development of other methods to analyze the behavior of the corresponding dynamical systems.

The Kosambi–Cartan–Chern geometrical approach (KCC-theory) was developed in details in numerous mathematical books and papers [3–5]. KCC-theory allowed to describe the evolution of a dynamical system in a configuration space of the Lagrange type. At that, the dynamical system is governed by the system of second-order differentials equations.

Results and discussion

$$\frac{dy^i}{dr}+2G^i=0,\qquad y^i=\frac{dx^i}{dr},$$
$$G^i=\frac{1}{4}g^{il}\left(\frac{\partial^2 L}{\partial x^k\partial y^l}y^k-\frac{\partial L}{\partial x^l}+\frac{\partial^2 L}{\partial y^l\partial r}\right),\qquad g_{ij}=\frac{1}{2}\frac{\partial^2 L}{\partial y^i\partial y^j}, \tag{1}$$

where L is a Lagrangian function, G^i is called a semispray. The properties of this dynamical system can be described in terms of five KCC geometrical invariants. From the physical point of view, the most interesting invariant is the second one P which is associated with the Jacobi field for geodesics deviation, so it indicates how rapidly different branches of the solution diverge from or converge to the intersection points. Explicitly, the second KCC-invariant can be calculated according to the formula

$$P^i_j=2\frac{\partial G^i}{\partial x^j}+2G^s\frac{\partial N^i_j}{\partial y^s}-\frac{\partial N^i_j}{\partial x^s}y^s-N^i_sN^s_j-\frac{\partial N^i_j}{\partial r},\ N^i_j=\frac{\partial G^i}{\partial y^j}. \tag{2}$$

In this work we apply the KCC-theory to study systems of differential equations which arise in the theory of electromagnetic and spinor fields on the background of the Schwarzschild spacetime.

Electromagnetic field

In [6] the Maxwell equations were considered on the background of the Schwarzschild spacetime

$$dS^2=\Phi dt^2-\frac{dr^2}{\Phi}-r^2\left(d\theta^2+\sin^2\theta d\varphi^2\right), \tag{3}$$

where function $\Phi=1-\frac{M}{r}$, and the differential equation system for the radial components was derived after separating the variables in the initial Maxwell equations both in 3-dimensional Majorana-Oppenheimer and 10-demensional Duffin–Kemmer–Petiau approaches. We start with the second order differential equation for the primary radial function F that was obtained in Majorana–Oppenheimer formalism:

$$\frac{d^2F}{dx^2}+\left(\frac{1}{x-1}-\frac{1}{x}\right)\frac{dF}{dx}+\left(M^2\omega^2+\frac{j(j+1)}{x}+\frac{2M^2\omega^2-j(j+1)}{x-1}+\frac{M^2\omega^2}{(x-1)^2}\right)F=0, \tag{4}$$

where $x=r/M$ is a dimensionless coordinate. The spray coefficient G equals

$$G=\frac{1}{2}\left(\frac{1}{x-1}-\frac{1}{x}\right)\frac{dF}{dx}+\frac{1}{2}\left(M^2\omega^2+\frac{j(j+1)}{x}+\frac{2M^2\omega^2-j(j+1)}{x-1}+\frac{M^2\omega^2}{(x-1)^2}\right)F. \tag{5}$$

The second KCC invariant is found in the form

$$P=\frac{-3+4x\left(1-j(j+1)(x-1)+M^2\omega^2x^3\right)}{4(x-1)^2x^2}. \tag{6}$$

In Duffin–Kemmer formalism the equation for another primary radial function f is ([6]):

$$\frac{d^2f}{dr^2}+\left(\frac{\Phi'}{\Phi}+\frac{2}{r}\right)\frac{df}{dr}+\left(\frac{\omega^2}{\Phi^2}-\frac{2\nu^2}{r^2\Phi}+\frac{\Phi'}{\Phi}\frac{1}{r}\right)f=0, \tag{7}$$

where a derivative over r is denoted by a prime. Utilizing the notations $x=r/M$, one finds the second KCC-invariant in the form:

$$P=\frac{-3+4x\left(1-2\nu^2(x-1)+M^2\omega^2x^3\right)}{4(x-1)^2x^2},\ 2\nu^2=j(j+1), \tag{8}$$

which coincides with (6).

Near singular points, the eigenvalue of the second invariant $\Lambda\equiv P$ behaves as follows:

$$x=\frac{r}{M}\to 0 \quad \Lambda\to-\frac{3}{4x^2}<0; \quad x\to 1\ (r\to M) \quad \Lambda\to\frac{1+4M^2\omega^2}{4(x-1)^2}>0; \quad x\to\infty \quad \Lambda\to\omega^2>0.$$

It indicates that in the vicinity of $x=0$ (this point is nonphysical) the geodesics converge. Vice versa, near the physical points, Schwarzschild horizon $x=1$ and at $x\to\infty$, the Jacobi instability exists and the geodesics diverge. The typical behavior of the eigenvalue as a function of the radial coordinate is shown in Fig. 1, *a*.

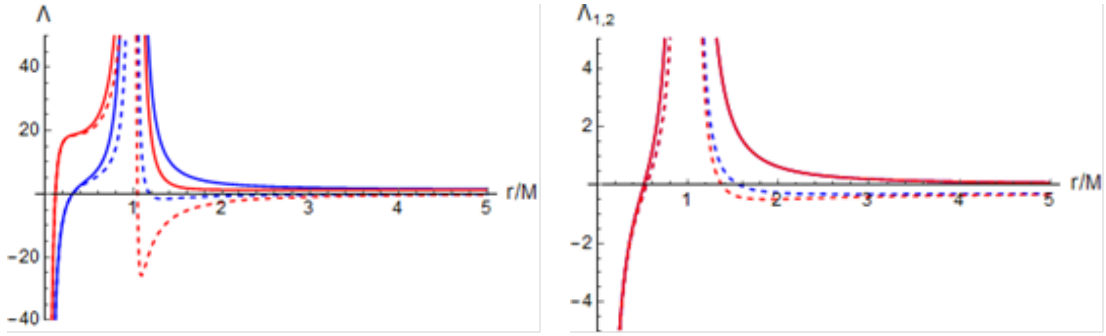

a *b*

Fig. 1. The behavior of the real parts of the second invariant eigenvalues for the geometrized problem of the electromagnetic (*a*) and spinor (*b*) fields on the background of the Schwarzschild spacetime. The values of parameters used are: *a* – $M=1$, $\omega=0.0001$ (dashed curves) and 1.0001 (solid curves), $j=1$ (blue) and 2 (red); *b* – $m=1$, $M=1$, $\varepsilon=0.0001$ (dashed curves) and 1.0001 (solid curves), $j=1/2$; blue and red curves correspond to two different eigenvalues Λ_1 and Λ_2

Spinor field

We consider the spin 1/2 particle on the background of the Schwarzschild spacetime. We start from a generally covariant form of the Dirac equation:

$$\left[i\gamma^a\left(e^\alpha_{(a)}\frac{\partial}{\partial x^\alpha}+\frac{1}{2}\left(\frac{1}{\sqrt{-g}}\frac{\partial}{\partial x^\alpha}\sqrt{-g}e^\alpha_{(a)}\right)\right)-m\right]\Psi(x)=0 \tag{9}$$

in the orthogonal static coordinates $x^\alpha=(t,\theta,\varphi,r)$ and tetrad in the Schwarzschild spacetime

$$e^\beta_{(a)}=g^{\beta\alpha}e_{(a)\alpha}=\begin{vmatrix}\Phi^{-1/2} & 0 & 0 & 0\\ 0 & 1/r & 0 & 0\\ 0 & 0 & 1/r\sin\theta & 0\\ 0 & 0 & 0 & \Phi^{1/2}\end{vmatrix}.$$

After separating the variables with diagonalization of the total angular momentum [7, 8] we derive the system of equations

$$\begin{aligned}
&\frac{\varepsilon}{\sqrt{1-\frac{M}{r}}}f_3-i\sqrt{1-\frac{M}{r}}\frac{df_3}{dr}-i\frac{\nu}{r}f_4-Mf_1=0, \quad \frac{\varepsilon}{\sqrt{1-\frac{M}{r}}}f_4+i\sqrt{1-\frac{M}{r}}\frac{df_4}{dr}+i\frac{\nu}{r}f_3-Mf_2=0,\\
&\frac{\varepsilon}{\sqrt{1-\frac{M}{r}}}f_1+i\sqrt{1-\frac{M}{r}}\frac{df_1}{dr}-i\frac{\nu}{r}f_2-Mf_3=0, \quad \frac{\varepsilon}{\sqrt{1-\frac{M}{r}}}f_2-i\sqrt{1-\frac{M}{r}}\frac{df_2}{dr}-i\frac{\nu}{r}f_1-Mf_4=0.
\end{aligned} \tag{10}$$

Each complex function $f_i(r)$ we resolved into a sum of real and imaginary parts:

$$f_1 = x_1 + ix_2\,,\ f_2 = x_3 + ix_4\,,\ f_3 = x_5 + ix_6\,,\ f_4 = x_7 + ix_8\,. \tag{11}$$

By substituting expressions (11) into the system (10) one gets the system of 8 connected differential equation systems of the first order. To bring it to the second order differential system of the type (1) we differentiate each equation over the radial variable. After that the second invariant P_j^i can be directly calculated

$$P_j^i = \begin{pmatrix} \alpha & -\beta & \gamma & 0 & 0 & 0 & 0 & 0 \\ \beta & \alpha & 0 & \gamma & 0 & 0 & 0 & 0 \\ \gamma & 0 & \alpha & \beta & 0 & 0 & 0 & 0 \\ 0 & \gamma & -\beta & \alpha & 0 & 0 & 0 & 0 \\ 0 & 0 & 0 & 0 & \alpha & \beta & \gamma & 0 \\ 0 & 0 & 0 & 0 & -\beta & \alpha & 0 & \gamma \\ 0 & 0 & 0 & 0 & \gamma & 0 & \alpha & -\beta \\ 0 & 0 & 0 & 0 & 0 & \gamma & \beta & \alpha \end{pmatrix}, \tag{12}$$

where

$$\alpha = \frac{4r^4(\varepsilon^2 - m^2) + 4Mr\left(m^2r^2 + \nu^2 + 2\right) - 5M^2 - 4\nu^2r^2}{16r^2(M-r)^2}\,,\ \beta = \frac{\varepsilon M}{4(M-r)^2}\,,\ \gamma = -\frac{\nu}{2r^2\sqrt{1-\dfrac{M}{r}}}\,.$$

The eigenvalues Λ_i of the second invariant P_j^i is fourfold degenerated, the different two are determined as

$$\Lambda_{1,2} = \alpha \pm \sqrt{\gamma^2 - \beta^2} = \frac{1}{16}\left(\frac{4m^2r^2 + 4\nu^2 - 2}{r(M-r)} \pm 4\sqrt{-\frac{M^2\varepsilon^2}{(M-r)^4} - \frac{4\nu^2}{r^3(M-r)} + \frac{4r^2\varepsilon^2 + 3}{(M-r)^2} - \frac{5}{r^2}} \right).$$

The dependences of two different eigenvalues $\Lambda_{1,2}$ of the second invariant on the radial variable have been analyzed for different values of energy ε (see Fig. 1, *b*). Near the singular points the eigenvalues behave as follows:

$$r \to 0 \qquad \Lambda_{1,2} \to -\frac{5}{16r^2} < 0\,,$$

$$r \to M \qquad \Lambda_{1,2} \to \frac{r^2\varepsilon^2 + 3}{4(M-r)^2} \pm \frac{iM\varepsilon}{4(M-r)^2},\ \ \mathrm{Re}(\Lambda_{1,2}) \to \frac{r^2\varepsilon^2 + 3}{4(M-r)^2} > 0\,,$$

$$r \to \infty \qquad \Lambda_{1,2} \to \frac{1}{4}\left(\varepsilon^2 - m^2\right).$$

So, in the vicinity of the Schwarzschild horizon the geodesics diverge at any energy ε, while at $r \to \infty$ the geodesics diverge at $\varepsilon > m$ and converge at $\varepsilon < m$, however the second possibility may be ignored as nonphysical.

The contradictory results have been found out for the problem of the existence of bound states for the Dirac equation in the presence of a black hole [2, 9]. Our results on the KCC-analysis support the conclusion that the fermion bound state on the background of a Schwarzschild black hole are absent as the bound state solution has to be characterized by the convergence of the geodesics flow near the extreme points $r \to M$ and $r \to \infty$. The main argument against the existence of bound states in this system consists of the following: effective potential curves are of a barrier type and do not contain any potential well (see [7]).

Conclusions

The authors applied the KCC-geometrical approach to study the radial systems arising in two problems, electromagnetic and spinor fields on the background of the Schwarzschild spacetime. The stability analysis in terms of the second invariant demonstrates similar behavior of geodesics at $r \to \infty$ for these two systems.

References

1. Moalem A., Gersten A. Quantum theory of massless particles in stationary axially symmetric spacetimes. *Entropy.* 2021;23:1205. https://doi.org/10.3390/e23091205.
2. Batic D., Nowakowski M., Morgan K. The problem of embedded eigenvalues for the Dirac equation in the Schwarzschild black hole metric. *Universe.* 2016;2:31. DOI:10.3390/universe2040031.
3. Atanasiu Gh., Balan V., Brinzei N., Rahula M. *Differential geometry of the second order and applications: Miron-Atanasiu theory*. Moscow: URSS; 2010.
4. Antonelli P.L., Bevilacqua L., Rutz S.F. Theories and models in symbiogenesis. *Nonlinear Analysis.* 2003;4:743-753.
5. Antonelli P.L., Bucataru I. New results about the geometric invariants in KCC-theory. *An. Şt. Univ. "Al.I.Cuza" Iaşi. Mat. N.S.* 2001;47:405-420.
6. Ovsiyuk E.M., Red'kov V.M. *Maxwell electrodynamics in the spaces with non-Euclidean geometry*. Mozyr: MSPU named after I.P.Shamyakin; 2011.
7. Ovsiyuk E.M., Veko O.V., Rusak Yu.A., Chichurin A.V., Red'kov V.M. To analysis of the Dirac and Majorana particle solutions in Schwarzschild field. *NPCS*. 201720(1):56-72.
8. Chichurin A., Ovsiyuk E., Red'kov V. On tunneling spin 1/2 particles through Schwarzschild barrier. *Computer Algebra Systems in Teaching and Research*. 2019;8:19-37.
9. Zecca A. Spin 1/2 bound states in Schwarzschild geometry. *Adv. Studies Theor. Phys.* 2007;1:271-279.

Authors' contribution

Krylova N.G. performed the study, prepared the manuscript of the article.
Red'kov V.M. stated a research problem, performed the study.

Information about the authors

Krylova N.G., PhD., Associate Professor, Associate Professor at Belarusian State Agrarian Technical University, Senior Researcher at Belarusian State University.

Red'kov V.M., D.Sc., Principal Researcher at B.I. Stepanov Institute of Physics of the National Academy of Science of Belarus.

Address for correspondence

220030, Republic of Belarus,
Minsk, Nezavisimosti Ave., 4,
Belarusian State University;
tel. +375-29-559-71-05;

Krylova Nina Georgievna

http://dx.doi.org/10.35596/1729-7648-2021-19-8-31-34

Original paper

UDC 53.087.4

INFORMATION - STATISTICAL APPROACH TO INVERSE OPTICAL PROBLEM SOLUTION FOR 3D DISPERSE SYSTEMS WITH NANO- AND MICRO PARTICLES

ALEXANDRA G. BEZRUKOVA, OLGA L. VLASOVA

Peter the Great St. Petersburg Polytechnical University (St. Petersburg, Russian Federation)

Submitted 18 November 2021

Abstract. Multiparameter analysis of simultaneous optical data for *3D* disperse systems (consisted from nano- and/or microparticles of different nature) by information-statistical methods can help to estimate the share of different types of particles in mixtures. At the solution of inverse optical problem for unknown poly-component *3D* DS, the comparison of measured parameters with the known ones from the set of mono-component *3D* DS can help to identify the component content of the system under study. The approach was tested on the biomineral water mixtures of kaolin clay and bacterium coli bacillus with the help of the program based on the information-statistical theory. To solve the impurity optical recognition tasks, the Base of optical data for *3D* DS is needed.

Keywords: biomineral mixtures, *3D* disperse systems, information-statistical methods, micro and nanoparticles, online optical control.

Conflict of interests. The authors declare no conflict of interests.

Gratitude. The authors thank Dr. Dmitriy F. Kalinin for the opportunity to process experimental data using the program MultAlt.

For citation. Bezrukova A.G., Vlasova O.L. Information-statistical approach to inverse optical problem solution for *3D* disperse systems with nano- and micro particles. Doklady BGUIR. 2021; 19(8): 31-34.

Introduction

Ensembles of nano- and / or micro- particles can be considered as three-dimensional (*3D*) disperse systems (DS) with particles as a disperse phase in dispersive medium (water, air, etc.) [1]. The particle sizes of the *3D* DS studied at our work [2–7] vary from nanometers to approximately ten micrometers in an average diameter. This article is devoted to the application of information-statistical methods [8–11] to multiparameter optical analysis of bicomponents (BC) *3D* DS such as biomineral mixtures of kaolin clay (polymodal *3D* DS consisted from nano and micro particles) and bacterium coli bacillus (with the average diameter about one micrometer) [5]. The inverse optical problem solution for polycomponent (PC) *3D* DS meets with difficulties due to the necessity of "a priori" information about component *3D* DS content. The set of parameters from optical methods: refractometry, absorbance, fluorescence, and light scattering (integral and differential, static and dynamic, unpolarized and polarized) is unique for each mono-component (MC) *3D* DS [6].

At the analysis of unknown PC *3D* DS, the comparison of measured parameters with the known ones for the set of MC *3D* DS can help to identify the system under study. For this purpose, the computer technology "MultAlt" [10] for practical prognosis based on the information-statistical

theory [8–11] was used. This approach provides the process of interpretation and visualization of intermediate and final results with an estimation of decision probability.

Methods of conducting experiment

The information-statistical methodology was tested on experimental biomineral mixtures as a two component (BC) *3D* DS consisted of kaolin clay [5] and bacterium coli bacillus (or Escherichia coli, or E. coli) of strain K-802 [5] in different proportions. Particle size distributions for both *3D* DS are polymodal with nano and micro particles [5].

In the previous articles [2–7] there were discussions about the main compatible optical methods for *3D* DS online characterization [7], polarization measurements information possibilities, and the *3D* DS polymodality [4]. *ND* unique optical vector of *3D* DS [6, 7] is the *ND* set of the so called "second-class" optical parameters by which the MC *3D* DS can be characterized and compared with other MC *3D* DS. One of the main second-class parameters is "wave exponent" – $n(\lambda)$ [1], which can be obtained by measuring on spectrophotometer the extinction of light due to the integral light scattering. At the interval of wavelength (λ), where there is no absorbance of light by *3D* DS, optical density spectra – $D(\lambda)$, can be considered as a measure of the integral light scattering (except the aperture angle of a photo-receiver). On a bi-logarithmic scale the slope of the linear part of $D(\lambda)$ is $n(\lambda)$ (Fig. 1):

$$n(\lambda) = -\Delta \lg D(\lambda) / \Delta \lg \lambda . \quad (1)$$

For the identification of potential objects in unknown *3D* DS mixtures the information-statistical methodology of complex interpretation of experimental data [8–11] with the computer technology MultAlt [10] are considered.

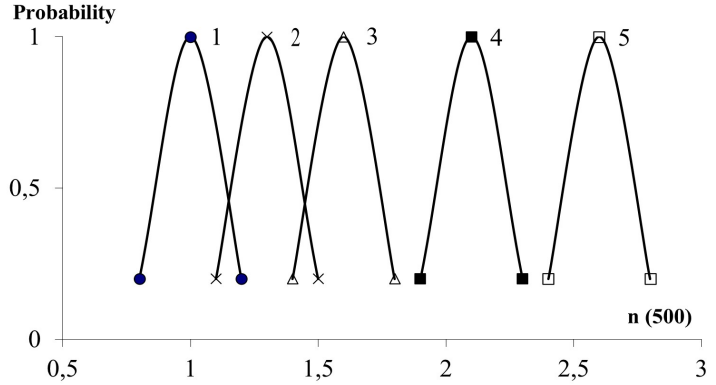

Fig. 1. The scheme of probability distributions for five experimental *3D* DS with the following $n(\lambda)$ values at λ = 500 nm: 1) 1.00 by volume – only kaolin clay (MC *3D* DS), $n(500)$ = 1.0; 2) mixture of 0.75 by volume – kaolin clay and 0.25 – coli bacillus (BC *3D* DS), $n(500)$ = 1.3; 3) mixture of 0.5 by volume – kaolin clay and 0.5 – coli bacillus (BC *3D* DS), $n(500)$ = 1.6; 4) mixture of 0.25 by volume kaolin clay and 0.75 – coli bacillus (BC *3D* DS), $n(500)$ = 2.1; 5) 1.0 by volume – only coli bacillus (MC *3D* DS), $n(500)$ = 2,6. Errors of n (500) about 3–5 %

Earlier [6, 7] it was reported that a set of optical parameters of the so-called second class (obtained as a result of processing experimental data without involving any a priori information about *3D* DS) is unique for each *3D* DS and implicitly reflects characteristics of *3D* DS: shape, refractive index of particles, distribution functions of number and mass of particles in size, etc. In other words, the characteristic of any *3D* DS can be represented as an *ND* vector in the *N*-dimensional space of optical parameters of the second class. On the basis of theory and experiment it is possible to predict specific parameters for a certain component. In the previous papers, the *3D* DS polymodality problem [4], optical characterization of *3D* DS mixtures [5], and the use of unique optical vectors for monitoring the aggregation process [7] were discussed. This part of study is connected with creation of algorithm based on the information-statistical methodology [8–11], which can help in the search of the most informative data for the particles of interest control (Fig. 1, 2).

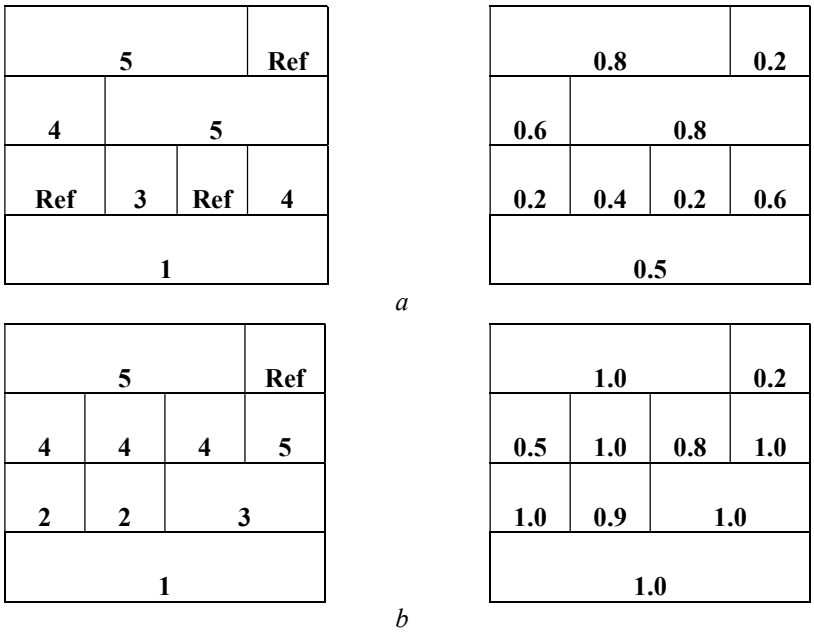

Fig. 2. MultAlt solutions (left) and probabilities of MultAlt solutions (right) based on the data from unique vectors for dispersions of kaolin clay (1), coli bacillus (5), and their mixtures (2, 3, 4) are submitted in Fig. 1. The data based on one (*a*) and five (*b*) optical parameters of the second class. Note: mixture 2 (*a*) did not appear at the analysis by this parameter of the second class**.** "Ref" means that the program MultAlt refused from solution with probability 0.2

Experimental results and discussion

The mixed dispersion of kaolin clay and bacterium coli bacillus can be designated as BC *3D* DS and considered as a model of natural water. With the help of a number of optical methods it is possible to obtain information on the distribution of particles in a multimodal *3D* DS [4]. However, the question of the component affiliation of different modes in mixtures remains open. In the study of unknown *3D* DS mixtures, there is a priori an uncertainty of knowledge about the type of the constituent particles, which requires the development of approaches to the interpretation of data. It seems that one of the promising areas in the study of various optical parameters, on the informative possibility to determine the component composition of unknown *3D* DS mixtures, is the method based on the information–statistical theory of optimal complexation [8–11].

The peculiarity of the input data is that instead of the component physical parameter, the probability of a component with this parameter presence is input (Fig. 1). The algorithms and programs developed on the base of optimal complexation can allow the analysis of PC *3D* DS by *ND* vector optical parameters to identify the components the presence of which is the most probable. For example, the solution of five-alternative optical recognition task for mixtures of kaolin clay and bacterium coli bacillus by MultAlt program [10] is presented (Fig. 2).

Conclusion

In the unique vector approach after the detailed *3D* DS study there is a proposal of the optical parameter set which can be a useful tool for online analyzing complex *3D* DS. The *ND* vector can characterize as unity the *3D* DS state with a minimum interference. For differentiation of *3D* DS constituents in mixtures the dimensions of *ND* vectors can be enlarged due to the involvement into consideration of different measurement conditions such as wavelengths, angles and apertures of measurements, polarization, etc. Calculations are based only on the experimental data (without any models of particle structures and size distributions) and can be performed online. For better differentiation of the components in mixtures (for the solution of the impurity of optical recognition tasks for *3D* DS) the Base of optical data is needed [2, 3].

Acknowledgements. *Authors thank Prof. Vitaly J. Klenin, Prof. Sergei Ya. Frenkel, Prof. Feodor M. Goltsman, Prof. Alexander I. Melker, Dr. Tatyana B. Kalinina, Dr. Margarethe Hofmann, Dr Dmitriy F. Kalinin for the useful discussions. No external funding was received for this study.*

References

1. Klenin V.J. *Thermodynamics of systems containing flexible chain polymers*. Elsevier; 1999.
2. Bezrukova A.G. Development of multiparametric optical assay for on-line environmental control. *Proceedings of SPIE*. 1997;3107:298-304.
3. Bezrukova A.G. Nondestructive testing of *3D* disperse systems with micro and nano particles: *N*-dimensional space of optical parameters. *Proceedings of SPIE*. 2006;6253:62530C1-C4.
4. Bezrukova A.G., Vlasova O.L. Optical characterization of *3D* disperse systems with nano and micro particles: polymodality of size distributions. *Materials Physics and Mechanics*. 2012;13(2):162-174.
5. Bezrukova A.G., Vlasova O.L. Mixtures of *3D* disperse systems with nano and micro particles: Optical Characterization. *St. Petersburg Polytechnic University Journal, Physics and Mathematics*. 2016;2(4):316-321. http://dx.doi.org/10.1016/j.spjpm.2016.11.004.
6. Bezrukova A.G., Vlasova O.L. Optical characterization of *3D* disperse systems with nano and micro particles: Unique vectors. *Materials Physics and Mechanics*. 2018;39(1):81-86. DOI: 10.18720/MPM.3912018_13.
7. Bezrukova A.G., Vlasova O.L. Nano and micro particle aggregation: unique optical vectors for control. *Materials Physics and Mechanics*. 2020;45(1):87-95. DOI: 10.18720/MPM.4512020_9.
8. Goltsman F.M. *Physical experiment and statistical conclusions*. Leningrad: Leningrad University Publishing House; 1982.
9. Kalinina T. B., Goltsman F.M. Methodological problems of interpretation of gravitational and magnetic Fields. *Russian Geophysical Journal*. 1994;(2):63-68.
10. Goltsman F.M., Kalinin D.F., Kalinina T.B. MULTALT computer technology for multi-alternative classification and forecasting for a complex of geodata. *Russian Geophysical Journal*. 2000;(17-18):64-70.
11. Kalinin D.F. *Information and statistical prediction of mineral resources*. St. Petersburg: Geological Exploration Group Publishing House; 2011.

Authors' contribution

Bezrukova A.G. and Vlasova O.L. – both authors performed the task for the study.
Bezrukova A.G. prepared the manuscript of the article.

Information about the authors

Bezrukova A.G., D.Sc., Senior Researcher, Corresponding member of St. Petersburg Academy of Sciences on Strength Problems, Peter the Great St. Petersburg Polytechnical University.

Vlasova O.L., D.Sc., Assistant Professor, Director of Graduate School of Biomedical Systems and Technologies in the Institute of Biomedical Systems and Biotechnology of Peter the Great St. Petersburg Polytechnical University.

Address for correspondence

195251, Russian Federation,
St. Petersburg, Polytekhnicheskaya St., 29.
Peter the Great St. Petersburg Polytechnical University;
e-mail: bezr@pb1097.spb.edu
Bezrukova Alexandra Gennadievna

http://dx.doi.org/10.35596/1729-7648-2021-19-8-35-39

Original paper

UDC 541.1

MODIFICATION OF THE RLA MODEL FOR PRESENTING A CLUSTER SYSTEM OF A COMPOSITE MATERIAL WITH A FRACTAL FILLER STRUCTURE

ALIAKSANDR V. BELKO, NIKOLAI N. BABARIKA, IOSIF S. ZEYLIKOVICH, ALIAKSANDR V. NIKITIN

Yanka Kupala State University of Grodno (Grodno, Republic of Belarus)

Submitted 19 November 2021

Abstract. The paper proposes a modification of the diffusion-limited aggregation model to study the properties of a cluster system. A computational experiment to determine the mutual influence of the sticking probability and the volume concentration of particles on the formation of fractal clusters in a cluster system was carried out in accordance with the second-order orthogonal central compositional plan (OCCP). As a result of a computational experiment in accordance with the OCCP, an equation was obtained for the dependence of the mass fractal dimension of clusters on the volume of particle concentration and the probability of adhesion of diffusing particles and cluster particles in the adhesion zone. This dependence was obtained in a range of volume concentration of particles from 2 to 5 % and the probability of adhesion of diffusing particles and particles of clusters in the adhesion zone from 0.2 to 1.

Keywords: polymer composites, cluster system, fractal dimension, RLA models.

Conflict of interests. The authors declare no conflict of interests.

For citation. Belko A.V, Babarika N.N., Zeylikovich I.S., Nikitin A.V. Modification of the RLA model for presenting a cluster system of a composite material with a fractal filler structure. Doklady BGUIR. 2021; 19(8): 35-39.

Introduction

Simulation methods can be used quite effectively along with experimental methods for studying the structure and properties of objects. The known methods (the diffusion-limited aggregation model and its modification) make it possible to fully describe the structure of single fractal clusters. At the same time, it is important to study the influence of a cluster system on the physical properties of the entire compositional system. Therefore, it becomes necessary to develop aggregation models for describing a system of fractal clusters (cluster system) in a range of dimensions observed in physical objects.

In [1–7], the quantitative characteristics of the spatial distribution of filler-copper particles in the matrix of a composite material based on polytetrafluoroethylene were investigated and determined using images of the surface obtained by optical microscopy methods. To determine the quantitative parameters of the structure of clusters, the method of cluster recognition based on threshold segmentation (Otzu method) was applied. The analysis of the distribution structure of copper particles in a polymer matrix at filler concentrations in the range of 1–20 wt. % shows that

the structure of the filler forms clusters can be described within the reaction-limited aggregation (RLA) model. It was found out that the fractal dimensions of the profile of the selected segments of copper clusters in the polytetrafluoroethylene matrix are in the range from 1.65 to 1.72 with a change in the mass concentration of copper from 1 to 20 %. The fractal dimensions of the profile of clusters, the structure of which was calculated within the framework of the RLA model (for three-dimensional lattices), vary from 1.62 to 1.72 when the probability of adhesion of a diffusing particle and cluster particles in the adhesion zone changes from 0.2 to 1.

The fractal dimensions of the profile of the clusters, the structure of which was calculated within the framework of the RLA model (for three-dimensional lattices), vary from 1.62 to 1.72 when the probability of adhesion of a diffusing particle and cluster particles in the adhesion zone changes from 0.2 to 1. This parameter of the RLA model, as adhesion probability, can serve as a link between the fractal dimension of the cluster profile and its mass fractal dimension.

In accordance with the RLA model, one seed particle of the cluster is placed in the space under consideration, and then one new particle is added to the space. Each new particle moves according to the law of random walks. If a particle reaches the boundary of space, it is reflected from it. The particle continues to move until it is in the vicinity of one of the cluster particles. Further, the diffusing particle is attached to the cluster in accordance with the given probability of adhesion of the diffusing particle and the configuration of the cluster particles in the adhesion zone. If a diffusing particle joins a cluster, then the next particle is launched into space. If the attachment of the particle to the cluster did not occur, then the particle continues to move according to the law of random walks. Thus, a cluster is formed [8–10].

Methods of conducting experiment

One of the options for modifying the RLA model is the condition for the termination of cluster growth. Usually, in the RLA model, the condition for the termination of cluster growth is that the cluster reaching the boundaries of the region. However, this condition can be changed by setting a finite amount (volume concentration) of primary particles from which a cluster is formed. The calculations provided that the cluster reaches the boundaries of the region, show that the volume concentration of particles corresponds to 2 %. The volume concentration of primary particles is related to the mass concentration of copper in the matrix of the composite material based on polytetrafluoroethylene and can be another parameter for comparing real clusters and model objects.

Real physical systems usually consist of several clusters (cluster system). In order to obtain a model of such a system, the RLA method can also be modified. In our case, unlike the RLA model, during the clustering process, seed particles are randomly added so that they do not move over the region and from which clusters can be formed. Also, during the clustering process, in accordance with the RLA model, particles are sequentially launched that diffuse over the area. If a diffusing particle enters a cell next to a cluster, then, depending on the adhesion probability, it either joins the cluster or continues to diffuse over the region. Thus, it is possible to build a cluster system. In this work, the RLA model was modified to study the properties of the cluster system in the range of the volume concentration of particles from 2 to 5 % and the probability of adhesion of diffusing particles and cluster particles in the adhesion zone from 0.2 to 1.

In this case, an informative characteristic of fractal clusters of the system can be their average fractal dimension. The calculations have shown that the average fractal dimension of clusters in the system corresponds to the fractal dimension of clusters, the structure of which was calculated within the RLA model with the corresponding probability of diffusing particles and cluster particles adhesion in the adhesion zone. An example of fractal clusters of the system is shown in Fig. 1.

a *b*

Fig. 1. Cluster systems obtained within the framework of the RLA model on three-dimensional lattices at various sticking probabilities: *a* – 1.0; *b* – 0.2

Experimental results

Within the framework of the modified RLA model, a computational experiment to determine the effect of the volume concentration of primary particles and the probability of diffusing particles and cluster particles adhesion in the adhesion zone to their fractal structure in the cluster system was carried out in accordance with the second-order orthogonal central compositional plan (OCCP). OCCP refers to an "active" experiment in which the input actions are purposefully changed [11–12]. OCCP allows you to obtain a statistical model (empirical) of the research object. The object of the study is the response function, which connects the output parameter D (in our case, the mass fractal dimension) with the factors x_1 (volume concentration of primary particles) and x_2 (the probability of adhesion of diffusing particles and cluster particles in the adhesion zone). Numerical calculations for the three-dimensional case were performed at volume concentrations of primary particles from 2 to 5 % and the probability of adhesion of diffusing particles and particles of clusters in the adhesion zone in the range from 0.2 to 1. The OCCP allows obtaining a regression equation in the form of a full quadratic polynomial:

$$D = b_0 + b_1 x_1 + b_2 x_2 + b_{12} x_1 x_2 + b_{11}(x_1^2 - a) + b_{22}(x_2^2 - a), \quad (1)$$

where x_1 and x_2 – are coded values of factors, a is a parameter that depends on a number of factors.

The maximum value of the volumetric concentration of primary particles is set at 5 % in the computational experiment corresponds to the coded value of factor 1, the minimum value of 2 % corresponds to the coded value of –1. Likewise, for the sticking probability, a maximum value of 1 corresponds to a coded value of 1, and a minimum 0.2 corresponds to –1. The values of the output parameter D (the results of repeating experiments D_1, D_2, D_3, D_4) corresponding to the coded values of the factors are presented in Tab. 1.

Table 1. OCCP experiment planning matrix

U	b_0	b_1	b_2	b_{12}	b_{11}–a	b_{22}–a	D_1	D_2	D_3	D_4
1	1	–1	–1	1	0,333	0,333	2,5	2,5	2,5	2,49
2	1	1	–1	–1	0,333	0,333	2,57	2,57	2,56	2,57
3	1	–1	1	–1	0,333	0,333	2,37	2,36	2,36	2,37
4	1	1	1	1	0,333	0,333	2,44	2,45	2,45	2,45
5	1	–1	0	0	0,333	–0,667	2,4	2,41	2,4	2,41
6	1	1	0	0	0,333	–0,667	2,48	2,47	2,48	2,47
7	1	0	–1	0	–0,667	0,333	2,54	2,53	2,54	2,53
8	1	0	1	0	–0,667	0,333	2,41	2,4	2,41	2,41
9	1	0	0	0	–0,667	–0,667	2,44	2,45	2,44	2,45

After carrying out a computational experiment in accordance with the OCCP technique, the hypothesis of the reproducibility of the experimental results was tested using the Cochran criterion [11, 12]. The calculated value of the Cochran test that equals to 0.125 turned out to be less than its critical tabular value equal to 0.403 for a 5 % significance level. In this case, you can start calculating the coefficients of the polynomial.

The calculation of the coefficients of the polynomial b_0, b_1, b_2, b_{12}, b_{11}, b_{22} in the regression equation (1) and their corresponding Student t-tests (respectively equal to 3132; 38.5; 65.8; 2.65; 1.75; 17) and subsequent comparison with the critical value of the Student's t-test equal to 2.05 for a 5% significance level showed that the coefficients of the polynomial b_0, b_1, b_2, b_{12}, b_{22} are significant. The b_{11} coefficient is insignificant. In this case, the mathematical dependence of the fractal dimension on the coded values of the factors (concentration of electrolyte counterions, potential) can be represented as:

$$D = 2.442 + 0.037x_1 - 0.063x_2 + 0.003x_1x_2 + 0.028x_2^2. \quad (2)$$

At the next stage, the hypothesis about the adequacy of the constructed model was tested on the basis of the Fisher criterion [11, 12]. The value of the Fisher criterion was obtained – 1.62, which is less than the critical value (2.73 for a 5 % significance level). Based on the calculation, a conclusion was made about the adequacy of the regression model to the data obtained as a result of the computational experiment.

When passing from the coded values of the factors x_1, x_2 in the equation (2), respectively, to the factors expressed on a natural scale (volume concentration of primary particles, the probability of adhesion of diffusing particles and cluster particles in the adhesion zone), an equation was obtained for the dependence of the mass fractal dimension of clusters (D) on the volume concentration of primary particles (n), the probability of adhesion of diffusing particles and cluster particles in the adhesion zone (P) [12]:

$$D = 2.524 + 2{,}167n - 0.385P + 0.5nP + 0.175P^2. \quad (3)$$

The developed methods for modeling a cluster system can be used to model the structure of a filler in composite materials and predict physical properties of composite systems.

Conclusion

The paper proposes a modification of the RLA model to study the properties of a cluster system. A computational experiment to determine the mutual influence of the adhesion probability and the volume concentration of particles on the formation of fractal clusters in a cluster system was carried out in accordance with the second-order orthogonal central compositional plan. As a result of the computational experiment in accordance with the OCCP, an equation was obtained for the dependence of the mass fractal dimension of clusters on the volume concentration from 2% to 5 % and the adhesion probability of diffusing particles and cluster particles in the adhesion zone from 0.2 to 1. The developed methods for modeling a cluster system can be used to present the structure of the filler in composite materials and predict the physical properties (thermal conductivity) of composite systems.

References

1. Belko A.V., Nikitin A.V. Fractal structure copper clusters in a matrix of polytetrafluoroethylene. *NDTCS-2017. 17th International Workshop on New Approaches to High-Tech: Nano-Design, Technology. Computer Simulations October 26–27*. Minsk, Belarus; 2017: 140-141.
2. Belko A.V., Babarika N.N., Zeyikovich I.S., Nikitin A.V. Diagnostics of the structure of fractal copper clusters in a polytetrafluoroethylene matrix. *Pattern Recognition and Image Analysis.* 2020;9(1):1-6.
3. Belko A.V., Babarika N.N., Zeyikovich I.S., Nikitin A.V. Diagnostics of the structure of fractal copper clusters in a matrix of polytetrafluoroethylene. *Proc. 14th International Conference on Pattern Recognition and Information Processing (PRIP'2019)*. Minsk, Belarus, May 21–23; 2019: 316-319.

4. Belko A.V., Nikitin A.V. Fractal structure copper clusters in a matrix of polytetrafluoroethylene. *Vesn. Grod. Dzyarzh. Univ.*, Ser. 2. 2017;7(3):90-97.
5. Belko A.V., Nikitin A.V. Simulation of cluster formation in a liquid dispersion medium. *Vesn. Grod. Dzyarzh. Univ.*, Ser. 2. 2015;192(2):92-100.
6. Belko A.V., Mogil'nikov I.V. Models of fractal structures of fillers in composite systems. *Transport. "Nauka – budushchee Litvy*": *doklady 10 konferentsii molodykh uchenykh Litvy*, Vil'nius, 23 maia 2007 g. Vil'nius: Vil'niusskii tekhn. universitet im. Gediminasa; 2007:206-211.
7. Belko A.V., Nikitin A.V. The kinetics of formation of fractal clusters in disperse systems with irreversible coagulation. *Vesn. Grod. Dzyarzh. Univ.,* Ser. 2. 2006;41(2):56-61.
8. Smirnov B.M. Fractal clusters. *UFN*. 1986;9(6):481-505.
9. Belko A.V., Nikitin A.V. Methods for constructing objects with fractal structure. *Vesn. Grod. Dzyarzh.Univ.*, Ser. 2. 2002;11(2):133-137.
10. Belko A.V., Nikitin A.V., Skaskevich A. A., Bachurina A. Yu., Sarosek S. I. Models of fractal structures in composite systems on the basis of polymers. *Vesn. Grod. Dzyarzh. Univ*., Ser. 2. 2012;129(2):95-104.
11. Belko A.V., Babarika N. N., Nikitin A. V. Effect of double electric layers of disperse particles on structure and mechanisms of formation of fractal clusters in disperse systems. *Vesn. Grod. Dzyarzh. Univ.,* Ser. 2. 2019;9(1):68-77.
12. Belko A.V., Babarika N. N., Zeyikovich I. S., Nikitin A. V. Modification of the RLA model for presenting a cluster system of a composite material with a fractal filler structure. *Book of abstracts NDTCS-2021. 19th International Workshop on New Approaches to High-Tech: Nano-Design, Technology, Computer Simulations.* Minsk, Belarus, October 28–29; 2021: 95-97.

Authors' contribution

Belko A.V., Babarika N.N., Zeyikovich I.S. and Nikitin A.V. performed the task for the study, obtained the results, and prepared the article in equal parts.

Information about the authors

Belko A.V. PhD., Chair, Associate Professor at the Department of Information Systems and Technologies of Yanka Kupala State University of Grodno.

Babarika N.N. Senior Lecturer at the Department of Fundamental and Applied Mathematics of Yanka Kupala State University of Grodno.

Zeylikovich I.S. D.Sc., Professor, Professor at the Department of Electrical Engineering and Electronics of Yanka Kupala State University of Grodno.

Nikitin A.V. PhD., Chair, Associate Professor at the Department of Theoretical Physics and Heat Engineering of Yanka Kupala State University of Grodno.

Address for correspondence

230023, Republic of Belarus,
Grodno, Ozheshko St., 22,
Yanka Kupala State University of Grodno;
tel. +375-29-780-49-98;
e-mail: belko_av@grsu.by
Belko Aliaksandr Vitalievich

http://dx.doi.org/10.35596/1729-7648-2021-19-8-40-44

Original paper

UDC 004.855.5:004.932.75

DEVELOPING A SEQ2SEQ NEURAL NETWORK USING VISUAL ATTENTION TO TRANSFORM MATHEMATICAL EXPRESSIONS FROM IMAGES TO LATEX

PAVEL A.VYAZNIKOV, IGOR D. KOTILEVETS

MIREA – Russian Technological University (Moscow, Russian Federation)

Submitted 19 November 2021

Abstract. The paper presents the methods of development and the results of research on the effectiveness of the seq2seq neural network architecture using Visual Attention mechanism to solve the im2latex problem. The essence of the task is to create a neural network capable of converting an image with mathematical expressions into a similar expression in the LaTeX markup language. This problem belongs to the Image Captioning type: the neural network scans the image and, based on the extracted features, generates a description in natural language. The proposed solution uses the seq2seq architecture, which contains the Encoder and Decoder mechanisms, as well as Bahdanau Attention. A series of experiments was conducted on training and measuring the effectiveness of several neural network models.

Keywords: im2latex, seq2seq, NLP, neural network.

Conflict of interests. The authors declares no conflict of interests.

For citation. Vyaznikov P.A., Kotilevets I.D. Developing a seq2seq neural network using visual attention to transform mathematical expressions from images to LaTeX. Doklady BGUIR. 2021; 19(8): 40-44.

Introduction

In the modern world, Optical Character Recognition technology finds an incredible number of applications (text recognition and rapid document scanning). The progress in this area is due to the emergence of advanced deep learning algorithms and neural network models which learn from a huge number of examples, can make very accurate predictions.

The seq2seq architecture (Sequence to Sequence) is very effective in OCR neural networks. It consists of two main parts – Encoder and Decoder, these are two connected neural networks training simultaneously, but performing different tasks. The encoder reads the input sequence (input data) and summarizes the information in a form called “the internal state vector”. In turn, the decoder uses these vectors and trains to generate the correct output sequence based on them.

The task of im2latex, known thanks to the OpenAI company, is to create an OCR neural network for converting math images into LaTeX language. The presented solution uses the seq2seq architecture and involves extracting features from images using convolutional layers (Encoder) and passing them to the decoder, which contains an RNN layer and trains to produce a caption in LaTeX for any mathematical image. The principle of operation of the neural network is shown in Fig. 1.

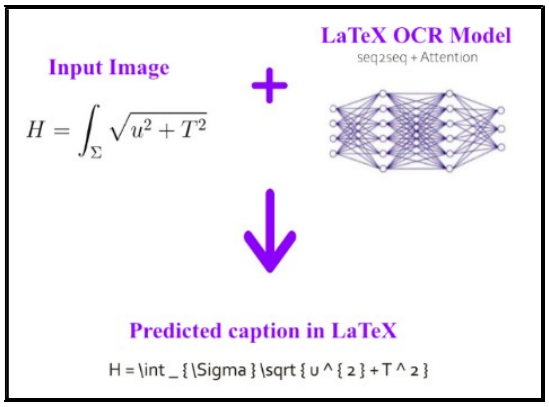

Fig. 1. Principle of im2latex

Dataset

The training data for im2latex contains 100000 images with mathematical expressions, paired with their true LaTeX label. A mandatory part of preprocessing is the separation of all individual LaTeX constructions by spaces. Fig. 2 shows several captions after this step.

```
{
    "annotations": [
        {
            "image_id": "1",
            "caption": "\\partial _ { \\mu } ( F ^ { \\mu \\nu } - e j ^ { \\mu } x ^ { \\nu } ) = 0 . "
        },
        {
            "image_id": "3",
            "caption": "x _ { \\mu } ^ { c } = x _ { \\mu } + A _ { \\mu } . "
        },
        {
            "image_id": "4",
            "caption": "s = { \\frac { S } { V } } = { \\frac { A _ { H } } { 1 _ { p } ^ { 8 } V } } =
        },
```

Fig. 2. LaTeX captions splitted by spaces

Before training, all captions are being tokenized (represented as numbers) and then a dictionary is assembled from all individual tokens (i.e., individual LaTeX words), which is used during training processes. Fig. 3 shows an array of tokenized labels.

```
[[9, 33, 5, 2, 70, 3, 11, 33, 14, ...], [9, 28, 5, 6, 148, 16, 2, 33, 3, ...], [9
> special variables
> function variables
> 00: [9, 33, 5, 2, 70, 3, 11, 33, 14, 16, 2, 13, 3, 2, ...]
> 01: [9, 28, 5, 6, 148, 16, 2, 33, 3, 2, 46, 3, 53, 7, ...]
> 02: [9, 84, 5, 6, 7, 35, 8, 11, 84, 7, 35, 8, 131, 84, ...]
> 03: [9, 106, 63, 4, 2, 51, 51, 3, 71, 11, 2, 17, 86, 6, ...]
> 04: [9, 44, 7, 107, 7, 57, 4, 58, 8, 8, 11, 37, 44, 7, ...]
> 05: [9, 107, 4, 98, 132, 88, 11, 20, 15, 10]
> 06: [9, 2, 60, 3, 4, 2, 99, 4, 21, 3, 11, 2, 13, 86, ...]
> 07: [9, 7, 29, 5, 2, 61, 3, 7, 20, 8, 15, 81, 5, 2, ...]
> 08: [9, 106, 24, 15, 55, 72, 71, 11, 106, 55, 24, 15, 55, 72, ...]
> 09: [9, 108, 4, 49, 73, 53, 74, 119, 151, 7, 17, 112, 73, 53, ...]
> 10: [9, 2, 30, 3, 11, 12, 16, 2, 13, 3, 2, 6, 22, 3, ...]
> 11: [9, 53, 4, 2, 52, 64, 52, 3, 11, 53, 4, 2, 22, 3, ...]
> 12: [9, 46, 4, 2, 31, 65, 3, 7, 66, 8, 14, 16, 2, 47, ...]
> 13: [9, 101, 7, 18, 15, 50, 135, 51, 8, 133, 16, 2, 67, 7, ...]
> 14: [9, 36, 4, 2, 58, 3, 11, 2, 2, 28, 77, 5, 6, 3, ...]
> 15: [9, 35, 4, 2, 37, 75, 55, 3, 11, 16, 2, 44, 5, 2, ...]
> 16: [9, 56, 11, 56, 5, 2, 13, 3, 4, 2, 13, 3, 14, 56, ...]
> 17: [9, 137, 7, 46, 8, 11, 12, 7, 16, 2, 93, 2, 31, 3, ...]
```

Fig. 3. Tokenized labels

Training images may have different resolutions, may contain noise, etc. These parameters must be carefully selected, since during training processes this can affect the effectiveness both for

better or worse. The highest efficiency was achieved with 300dpi images and a formula, padded to the middle (Fig. 4).

$$T^{MN}(X) = \frac{1}{\pi\gamma^* \sqrt{|G|}} \int d\tau d^p \xi \dot{x}^M \dot{x}^N \delta^D (X^M - x^M)$$

Fig. 4. Example of training image

Encoder

Encoder is a mechanism, that contains a set of convolutional and pooling layers (shown in Fig. 5) and is designed to extract features from images, which can then be used by Decoder and Attention to generate an output sequence. The number of layers and their settings are very important and may vary depending on the task. After extracting the features, Encoder summarizes it in a form called the "Internal State Vector", which is passed to Decoder.

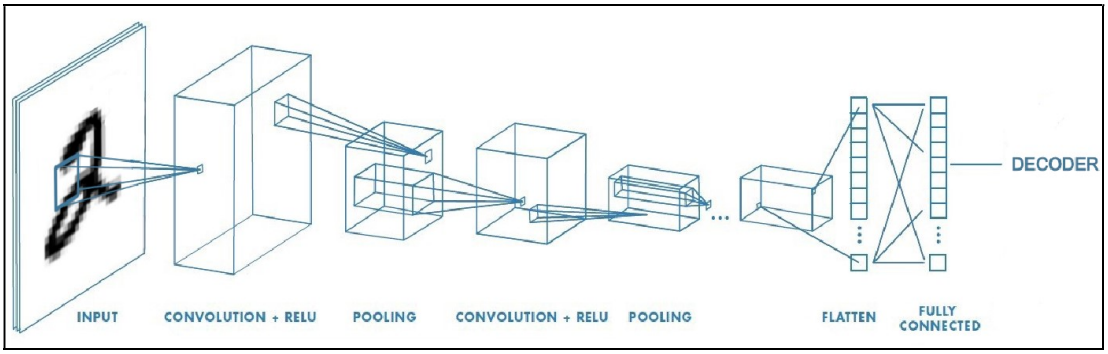

Fig. 5. Encoder architecture

Decoder

After extracting the features from input images, the decoder begins to train, which after the process is done will be able to generate captions for any image. The mechanism is based on a recurrent neural network (RNN), which is able to identify and remember important information and ignore the irrelevant one. There are several recurrent layers, the best of which are proved to be LSTM [1]. Due to the presence of a gate mechanism, LSTM, based on image features and the truth LaTeX labels, computing of which features correspond to certain LaTeX symbols, and subsequently generate an accurate label for the new image.

An important element of the decoder is the Bahdanau Attention mechanism [2]. Its essence is to generate "importance weights", called the "Context Vector", for the output sequences of the encoder (image features), which are then combined with the input data of the decoder, which allow the network to train much more efficiently. Fig. 6 shows an example of how attention mechanism works in NLP. The input data of the decoder is dataset images passed through the encoder and their real captions.

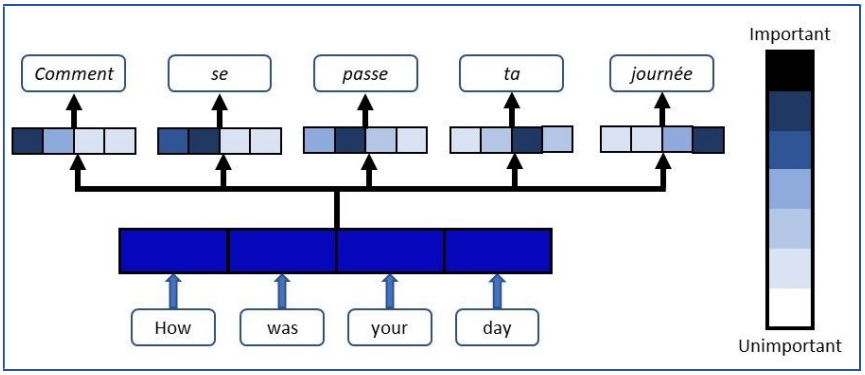

Fig. 6. Attention mechanism

Training loop

The training loop is being done for every LaTeX token of each caption and dataset image. The whole process is shown on Fig. 7 and consists of following parts:

1. Passing input images through Encoder and getting their features.
2. The decoder LSTM hidden state combined with the encoded images is being passed to the attention mechanism, which computes context vector for this training step.
3. Context vector is being concatenated with LaTeX label during this step and passed to LSTM, which generates probability distribution for each unique LaTeX token that is used during training, the higher the value, the greater the probability that the token should be after the previous one.
4. The probability distribution is being passed to the loss function (Categorical Crossentropy), which determines how far the prediction of the network is from the real caption.
5. Optimizer corrects neural network weights according to the obtained loss value.

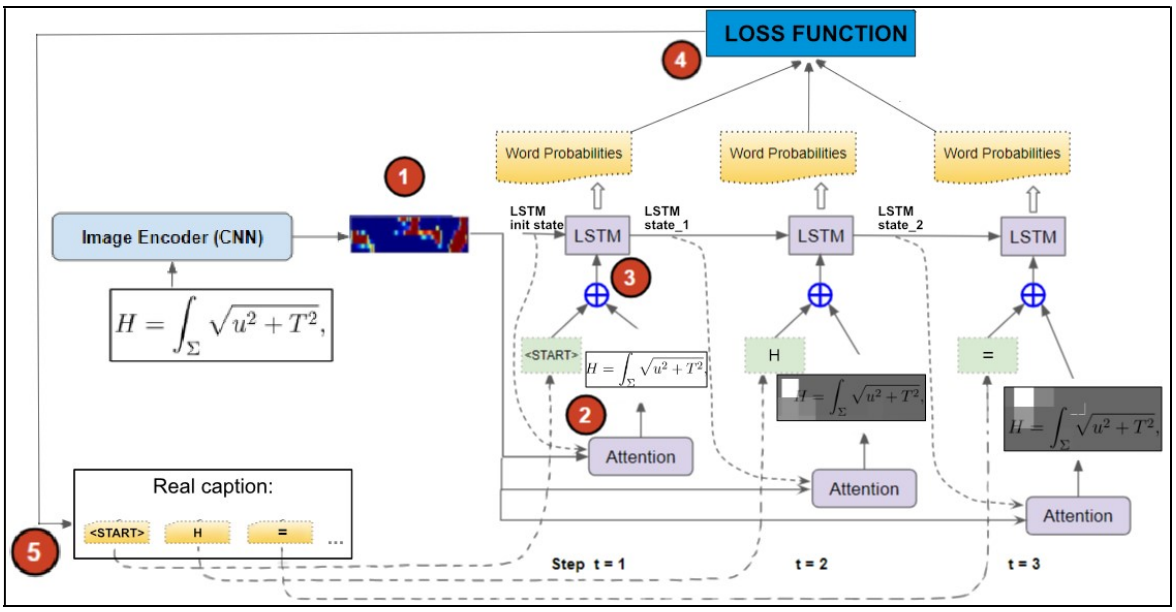

Fig. 7. Training loop

Hyperparameters

The best training results were achieved with the following parameters:

- epochs = 12
- batch_size = 24
- units = 200 (number of cells in decoder's recurrent layer)
- optimizer = Adam.

With such parameters, the network trained for about 14 hours using Nvidia RTX 3080 and 32 gigabytes of RAM. The lowest average loss obtained is 0.02, which is a good result for Image Captioning neural networks.

Evaluation

Measured BLEU [3] score is about 70 % and Levenshtein distance metric is 31. In comparison with similar works [Im2Latex. September 2019. https://github.com/luopeixiang/im2latex (on-line resource)], the obtained metric measurements are quite high. The competing solution has 40 % for BLEU against 70% of the reviewed and 44 for Minimal Edit Distance against 31. Based on the above data, it can be argued that the developed neural network has high efficiency.

Conclusion

The presented neural network with the seq2seq architecture and Attention mechanism successfully solves the im2latex problem, which is confirmed by the results of measuring metrics. Generated captions for images with equations are quite accurate and, in most cases, coincide with the real ones.

Such solution can be used in mathematical programs to automatically translate images into LaTeX and further solve and analyze the resulting equations or expressions.

References

1. Hochreiter S., Schmidhuber J. Long Short-Term Memory. *Neural Computation*. 1997;9(8):1735-1780.
2. Bahdanau D., Cho K., Bengio Y. Neural Machine Translation by Jointly Learning to Align and Translate. *3rd International Conference on Learning Representations, ICLR 2015.*
3. Papineni K., Roukos S., Ward T., Zhu W. BLEU: a method for automatic evaluation of machine translation. *ACL '02: Proceedings of the 40th Annual Meeting on Association for Computational Linguistics*, 2002: 311-318.

Authors' contribution

Vyaznikov P.A. completed dataset collection, neural network development in Python, training, and evaluation.

Kotilevets I.D. fulfilled documentation, carried out forming technical specifications, as well as technical and functional requirements.

Information about the authors

Vyaznikov P.A., Bachelor student at the Federal State Budget Education Institution of Higher Education "MIREA – Russian Technological University".

Kotilevets I.D., Senior Lecturer at the Federal State Budget Education Institution of Higher Education "MIREA – Russian Technological University".

Address for correspondence

119454, Russian Federation,
Moscow, Vernadsky Ave, 78,
Federal State Budget Education Institution of Higher Education
"MIREA – Russian Technological University";
tel. +7-499-215-65-65;
e-mail: vyaznikov.p.a@edu.mirea.ru
Vyaznikov Pavel Andreevich

http://dx.doi.org/10.35596/1729-7648-2021-19-8-45-49

Original paper

UDC 530.145.61

AB INITIO CALCULATIONS OF ELECTRONIC BAND STRUCTURE OF CdMnS SEMIMAGNETIC SEMICONDUCTORS

MATANAT A. MEHRABOVA[1], NATIG T. PANAHOV[2], NIYAZI H. HASANOV[3]

[1]*Institute of Radiation Problems of Azerbaijan National Academy of Sciences (Baku, Azerbaijan)*

[2]*Azerbaijan University of Architecture and Construction (Baku, Azerbaijan)*

[3]*Baku State University (Baku, Azerbaijan)*

Submitted 21 November 2021

Abstract. This work is devoted to theoretical investigations of $Cd_{1-x}Mn_xS$ semimagnetic semiconductors (SMSC). The purpose of this work was to calculate the electronic band structure of ideal and defective $Cd_{1-x}Mn_xS$ SMSC in both antiferromagnetic (AFM) and ferromagnetic (FM) phases. Ab initio, calculations are performed in the Atomistix Toolkit (ATK) program within the Density Functional Theory (DFT) and Local Spin Density Approximation (LSDA) on Double Zeta Double Polarized (DZDP) basis. We have used Hubbard U potential U_{Mn} = 3.59 eV for 3*d* states for Mn atoms. Supercells of 8 and 64 atoms were constructed. After the construction of $Cd_{1-x}Mn_xS$ (x = 6.25 %; 25 %) supercells and atom relaxation and optimization of the crystal structure were carried out. Electronic band structure and density of states were calculated, the total energy has been defined in antiferromagnetic (AFM) and ferromagnetic (FM) phases. Our calculations show that the band gap increases with the increase in Mn ion concentration. It has been established that Cd or S vacancy in the crystal structure leads to the change of band gap, Fermi level shifts towards the valence or conduction band.

Keywords: Ab initio calculations, DFT, semimagnetic semiconductors, electronic band structure, vacancy.

Conflict of interests. The authors declare no conflict of interests.

For citation. Mehrabova M.A., Panahov N.T., Hasanov N.H. Ab initio calculations of electronic band structure of CdMnS semimagnetic semiconductors. Doklady BGUIR. 2021; 19(8): 45-49.

Introduction

CdS is an attractive semiconductor in the photoconductive, photovoltaic, and optoelectronic materials. The dope of transition metals in nonmagnetic CdS is very important to make this material multifunctional. Room temperature CdS based SMSC, such as Mn doped CdS is a very good photo-luminance compound due to *d* states at the top of the valence band and intra-*d* shell transitions [1].

This work devoted to theoretical investigations of $Cd_{1-x}Mn_xS$ SMSC. The Mn-CdS sheet with 16 atom supercell is analyzed by Kumar S., Kumar A., Ahluwalia P.K. [2]. The electronic band structure of wurtzite CdS calculated by Rantala et al. using two different self-consistent ab initio LDA methods [3]. Nabi [4] investigated electronic and magnetic properties of Mn doped CdS in wurtzite phase, using ab-initio calculations based on Local Density Approximation (LDA), Generalized Gradient Approximation (GGA) and LDA + U exchange and correlation functionals.

Ahmed N., Nabi A., Nisar J., Tariq M., Javid M.A., and Nasim M.H. [1] investigated the electronic band structure of $Cd_{1-x}Mn_xS$ (x = 6.25 %) using spin-polarized DFT within the framework

of GGA, its extension via on-site Hubbard U interactions (GGA + U), and a model for exchange and correlation of potential Tran modified Becke-Johnson (TB-mBJ).

The purpose of this work was to calculate the electronic band structure (EBS) of ideal and defective $Cd_{1-x}Mn_xS$ SMSC in both AFM and FM phases.

Methods and results

Ab initio calculations are performed in the Atomistix Toolkit (ATK) program within the DFT and LSDA on the DZDP basis. We have used Hubbard U potential U_{Mn} = 3.59 eV for 3*d* states for Mn atoms [5, 6]. An ideal supercells of 8 (Fig. 1) and 64 (Fig. 2) atoms were constructed. After the construction of $Cd_{1-x}Mn_xS$ (x = 0; 6.25 %; 25 %) supercells, atom relaxation and optimization of the crystal structure were carried out to eliminate forces and minimize stresses. Electron band structure and density of states were calculated, the total energy has been defined in AFM and FM phases.

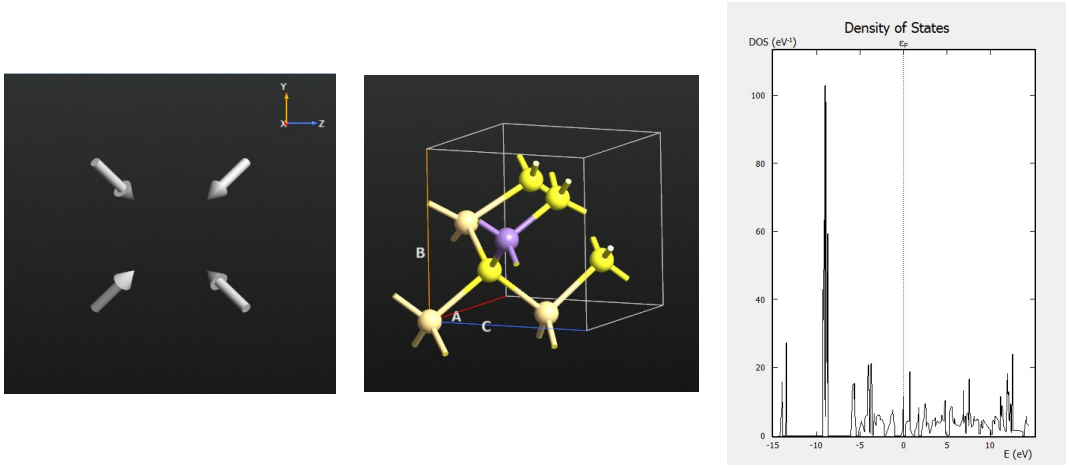

a *b* *c*

Fig. 1. $Cd_{1-x}Mn_xS$, x = 0.25 supercell: *a* – forces; *b* – bulk configuration; *c* – density of states

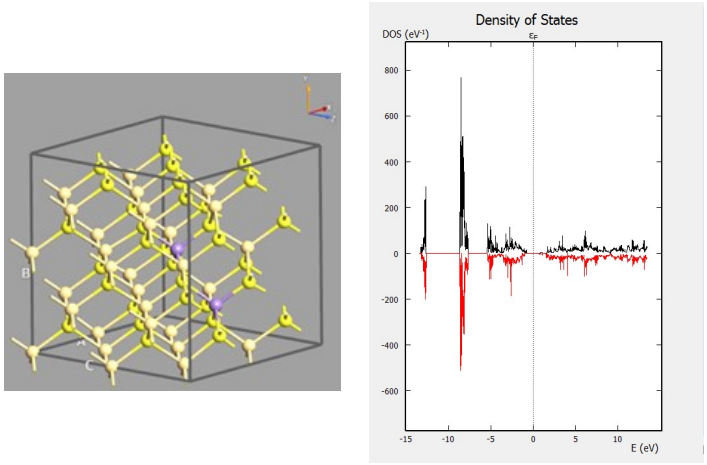

a *b*

Fig. 2. $Cd_{1-x}Mn_xS$, x = 0.0625 supercell: *a* – bulk configuration; *b* – density of states

The electron band structure of $Cd_{1-x}Mn_xS$ (x = 0.0625) SMSC is determined from the projected density of states (PDOS) (Fig. 3). The obtained PDOS plots are presented in Fig. 3. The analysis of these graphs shows that in the valence band, electron band structure of $Cd_{1-x}Mn_xS$ consists of three parts: (1) the upper part of the valence band is mainly formed by *p*-orbitals of S and Cd atoms, *s*-orbitals of Cd and Mn atoms with some contribution of *d*-orbitals of Mn atoms; (2) the middle part is formed by *d*-orbitals of Cd atoms, which are 8–9 eV lower than the valence band

maximum (3) the lower part is formed by *s*-orbitals of S and Mn atoms, *p*-orbitals of Mn atoms which are located 13 eV lower than the valence band maxim.

The bottom of the conductivity band is formed by *s*-and *p*-orbitals of Mn atoms and *p*-orbitals of Cd atoms, *d*-orbitals of S atoms (Fig. 3).

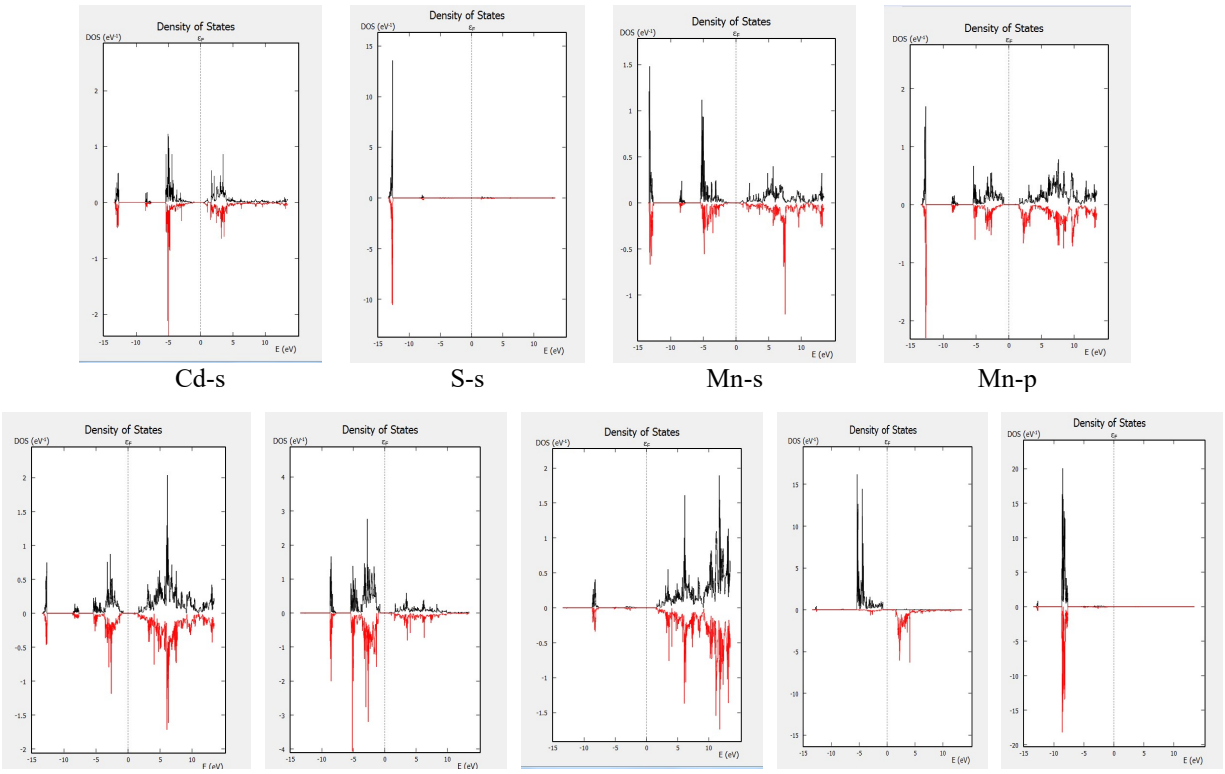

Fig. 3. PDOS of $Cd_{1-x}Mn_xS$ ($x = 0.0625$) SMSC

The band gap for the $Cd_{1-x}Mn_xS$ with $x = 0.25$ supercells is equal to $E_g = 1.6$ eV and total energy is equal to $E_t = -6698.61546$ eV. For the $x = 0.0625$ supercell band gap is equal to $E_g = 1.25$eV and total energy is equal to $E_t = 59267.92943$ eV.

EBS and DOS of the defective $Cd_{30}Mn_2Se_{32}$ supercell are calculated. We consider vacancy type as a defect. Atom relaxation and optimization of the crystal structure were carried out, forces and stresses were minimized (Fig. 4).

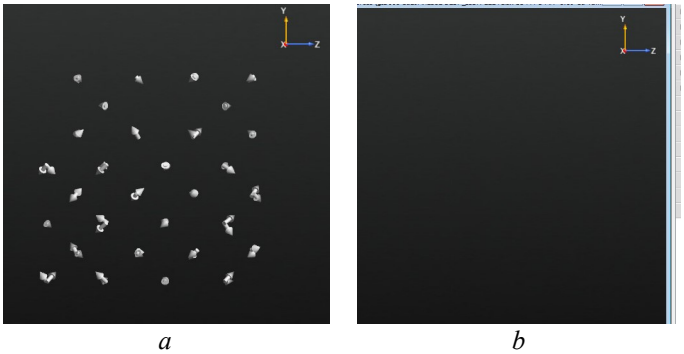

a *b*

Fig. 4. Forces: *a* – before optimization; *b* – after optimization

In the case of S vacancy (V_S), the band gap is $E_g = 1.3$ eV, the total energy equals $E_t = -58907.646$ eV (Fig. 5); for Cd vacancy (V_{Cd}) the band gap is $E_g = 1.55$ eV, the total energy is $E_t = -57712.50684$ eV (Fig. 6). It can therefore be concluded that the Cd or S vacancy in a crystal leads to an increase in the band gap, as a change in the total energy occurs, the Fermi level shifts towards the valence or conduction band.

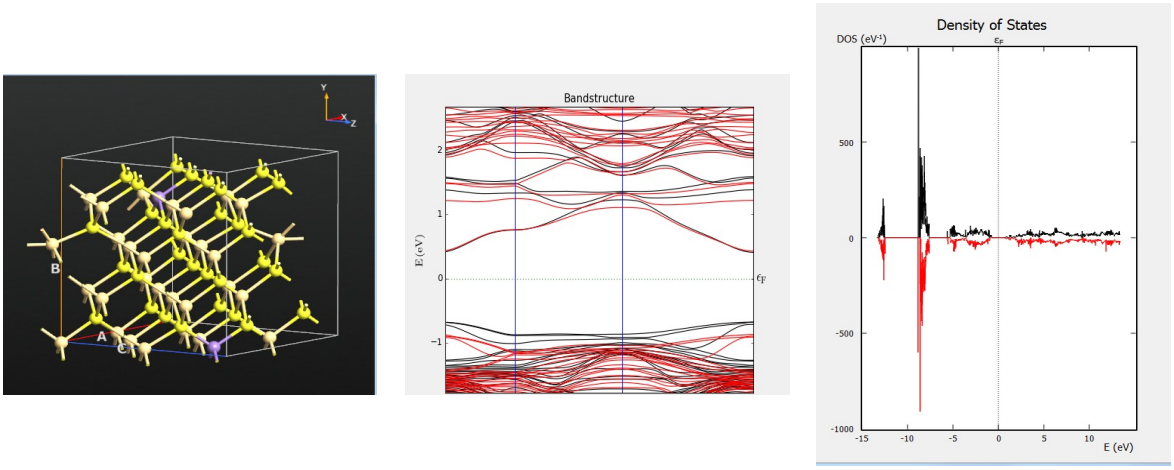

a *b* *c*

Fig. 5. S vacancy in $Cd_{1-x}Mn_xS$, $x = 0.625$; *a* – bulk configuration; *b* – EBS; *c* – DOS

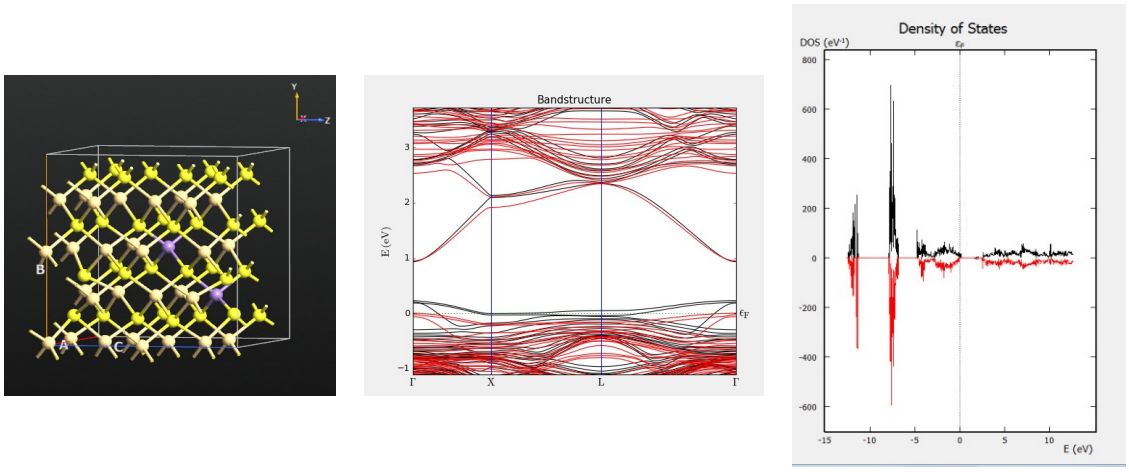

a *b* *c*

Fig. 6. Cd vacancy in $Cd_{1-x}Mn_xS$, $x = 0.625$; *a* – bulk configuration; *b* – EBS; *c* – DOS

Conclusion

Ab initio calculations have been performed to analyze the electronic band structure of an ideal and defective $Cd_{1-x}Mn_xS$ SMSC ($x = 0.25$; 0.0625). It has been defined that with an increase in Mn ion concentration in the $Cd_{1-x}Mn_xS$, there is an increase in the band gap and an increase in the total energy. The calculations show that the defects as a vacancy in a crystal lead to an increase in the band gap, decrease in the total energy, shifting of the Fermi level towards the valence or conduction ban.

References

1. Ahmed N., Nabi A., Nisar J., Tariq M., Javid M.A., Nasim M.H. First principle calculations of electronic and magnetic properties of Mn-doped CdS (zinc blende): a theoretical study. *Materials Science-Poland*. 2017;35(3):479-485.
2. Kumar S., Kumar A., Ahluwalia P.K. First principle study of manganese doped cadmium sulphide sheet *AIP Conference Proceedings, AIP.* New York; 2014.
3. Rantala T.T., Rantala T.S., Lantto V., Vaara J. Surface relaxation of the (1010) face of wurtzite CdS. *Surface Science.* 1996;352-354:77-82.
4. Nabi A. The electronic and the magnetic properties of Mn doped wurtzite CdS: First-principles calculations. *Computer Matererial Science A.* 2016: 210-218.
5. Mehrabova M.A., Orujov H.S., Hasanov N.H., Kazimova A.I., Abdullayeva A.A. Ab Initio Calculations of Defects in CdMnSe Semimagnetic Semiconductors. *Mechanics of Solids*. 2020;55(1):108-113.
6. Mehrabova M.A., Hasanov N.H., Huseynov N.I., Kazimova A.I. “Ab initio calculations of defects in $Cd_{1-x}Mn_xTe(Se)$ semimagnetic semiconductors. *Journal of Radiation Researches.* 2020;7(2):39-42.

Authors' contribution

Mehrabova M.A. and Panahov N.T. carried out calculations in the program.

Hasanov N.H. defined the objectives of the research, took part in the preparation of the text of the article, and interpretated the results of the experiments.

Information about the authors

Mehrabova M.A., D.Sc., Associated Professor, Leading Researcher at the Institute of Radiation Problems of Azerbaijan National Academy of Sciences.

Panahov N.T., PhD., Associated Professor, Leading Researcher at the Azerbaijan University of Architecture and Construction.

Hasanov N.H., Lecturer at the Department of Physics of Baku State University.

Address for correspondence

AZ1143, Azerbaijan,
Baku, B.Vahabzade St., 9,
Institute of Radiation Problems of ANAS;
tel. +994-50-731-81-77;
e-mail: m.mehrabova@science.az
Mehrabova Matanat Ahmed

http://dx.doi.org/10.35596/1729-7648-2021-19-8-50-57

Original paper

UDC 621.383.52

MODELING AlGaN *P-I-N* PHOTODIODES

NIKOLAI N. VORSIN, ANATOLII A. GLADYSHCHUK, TATSIANA L. KUSHNER, NIKOLAI P. TARASIUK, SERGEY V. CHUGUNOV, MARINA V. BORUSHKO

Brest State Technical University (Brest, Republic of Belarus)

Submitted 21 November 2021

Abstract. Ternary AlGaN alloys with a band gap of 3.4 to 6.2 eV are very promising for photodetectors in the UV wavelength range. Using the COMSOL MULTIPHYSICS software based on AlGaN, a *p-i-n* photodiode model was developed, including its *I–V* characteristic, spectral sensitivity of the received radiation, absorption coefficient as a function of the aluminum fraction and the depletion layer thickness. To calculate the process of interaction of a semiconductor with EM radiation, we used a model based on the use of an element of the transition matrix through the carrier lifetime during spontaneous recombination. In this case, the peak sensitivity of the photodiode is from 0.08 to 0.18 A/W at wavelengths of 0.2–0.33 μm. This is in line with experimental results taken from the relevant literature.

Keywords: photodetector, two-dimensional model, *p-i-n* structure, numerical simulation.

Conflict of interests. The authors declare no conflict of interests.

For citation. Vorsin N.N., Gladyshchuk A.A., Kushner T.L., Tarasiuk N.P., Chugunov S.V, Borushko M.V. Modeling AlGaN *p-i-n* photodiodes. Doklady BGUIR. 2021; 19(8): 50-57.

Introduction

III-nitride compound materials that consist of InN, GaN, AlN, and their alloys are semiconductors with interesting physical properties such as high electron mobility, high carrier saturation rate, good thermal stability and conductivity, direct and variable width forbidden zone with a high coefficient of optical absorption.

The absorption coefficient of III-nitride materials is over 10^4 cm^{-1} [1]. A significant fraction of light penetrates as deep as several hundred nanometers into the absorbing region. The band gap of the $Al_xGa_{1-x}N$ (AlGaN) material varies from 3.4 eV to 6.2 eV depending on the x proportion of aluminum in the $Al_xGa_{1-x}N$ compound [2, 3]. Due to these physical properties, III-nitride semiconductors are promising materials to implement numerous optoelectronic devices such as LEDs, laser diodes, solar cells, and photodiodes.

Most modern photodiodes are based on a *p-i-n* structure. Photons absorbed in the region of their own conductivity (*i*-layer) generate electron-hole pairs, which are then separated by an electric field, thus creating a load current. Multiple quantum wells (MQW) [4] or superlattice structures [4] contained in nanometer AlGaN layers can be used as additional factors for bulk structures to improve crystal quality of active layers and increase sensitivity of photodiodes.

In the late 2000s E. Berkman et al. [5] developed a *p-i-n* photodiode InGaN which showed a sensitivity of 37 mA/W at the wavelength of 426 nm. Then the sensitivity parameter improved

rapidly with each new development. A year later, Su et al. [6] produced a *p-i-n* photodiode with its own $In_{0.11}Ga_{0.89}N$ active layer and the highest spectral sensitivity of 0.206 A/W at a wavelength of 380 nm. This figure was surpassed by Lu Y., Zhang Y., Li X.Y. [7] who reported a peak sensitivity of 0.22 A/W at 378 nm in an unbiased *p-i-n* photodetector.

All the achievements mentioned above are related to the region of violet and near ultraviolet range. As the wavelength shortens, the achievable sensitivity index should decrease because an increase in photon energy at a constant value of radiation power means a decrease in the density of photon flux. Therefore, at the wavelength of 200 nm one should expect half the sensitivity indicator, i. e. about 0.1 A/W. The authors of this work have made an attempt to model *p-i-n* photodiodes based on the AlGaN triple compound with the use of COMSOL MULTIPHYSICS software [8]. Based on the constructed model, they determined dependences of the photodiodes characteristics on such parameters as molar fraction of aluminum and thickness of the layer with intrinsic conductivity (*i*-layer). The information obtained from the models was used to develop a UV photodetector with a maximum spectral sensitivity at the wavelength of 0.24 μm. The simulation results presented in this work can be used to optimize AlGaN/GaN photodetectors and develop a new generation of optoelectronic devices.

Photodiode structure and numerical model

The structure shown in Fig. 1 is typical of nitride photodiodes.

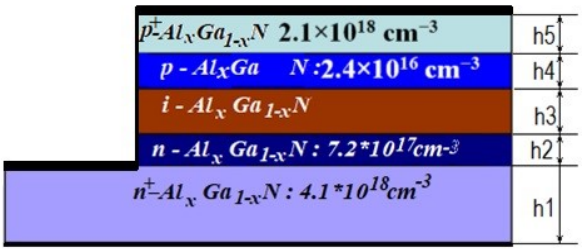

Fig. 1. Photodiode structure

Between the *n* and *p* layers which have moderate electron and hole conductivity there is a pretty thick *i*-layer with its own conductivity where most light is absorbed and converted into free charge carriers. This three-layer structure is complemented with highly doped *n*+ and *p*+ layers at the top and bottom which make it possible to obtain omic contacts with metallic leads shown in thick lines in the figure.

The lower *n*+ layer solves some other problems except for contacting the leads. It reduces an intergrowth of dislocations from a contact with the substrate into the overlying layers and compensates for errors in the etching depth of the upper layers when separating diodes. Therefore, the lower *n*+ layer is much thicker than the others. It is applied on an AlN buffer layer which, in turn, rests on a sapphire substrate.

Thicknesses of the h1–h5 layers are parameters that can be easily changed before the model is calculated. The lower *n*+ region is made wider than the rest of the structure and the omic contact is made from above the protruding part.

The applied two-dimensional model is shown in Fig. 1. Taking into account the same processes along the horizontal axis, the model is actually one-dimensional, which simplifies the calculation. The COMSOL MULTIPHYSICS "optoelectronics" module solves a number of basic semiconductor equations, including the Poisson equation, the continuity equation, and the transport equations for electrons and holes. In addition, it offers several modern physical models for the interaction of a semiconductor with EM radiation.

The band gap E_g for $Al_xGa_{1-x}N$ at room temperature is calculated by using the well-known formula [9] which approximates the actual dependence of E_g on *x* molar fraction of aluminum by the quadratic dependence:

$$E_g^{AlGaN} = xE_g^{AlN} + (1 - x)\,E_g^{GaN} - 1.1x(1 - x). \quad (1)$$

The values of the AlN and GaN band gap are: $E_g^{AlN} = 6.2$ eV [11] and $E_g^{GaN} = 3.42$ eV [10].

It is known that electronic affinity potential of AlGaN decreases as the fraction of aluminum increases and the band gap increases according to a law close to a linear one. The calculation is based on the following formula from [11]

$$\chi = 4.1 + 0.7\left(Eg^{GaN} - Eg^{AlGaN}\right). \quad (2)$$

Effective densities of the states in the conduction and valence bands are approximated by linear dependences on the fraction of aluminum [11]:

$$N_c^{AlGaN} = \left(\frac{T}{1K}\right)^{3/2} \left(1.8x + 4.6(1-x)\right)\cdot 10^{14}\,\text{cm}^{-3};$$
$$N_v^{AlGaN} = \left(\frac{T}{1K}\right)^{3/2} \left(10.6x + 9.2(1-x)\right)\cdot 10^{15}\,\text{cm}^{-3}. \quad (3)$$

The permittivity constant ε and the relative effective masses of electrons (holes), m_e (m_h), are also assumed to depend linearly on the fraction of aluminum and determined as [11]:

$$\varepsilon^{AlGaN} = 10.1x + 10.4\,(1-x);$$
$$m_e^{AlGaN} = 0.314x + 0.2\,(1-x); \quad (4)$$
$$m_h^{AlGaN} = 0.417x + 1.0\,(1-x).$$

There are temperature-dependent models of carrier mobility in nitride materials in weak and strong fields. However, since the calculation was carried out only at room temperature (293 K), the temperature dependence was excluded from the formulas. This makes it possible to use a simpler expression for the electron mobility:

$$\mu_e(N,x) = \mu(x)_{\min} + \frac{\mu(x)_{\max} - \mu(x)_{\min}}{1 + \left(\frac{N_{tot}}{N_{ref}}\right)^{\alpha(x)}}, \quad (5)$$

where x is fraction of aluminum, $N_{ref} = 10^{17}$ cm^{-3} is reference impurity concentration, N_{tot} is total concentration of impurities in a given area of the crystal. The values of the $\mu(x)_{max}$, $\mu(x)_{min}$ and $\alpha(x)$ parameters obtained experimentally in [11] are presented in the following Tab. 1.

Table 1. The values of the $\mu(x)_{max}$, $\mu(x)_{min}$ and α

Material	μ_{min} cm^2/(V.s)	μ_{max} cm^2/(V.s)	α
GaN	295.0	1460.7	0.66
$Al_{0.2}Ga_{0.8}N$	132.0	306.1	0.29
$Al_{0.5}Ga_{0.5}N$	41.7	208.3	0.12
$Al_{0.8}Ga_{0.2}N$	47.8	199.6	0.17
AlN	297.8	683.8	1.16

In the region with intrinsic conductivity $N_{tot} = 0$, the electron mobility coincides with the maximum value: $\mu_e = \mu_{max}$. This value was calculated using the approximating formula, which provides an exact match at the five points given in the table: $\mu_e = 18475x^4 - 40696x^3 + 32168x^2 - 10723x + 1460$.

The hole mobility is taken equal to 5 cm^2 V^{-1} s^{-1} [10]. As the band gap of AlGaN is quite wide, the main mechanism of carrier loss in AlGaN is defect-mediated recombination. The calculations take into account two recombination models. The first one is a simplified Shockley–Read–Hall (SRH) model of recombination on defects (traps) where one energy level is assigned to the traps while other characteristics, including the concentration of defects, are expressed by the lifetimes of electrons and holes. This time is assumed as equal to 1 ns, and the energy level of defects is taken near the middle of the band gap. The second type taken into account is direct recombination with the parameter C = 10^{-8}cm^{-3}s^{-1} [8].

COMSOL MULTIPHYSICS offers several models of optical generation and carrier recombination. We applied a model based on the calculation of a transition matrix element using the carrier lifetime with spontaneous recombination, which was taken equal to τ_{spon} = 1 ns. The element of the transition matrix is also highly dependent on the n refractive index of the material. The value of the latter, in turn, is a function of the wavelength λ. This dependence can be approximately described by the Sellmeier dispersion equation:

$$n^2(\lambda) = 1 + \frac{A_0}{1 - \left(\frac{\lambda_0}{\lambda}\right)^2}, \tag{6}$$

where the A_0 and λ_0 constants are determined by the band gap and approximated for nitride compounds by the following expressions [1]:

$$\begin{aligned} A_0 &= 6.626 - 0.934E_g + 0.0598E_g^2; \\ \lambda_0 &= (396.8 - 84.12E_g + 6.758E_g^2)[\text{nm}]. \end{aligned} \tag{7}$$

The band gap in these formulas is in eV and the wavelength is in nm.

COMSOL MULTIPHYSICS calculates many quantities, including the magnitude of the absorption coefficient and its spectral behavior α(λ) which can be easily recalculated into the extinction coefficient:

$$k(\lambda) = \frac{a(\lambda)\lambda}{4\pi}. \tag{8}$$

Numerical modeling was carried out for the AlGaN *p-i-n* photodiode at 293 K. The width of the diode was assumed to be 20 μm, its thickness is the depth size of 1 m. The thickness is chosen taking into account that the absolute value of electromagnetic power in a two-dimensional problem is considered to be distributed in depth per unit of length, i. e. at 1 m.

Results and discussion

COMSOL MULTIPHYSICS calculates a number of characteristics of simulated processes and has a very rich toolkit to represent the results. The most illustrative one is the graphical form used below. Fig. 2 shows a graph of impurity dopants distribution for 2 μm thickness of depletion layer. Acceptor impurity corresponds to positive values while donor impurity corresponds to the negative ones. There is no doping in the thickness range from 0.15 to 2.15 μm. We have a layer with its own conductivity that absorbs radiation incident on it.

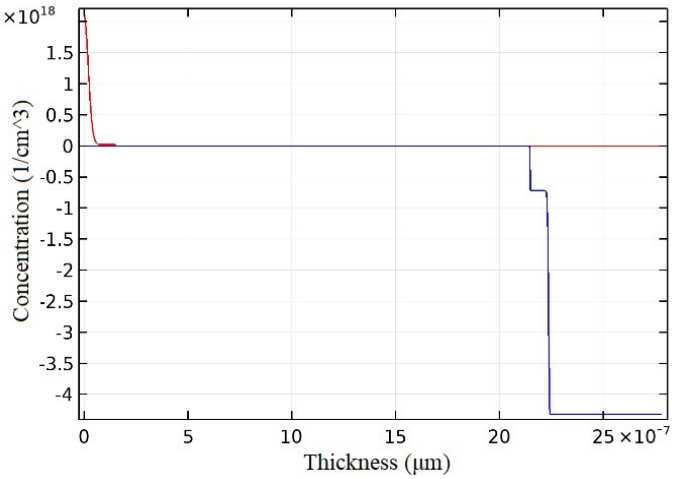

Fig. 2. Impurity dopants distribution for a 2 μm thickness of depletion layer

The main parameters of the photodetector are a coefficient of conversion of the incident light power into electric current (watt-ampere characteristic) and dependence of this coefficient on the length of the light wave (spectral characteristic).

Fig. 3 shows the graphs obtained as a result of calculation. They reveal how the photocurrent value depends on the light wavelength (lambda) and the molar fraction of aluminum (x) in the i-layer at an incident light power of 1 W. The calculation was carried out for the 0.2 μm i-layer and the reverse voltage applied to the photodiode $V_n = 1$ V. Depending on x, the maximum of the spectral characteristic falls on the wavelengths from $\lambda = 0.2$ μm to 0.32 μm. In this case, the maximum of the watt-ampere characteristic is $k = 0.085$ A/W in the short-wave part of the range, with $x = 0.8$, in the long-wave part $k = 0.175$ A/W, with $x = 0$.

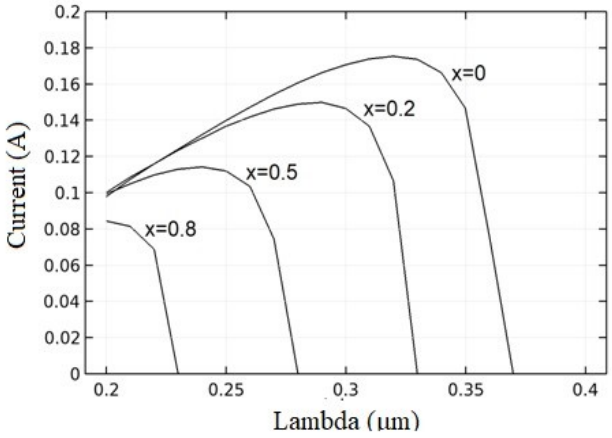

Fig. 3. The photocurrent as function of light wavelength for different x of aluminum in the i-layer

It is quite obvious that the spectral characteristic decreases as the light wavelength reduces. It happens if the photon flux density decreases while the value of the incident light power is constant and the photon energy increases. Moreover, the applied model of the frequency dependence of the Sellmeier refractive index determines its increase as the light wavelength decreases. An increase in the refractive index results in a decrease in the transition matrix element in the light absorption model and a corresponding decrease in the light absorption.

Fig. 4 shows dispersion graphs of the AlGaN absorption coefficient with different values of aluminum fraction. It is surprising that until now there are no generally accepted values of this quantity for AlGaN in the region of its absorption of the light power. According to some papers [12], its value α is more than 10^5 cm^{-1}, but according to other [13], it is about $1.8 \cdot 10^4$ cm^{-1}. The values of α obtained in our modeling quite confirm the latter value. However, it is not obvious that the applied model of a semiconductor interacting with radiation takes into account all the mechanisms of this process.

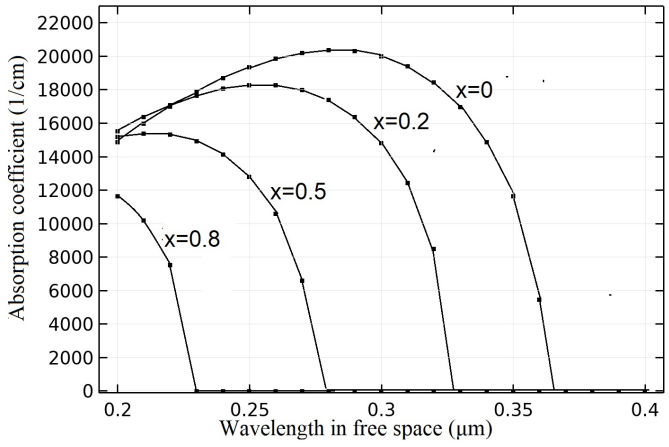

Fig. 4. Dispersion graphs of the AlGaN absorption coefficient with different values x of aluminum fraction

The intersection of graphs at the wavelength of 0.23 μm is still explained by the refractive index dispersion of the material. It affects the value of the transition matrix element more at the lower x than at the higher ones. One of the important issues in creating *p-i-n* photodiodes is choosing a thickness of the absorbing *i*-layer. There are some physical grounds to expect an optimum of this value according to some criteria. For example, on one hand the thicker the *i*-layer is, the higher the absorption of light power, but, on the other hand, it makes the path of photocarriers longer and increases their losses due to recombination.

This allows us to assume that there is an optimum of the maximum conversion coefficient. Fig. 5 shows graphs of the watt-ampere characteristics calculated for $x = 0$ (pure GaN) with various thicknesses of the *i*-layer (h3). It can be seen in these graphs that a change in the thickness of the *i*-layer from 50 to 3200 nm (64 times) increases the maximum photocurrent from 0.07 to 0.23 A (approximately 3 times). In this case, the main increase in the photocurrent falls on the thickness range from 200 to 800 nm. Apparently, this range of *i*-layer thicknesses is the best to realize the highest conversion coefficient. However, the maximum sensitivity is not detected by the thickness of the *i*-layer. The graph curve slowly reaches 0.23 A/W and then goes almost horizontally.

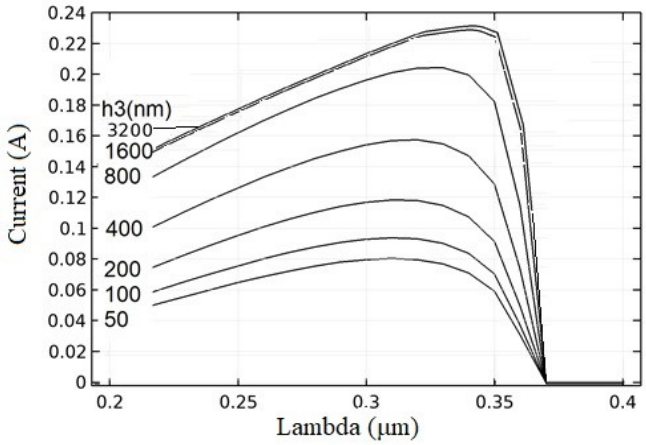

Fig. 5. Watt-ampere characteristics calculated for GaN

A volt-ampere characteristic (CVC) of a photodiode can be easily constructed with the COMSOL MULTIPHYSICS software because it is not necessary to take into account any interaction with luminous flux. The graphs of a straight edge with different values of the x proportion of aluminum in the solid solution are shown at Fig. 6.

The course of the graphs is obvious as an increase in x leads to an increase in the band gap, and this, in turn, decreases the reverse current and shifts the CVC graph to the right. What is of special interest is the value of direct voltage when a noticeable direct current appears. Let's call it U_x. Then $U_0 = 3.2$ V, $U_{0.2} = 3.53$ V, $U_{0.5} = 4.51$ V, $U_{0.8} = 5.2$ V.

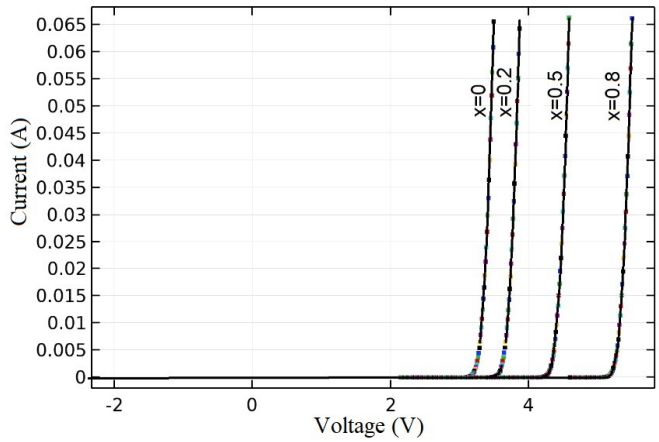

Fig. 6. Straight edge with different values of the x proportion of aluminum in the solid solution

Conclusion

The new numerical model using the COMSOL MULTIPHYSICS software to estimate *I–V* curve, spectral sensitivity, absorption coefficient, and other parameters as a function of the proportion of aluminum in the AlGaN alloy and the thicknesses of the layers forming *p-i-n* photodiode based on AlGaN [14, 15] is proposed in the article. This model was able to calculate the voltage and current dependency similar to a device simulation as a continuous solution and could be useful for device development as a quick calculation. It could be also useful to academical and educational understanding the behavior of the electrical characteristics.

References

1. Zayac N.S., Gencar' P.A., Bojko V.G., Litvin O.S. Opticheskie svojstva plenok GaN/Al2O3, legirovannyh kremniem. *Fizika i tekhnika poluprovodnikov*. 2009;43(5):617-620.
2. Mohammad S.N., Morkos Y.H. Progress and prospects of group-III nitride semiconductors. *Progress in Quantum Electronics*. 1996;20;361. DOI: org/10.1016/S0079-6727(96)00002-X.
3. Ambacher O. Growth and applications of Group III-nitrides. *Appl. Phys.* 1998;31;2653. DOI: org/10.1088/0022-3727/31/20/001.
4. Yang C.C., Sheu J.K., Liang X.W., Huang M.S., Lee M.L., Chang K.H., Tu S J., Huang F.-W., Lai W.C. Enhancement of the conversion efficiency of GaN-based photovoltaic devices with AlGaN/InGaN absorption layers. *Appl. Phys. Lett.* 2010;97;021113-1. DOI: org/10.1063/5.0019576.
5. Berkman E., El-Masry N., Emara A., Bedair S. Nearly lattice-matched n, i and p layers for InGaN *p-i-n* photodiodes in the 365-500 nm. *Appl. Phys. Lett.* 2008;92;101118. DOI: org/10.1063/1.2896648.
6. Su Y.K., Lee H.C., Lin J.C., Huang K.C., Lin W.J., Li T.C., Chang K.J. $In_{0.11}Ga_{0.89}N$-based *p-i-n* photodetector. *Phys. Status Solidi C.* 2009;6;S811. DOI: org/10.1002/pssc.200880757.
7. Lu Y., Zhang Y., Li X.Y. Properties of InGaN *P-I-N* ultraviolet detector. In: *Proc. SPIE 9284, 7th International Symposium on Advanced Optical Manufacturing and Testing Technologies: Optoelectronics Materials and Devices for Sensing and Imaging*. 2014; 928401. DOI: 10.1117/12.2073317.
8. "COMSOL MULTIPHYSICS Modeling Software". COMSOL MULTIPHYSICS.com. COMSOL MULTIPHYSICS, Inc. Retrieved 20 November 2015.
9. Nikonov A.P., Boltar' K.O., YAkovleva N.I. Opticheskie svojstva geteroepitaksial'nyh sloev AlGaN. *Prikladnaya fizika*. 2014;2:50-52.
10. Kuej R.. *Elektronika na osnove nitrida galliya*. Moskow: Tekhnosfera; 2011: 582.
11. ATLAS User's Manual, Device Simulation Software, Version 5.20.2. R, SILVACO International, Santa Clara, CA, 2016.
12. Hirsch L., Barriere A.S. Electrical characterization of InGaN/GaN light emitting diodes grown by molecular beam epitaxy. *Journal of Applied Physics.* 2003;94(8):5014. DOI: org/10.1063/1.1605252.
13. Mott N. *Elektronnye processy v nekristallicheskih veshchestvah*. Moskow: Mir; 1982.
14. Vorsin N.N., Gladyshchuk A.A., Kushner T.L., Tarasiuk N.P., Chugunov S.V. *Modelirovanie i razrabotka AlGaN p-i-n fotodiodov*. *Vestnik BrGU*. 2018;4:5-14.
15. Lutsenko E.V., Danilchyk A.V, Tarasuk N.P., Andryeuski A., Pavloskii V.N., Gurskii A.L., Yablonskii G.P., Kalish H., Jansen R.H., Dikme Y., Schineller B., Heuken M. Laser threshold and optical gain of blue optically pumped InGaN/GaN multiple quantum wells (MQW) grown on Si. *Phys. Stat. Sol. (c)*. 2008;5(6):2263-2266. DOI: 10.1002/pssc.200778673.

Authors' contribution

Vorsin N.N. performed the task for the study, contributed to creating the models and discussing the research results, as well as prepared the manuscript of the article.

Gladyshchuk A.A. performed the task for the study, contributed to discussing the research results.

Kushner T.L. did the literature review, contributed to the research results discussion, and prepared the manuscript of the article.

Tarasiuk N.P. contributed to modeling the photodiodes structure, solving math models, and discussing the research results, prepared the manuscript of the article.

Chugunov S.V. contributed to modeling the photodiodes structure, solving math models, and discussing the research results.

Borushko M.V. did the literature review and prepared the manuscript of the article.

Information about the authors

Vorsin N.N., PhD., Associate Professor, Assistant Professor at Physics Department of Brest State Technical University.

Gladyshchuk A.A., PhD., Associate Professor, Assistant Professor at Physics Department of Brest State Technical University.

Kushner T.L., PhD., Associate Professor, Head of Physics Department of Brest State Technical University.

Tarasiuk N.P., Senior Lecturer at Brest State Technical University.

Chugunov S.V., Senior Lecturer at Brest State Technical University.

Borushko M.V., Senior Lecturer at Brest State Technical University.

Address for correspondence

224017, Republic of Belarus,
Brest, Moskovskaya St., 267,
Brest State Technical University;
tel. +375-29-222-35-95;
e-mail: phys@bstu.by
Tarasiuk Nikolai Petrovich

http://dx.doi.org/10.35596/1729-7648-2021-19-8-58-62

Original paper

UDC 535.21:534

PHOTOACOUSTIC EFFECT IN MICRO- AND NANOSTRUCTURES: NUMERICAL SIMULATIONS OF LAGRANGE EQUATIONS

OLEG G. ROMANOV, YAKOV K. SHTYKOV, IGOR A. TIMOSHCHENKO

Belarusian State University (Minsk, Republic of Belarus)

Submitted 22 November 2021

Abstract. The work provides the description of theoretical and numerical modeling techniques of thermomechanical effects that take place in absorbing micro- and nanostructures of different materials under the action of pulsed laser radiation. A proposed technique of the numerical simulation is based on the solution of equations of motion of continuous media in the form of Lagrange for spatially inhomogeneous media. This model allows calculating fields of temperature, pressure, density, and velocity of the medium depending on the parameters of laser pulses and the characteristics of micro- and nanostructures.

Keywords: short laser pulses, nanoacoustics, Lagrange equations, numerical simulations.

Conflict of interests. The authors declare no conflict of interests.

For citation. Romanov O.G, Shtykov Y.K, Timoshchenko I.A. Photoacoustic effect in micro- and nanostructures: numerical simulations of Lagrange equations. Doklady BGUIR. 2021; 19(8): 58-62.

Introduction

The photoacoustic effect is the formation of sound waves due to pulsed heating of the absorbing medium upon the absorption of electromagnetic radiation. Currently, the photoacoustic effect is widely used in biomedical research [1], photoacoustic spectroscopy [2], and other applications. The studies of the interaction of pulsed laser radiation with absorbing micro- and nanostructures are of particular interest. The absorption of laser pulse energy in micro- and nanostructures makes it possible to excite acoustic vibrations in the frequency range from gigahertz to terahertz. Such oscillations are of particular interest for fundamental research and have many potential applications (acoustic visualization of nanoobjects, acoustic nanocavities, phonon crystals) [3–7].

This work is devoted to the development of a technique for modeling the problems of thermooptical excitation of acoustic vibrations in absorbing micro- and nanostructures, based on the numerical solution of the equations of motion of continuous media in the Lagrange form. Using the developed technique, the problems of excitation of ultra high-frequency oscillations in spherical micro- and nanoparticles of various materials are considered.

Theoretical model

The Lagrange equations for one-dimensional spherically symmetric motion of a continuous medium have the following forms [8]:

– equation of continuity:

$$V = V_0 \left(\frac{R}{r} \right)^2 \frac{\partial R}{\partial r}; \tag{1}$$

– equation of motion:

$$\frac{\partial u}{\partial t} = -V_0 \left(\frac{R}{r} \right)^2 \frac{\partial P}{\partial r}; \tag{2}$$

– equation of the Euler coordinate R change:

$$\frac{\partial R}{\partial t} = u. \tag{3}$$

Here V_0, V are the initial and current specific volumes $V_0 = 1/\rho_0$, $V = 1/\rho$, where ρ_0, ρ are the corresponding densities, r is the Lagrangian coordinate, t is the time.

As an equation of state in the problems under consideration, it is advisable to use the Mie – Grüneisen equation in its two-term form [9]:

$$P = \rho_0 u_0^2 \left(1 - \frac{V}{V_0} \right) + \Gamma \frac{C_V (T - T_0)}{V}. \tag{4}$$

Here $\Gamma = \frac{u_0^2 \beta}{C_V}$ is the Grünheisen coefficient, β is the volume expansion coefficient, C_V is the heat capacity, and u_0 is the sound speed in the medium.

To find the change in the temperature of the medium, we will use the following heat conduction equation:

$$\rho C_V \frac{\partial T}{\partial t} = k_h \frac{1}{r^2} \frac{\partial}{\partial r} \left(r^2 \frac{\partial T}{\partial r} \right) + Q_S. \tag{5}$$

Here k_h is the coefficient of thermal conductivity of the medium. The quantity Q_S is determined by the source of energy release: $Q_S = k_{abs} I(r,t)$, where k_{abs} is the absorption coefficient of the medium, $I(t,r) = I_0 f_t(t) f_r(r)$ is the intensity of the light beam. A power-exponential function $f_t(t) = t/t_p e^{-t/t_p}$ was chosen as the temporal shape of the laser pulse, where t_p is the duration of the laser pulse; the spatial function has the form $f_r(r) = \begin{cases} 1, r \le R_0 \\ 0, r > R_0 \end{cases}$, which, in the case of the spherical geometry of the absorbing particle, corresponds to a sphere of radius R_0.

The solution of the system of equations (1) – (5) makes it possible to calculate the space-time dependences of pressure, temperature, density, and velocity, to estimate the contribution of thermal and acoustic mechanisms to the change in the physical parameters of a continuous medium. Note that if it is necessary to describe thermomechanical phenomena in metallic nanostructures under the action of ultrashort laser pulses, this approach should be supplemented with the usage of a two-temperature model of metal heating, which makes it possible to study processes at times shorter than the electron-phonon relaxation time. In this case, the heat equation takes the following form [10]:

$$\rho_e C_e \frac{\partial T_e}{\partial t} = k_h^e \frac{1}{r^2} \frac{\partial}{\partial r}\left(r^2 \frac{\partial T_e}{\partial r} \right) + Q_S - \gamma\left(T_e - T_i\right); \quad (6)$$

$$\rho_i C_i \frac{\partial T_i}{\partial t} = \gamma\left(T_e - T_i\right). \quad (7)$$

Here the values ρ (density), C (heat capacity), T (temperature), k_h (thermal conductivity) with the index "*e*" refer to the electronic subsystem, with the index "*i*" – to the ionic one. The parameter γ determines the rate of energy relaxation from the electron gas to the ions of the crystal lattice.

To approximate the equation of state of a metal nanoparticle, we use the Mie – Grüneisen equation, which, taking into account the separation of two subsystems (electronic and ionic), takes the form [6]:

$$P = \rho_{i0} u_{0m}^2 \left(1 - \frac{V_i}{V_{i0}}\right) + \Gamma_i \frac{C_i\left(T_i - T_0\right)}{V_i} + \Gamma_e \frac{C_e\left(T_e - T_0\right)}{V_e}. \quad (8)$$

Here V_{i0}, $V_{i,e}$ are the initial and current specific volumes, $V_{i0} = 1/\rho_{i0}$, $V_{i,e} = 1/\rho_{i,e}$, where ρ_{i0}, $\rho_{i,e}$ are the corresponding densities, $\Gamma_{i,e}$ are the Grünheisen coefficients, u_{0m} is the sound speed in a metal particle.

The numerical solution of this system of equations was carried out by constructing a finite-difference approximation using artificial viscosity to stabilize the solution in the presence of pressure jumps [11].

Results of numerical simulations and discussion

Before proceeding to the discussion of the results of numerical simulations, let us establish approximate requirements for the duration of a laser pulse for efficient excitation of acoustic signals in micro- and nanoparticles. To implement isochoric heating, it is necessary that the duration of the laser pulse be less than the acoustic relaxation time t_a of the heated region (less than the time of passage of a sound wave through it). For a spherical particle $t_a = 2R_0 / u_0$. For typical values of the sound speed, this value can be estimated for micron-sized particles as $t_a \approx 10^{-9}$ s, and $t_a \approx 10^{-11}$ s for particles with a radius of 10 nm. Consequently, in the first case, it is advisable to use laser radiation with a pulse duration of the picosecond range, and to excite acoustic vibrations of nanometer particles, it is necessary to use radiation of a subpicosecond (femtosecond) duration.

As the first example, consider the problem of the excitation of acoustic pulses in a spherical microparticle simulating an agglomerate of close-packed carbon nanotubes [12]. We assume the radius of the absorbing particle $R_0 = 1$ μm, the absorption coefficient $k_{abs} = 2.4 \cdot 10^5$ cm^{-1}, the duration of the laser pulse $t_p = 10^{-11}$ s, and the intensity $I_0 = 10^6$ W/cm^2. The rest parameters used in the calculations are the typical values for single-walled carbon nanotubes and water as environment.

As the second example, the problem of the excitation of acoustic vibrations in spherical gold nanoparticles in an aqueous environment is considered. In this case, a two-temperature model of metal heating under the action of an ultrashort laser pulse (equations (6)–(7)) and equation of state (8) were used. The radius of the gold nanoparticle was assumed equal $R_0 = 10$ nm, the absorption coefficient $k_{abs} = 5 \cdot 10^5$ cm^{-1}, the duration of the laser pulse $t_p = 10^{-13}$ s, and the intensity $I_0 = 10^8$ W/cm^2. The calculations were performed for typical thermophysical parameters of gold.

The results of numerical modeling of two problems are presented in Fig. 1 and 2. Let's carry out a comparative analysis. In the first case, the duration of the laser pulse is sufficient, according to the theoretical estimation, for effective excitation of acoustic vibrations of the microparticle (Fig. 1, *a*) and for the formation of a train of acoustic vibrations in the environment surrounding

the particle (Fig. 1, *b*). A train of compression-rarefaction pulses in the environment is formed due to the reflection of a pressure wave at the interface between the absorbing particle/external environment. The period of oscillations (changes in the radius of a spherical particle) in this case is $T \approx 200$ ps.

In the case of a metal (Au) nanoparticle, a change in temperature due to the absorption of the laser pulse energy also initiates the appearance of radial pressure waves ΔP, density $\Delta\rho$, and the velocity of motion of particles of the medium u, propagating at the speed of sound inside the nanoparticle and reflected from its surface and the center of symmetry. In this case, the presence of wave-like motion of particles of the medium can be considered as the emergence of its radial oscillations. For example, Fig. 2 shows the time dependence of the relative radial displacement of the nanoparticle surface. The period of the excited acoustic oscillations is $T \approx 6.2$ ps for the case under consideration, the amplitude of the oscillations is directly proportional to the intensity of the exciting laser pulse. A pressure wave propagating inside a particle upon reflection from the interface between two media on the surface of a nanoparticle initiates pressure fluctuations in the environment. In this case, the first peak in the time dependence of ΔP (r = 10,1 nm) (Fig. 2, *b*) is associated with the heating of the near-surface layer of the liquid at the time of the laser pulse action, while the rest are the result of the partial passage of the compression-rarefaction wave through the gold–water interface.

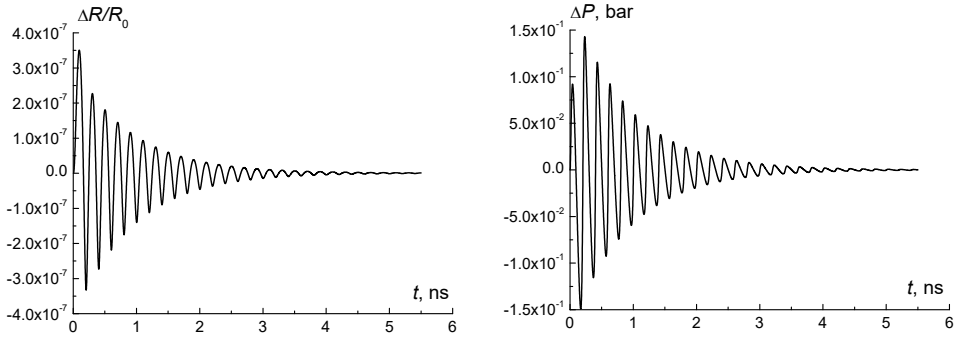

a *b*

Fig. 1. Time dependence of changes in the radius of carbon microparticle (*a*) and pressure in the environment (*b*)

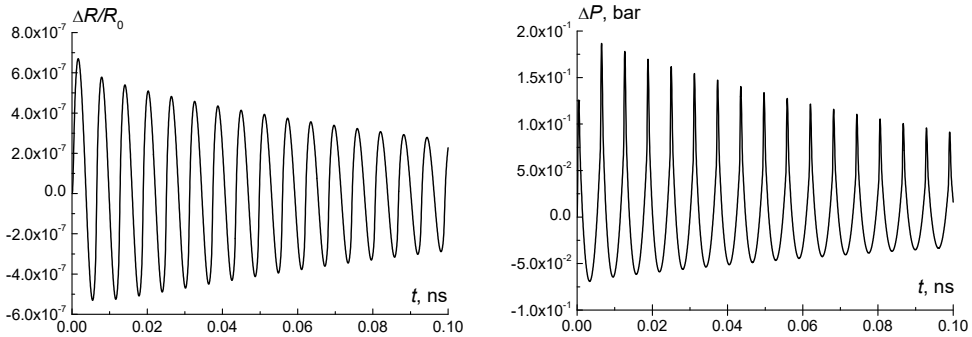

a *b*

Fig. 2. Time dependence of changes in the radius of gold nanoparticle (*a*) and pressure in the environment (*b*)

Conclusion

In conclusion, for the theoretical description of thermomechanical phenomena in absorbing micro- and nanostructures under the action of pulsed laser radiation, a technique has been developed for the numerical simulation of the equations of continuous media motion in the form of the Lagrange equation and the heat conduction equation. It is shown that, when the duration of laser pulses is shorter than the acoustic relaxation time, effective excitation of acoustic vibrations in micro- and nanostructures occurs. Examples of carbon microparticles and gold nanoparticles are considered in details.

References

1. Attia A.B.E., Balasundaram G., Moothanchery M., Dinish U.S., Bi R., Ntziachristos V., Olivo M. A review of clinical photoacoustic imaging: Current and future trends. *Photoacoustic*s. 2019;16:100144. https://doi.org/10.1016/j.pacs.2019.100144
2. Dumitras D.C., Petrus M., Bratu A.M., Popa C. Applications of Near Infrared Photoacoustic Spectroscopy for Analysis of Human Respiration: A Review. *Molecules.* 2020;25(7):1728. http://doi.org/10.3390/molecules25071728.
3. van Capel P.J.S., Peronne E., Dijkhuis J.I. Nonlinear ultrafast acoustics at the nano scale. *Ultrasonics*. 2015;56:36-51. https://doi.org/10.1016/j.ultras.2014.09.021.
4. Smith R.J., Perez Cota F., Marques L., Chen X., Arca A., Webb K., Aylott J., Somekh M.G., Clark M. Optically excited nanoscale ultrasonic transducers. *J. Acoust. Soc. Am.* 2015;137:219-227. https://doi.org/10.1121/1.4904487.
5. Taruttis A., Ntziachristos V. Advances in real-time multispectral optoacoustic imaging and its applications. *Nature Photonics*. 2015;9:219-227. https://doi.org/10.1038/nphoton.2015.29.
6. Romanov O.G., Romanov G.S. Thermomechanical effect of ultrashort laser pulses on single-dimension metallic nanostructures. *Bulletin of the Russian Academy of Sciences: Physics*. 2014;78(12):1299-1302. https://doi.org/10.3103/s1062873814120260.
7. Khokhlov N., Knyazev G., Glavin B., Shtykov Y., Romanov O., Belotelov V. Interaction of surface plasmon polaritons and acoustic waves inside an acoustic cavity. *Optics Letters*. 2017;42(18):3558-3561. https://doi.org/10.1364/OL.42.003558.
8. Richtmayer R.D., Morton K.W. *Difference methods for initial-value problems*. Interscience publishers a division of John Wiley & Sons; 1967.
9. Zel'dovich Ya.B., Raizer Yu.P. *Fizika udarnykh voln i vysokotemperaturnykh gidrodinamicheskikh yavlenii* (*Physics of Shock Waves and High-Temperature Hydrodynamic Phenomena*). Moskow: Nauka; 1966.
10. Anisimov S.I., Imas Ya.A., Romanov G.S., Khodyko Y.V. Deistvie izlucheniya bol'shoi moshchnosti na metally (The Effect of High Power Radiation onto Metals). Moskow: Nauka; 1970.
11. Romanov O.G., Zheltov G.I., Romanov G.S. Numerical modeling of thermomechanical processes in absorption of laser radiation in spatially inhomogeneous media. *Journal of Engineering Physics and Thermophysics*. 2011;84(4):772-780. https://doi.org/10.1007/s10891-011-0533-5.
12. Golubewa L., Timoshchenko I., Romanov O., Karpicz R., Kulahava T., Rutkauskas D., Shuba M., Dementjev A., Svirko Yu., Kuzhir P. Single-walled carbon nanotubes as a photo-thermo-acoustic cancer theranostic agent: theory and proof of the concept experiment. *Scientific Reports*. 2020;10:22174. https://doi.org/10.1038/s41598-020-79238-6.

Authors' contribution

Romanov O.G. developed the theoretical model, prepared the manuscript of the article.

Shtykov Y.K. performed computer simulations of the photoacoustic effect in metal nanostructures.

Timoshchenko I.A. performed computer simulations of the photoacoustic effect in carbon micro- and nanostructures.

All authors took part in the discussion of the results of the work.

Information about the authors

Romanov O.G., PhD., Assosiate Professor, Head of the Department of Computer Simulations of the Faculty of Physics of Belarusian State University.

Shtykov Y.K., Postgraduate student at the Faculty of Physics of Belarusian State University.

Timoshenko I.A. Senior Lecturer at the Faculty of Physics of Belarusian State University.

Address for correspondence

220030, Republic of Belarus,
Minsk, Nezavisimosti Ave., 4,
Belarusian State University;
tel. +375-17-209-51-21;
e-mail: romanov@bsu.by
Romanov Oleg Gennadievich

http://dx.doi.org/10.35596/1729-7648-2021-19-8-63-67

Original paper

UDC 538.91

ATOM SPECIES ENERGY DEPENDENCE ON MAGNETIC CONFIGURATIONS IN THE PEROVSKITE YTTRIUM ORTHOFERRITE

ALEKSEY V. BAGLOV, LIUDMILA S. KHOROSHKO

Belarusian State University of Informatics and Radioelectronics (Minsk, Republic of Belarus)
Belarusian State University (Minsk, Republic of Belarus)

Submitted 22 November 2021

Abstract. The article represents the results of studying of the influence of atom species in the perovskite multiferroic yttrium orthoferrite $YFeO_3$ on magnetic configurations by ab-initio methods. Four magnetic configurations possible in magnetic sublattice that were formed by iron atoms were analyzed. It is shown that different magnetic orderings change the lattice parameters and the ions occupied positions while preserving symmetry of the unit cell, the lowest state responds G-AFM type magnetic ordering. The lattice parameters are in good relevant published experimental data. The atom species energy dependence shows that the main role in magnetic properties goes to iron and oxygen. In the ground state, magnetic properties relate with Dzyaloshinskii – Moriya interaction, while in other configurations, these relate with superexchange through Fe-O-Fe chains. Obtained results are useful for analyzing and designing straintronics devices. Also, the results can be interesting for interpretation and predicting magnetic properties of partially or fully substituted orthoferrites including substitution on rare-earth elements.

Keywords: multiferroic, perovskite, orthoferrite, ab-initio, antiferromagnetic, magnetic ordering.

Conflict of interests. The authors declare no conflict of interests.

Gratitude. The authors are grateful for the partial support of the research by the grant F20MV-022 (BRFFR, Ministry of Education, Republic of Belarus)

For citation. Baglov A.V., Khoroshko L.S. Atom species energy dependence on magnetic configurations in the perovskite yttrium orthoferrite. Doklady BGUIR. 2021; 19(8): 63-67.

Introduction

Multiferroics are materials which combine (ferro)magnetic and ferroelectric ordering. These materials are very interesting both radioelectronic applications and new scientific directions, such as straintronics, which use effects and phenomena created by deformations for new devices creation. Early we described different magnetic orderings in the perovskite $YFeO_3$ and the dependence of the structural properties on them with ab-initio methods were established [1].

The difference in total energy and structural parameters of the various magnetic configurations of the $YFeO_3$ appears due to the interaction of iron d-shell electrons in magnetic sublattice, formed by iron ions, and interaction between iron ions neighboring yttrium, and oxygen ions which change electron density distribution and total energy in the material. Unfortunately, the contribution of each atom species to the total energy in various magnetic configurations of the $YFeO_3$ is unknown.

Dependence of Fe ions d-shell electron energy for these states in the $YFeO_3$ is also unknown. This information can be useful for engineering magnetic properties of a multiferroics with perovskite structure for physical and technical applications. Thereby in this work we study energy contribution for each atom species and changing spin-resolved energy in iron d-shell electrons in the dependence of the $YFeO_3$ magnetic configurations by ab-initio methods. Also, we study the evolution of Fe ions magnetic moments and a state of the d-shell through Mulliken populations analysis.

Methods of calculation

We performed our ab-initio calculations within the density functional theory and pseudopotential theory as implemented in the OpenMX code [2–4]. We chose generalized gradient approximation (GGA) and the Perdew – Burke – Ernzerhof exchange-correlation functional while taking into account of spin polarization [5]. We used pseudopotentials with the following valence state configurations: Y – 4s, 4p, 4d, and 5s states; Fe – 3p, 3d, and 4s states; O – 2s and 2p states. We selected the basis sets with 2 primitive pseudoatomic orbital (PAO) functions for each electronic state and 1 adding primitive PAO function as polarized for better description of chemical bonding. For the numerical integrations and the solution of the Poisson's equation, we chose 60×80×56 real-space grid, which approximately equals the cutoff energy 4200 eV [4].

The integration over Brillouine zone the 4×3×5 regular Γ-centered k-points mesh was performed. Self-consistent field calculation was stopped when the difference between two consecutive iterations is less than 10^{-6} eV/atom. The total and orbitally decomposed energies were obtained for equilibrium lattices for each magnetic configuration after structure relaxation, which stopped, when the forces acting on each atom and each component of stress-tensor became less than 0.01 eV/Å.

Results and discussion

The perovskite multiferroic $YFeO_3$ with orthorhombic primitive Bravais lattice has a centrosymmetric primitive cell that includes 4 formulae units (Fig. 1, *a*). In the process of structural relaxation, it was found that while the lattice parameters and the positions occupied by the ions change, the initial symmetry of the unit cell is preserved. Thus, in this crystal four magnetic orderings are allowed: one ferromagnetic (FM) and three antiferromagnetic (AFM), also called as A-AFM, C-AFM and G-AFM. Although all orderings formed by the Fe magnetic sublattice, they are not equivalent in energy sense, what causes differences lattice parameters and atom positions. Our earlier calculations and the experiments of the other researchers showed that the G-AFM ordering in $YFeO_3$ is the main ordering [1, 6].

Following [1], the total energy of the $YFeO_3$ is monotonously decreasing from ferromagnetic (FM) to antiferromagnetic (AFM) state with close energy distances per formulae unit between neighboring magnetic configurations in set FM → A-AFM → C-AFM → G-AFM (Tab. 1). Differences in a spin configuration in an iron sublattice changes energy for each atomic species in different ways (Fig. 1, *b*). In all cases, the zero energy is a relative value.

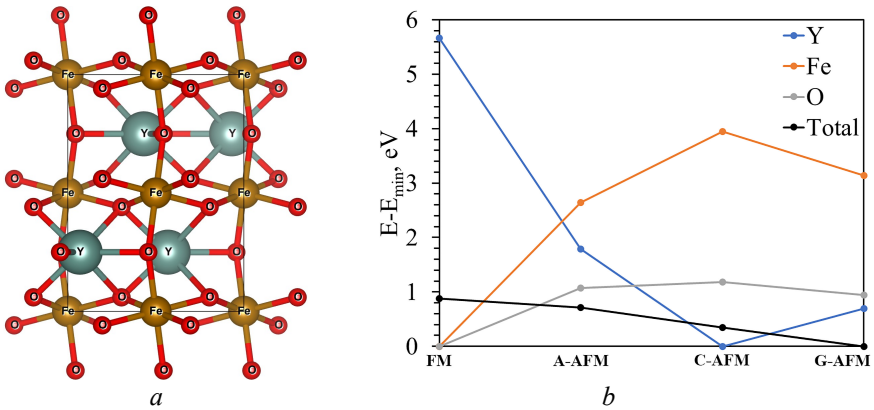

a *b*

Fig. 1. $YFeO_3$ perovskite structure: *a* – primitive cell; *b* – atom species contribution dependence on magnetic configuration

Table 1. Structural properties of $YFeO_3$ with different magnetic ordering

Magnetic ordering	Lattice parameter, Å			Volume, Å^3	ΔE (per formulae unit), meV
FM	5.67438	7.55454	5.27973	226.328	228
A-AFM	5.65376	7.60403	5.30612	228.117	179
C-AFM	5.62010	7.70463	5.30326	229.635	87
G-AFM	5.63788	7.65396	5.30518	228.930	0
Experiment (G-AFM) [7]	5.58770	7.59510	5.27430	223.837	–

Decomposition of the total energy on atom species show that yttrium energy states decreasing in the order FM → A-AFM → C-AFM, with increasing in G-AFM ordering a case. The behavior of iron and oxygen atoms is opposite, and deviation of energy is less than for yttrium. It says about the primary role of the interaction between iron and oxygen atoms on magnetic properties of the $YFeO_3$. For better understanding processes behind the interaction between all atom species in the $YFeO_3$ we appreciated their magnetic moments in different magnetic configurations through Mulliken populations analysis. In this case magnetic moments can be roughly estimated as a difference between populations with up spin and down spin states.

Following symmetry of the crystal all yttrium and iron atoms are equivalent, and oxygen atoms divided in 2 groups of equivalent atoms – 4 atoms in the first group and 8 atoms in the second, which we will designate as O(1) and O(2) respectively. All information is presented in Tab. 2, the zero energy is a relative value. In all cases magnetic moment of yttrium atoms is either small or zero. It says about a weak role of this element in the magnetic properties of the $YFeO_3$.

The magnetic and energetic behavior of iron and oxygen atoms correlated for 3 out of 4 magnetic configurations, but the absolute magnetization of oxygen in the G-AFM phase is either very small or zero. It says about the primary role of antisymmetric exchange, or the so-called Dzyaloshinskii – Moriya interaction (DMI), not the superexchange mechanism as for other magnetic configurations, what is consistent with the experimental data. For FM, A-AFM, and C-AFM the main mechanism of magnetization is superexchange between two next-to-nearest neighbor iron atoms through an oxygen atom.

Table 2. The magnetic moments per atom for each atom species group in the $YFeO_3$ with different magnetic ordering

Atom species group	Magnetic moment, μ_B			
	FM	A-AFM	C-AFM	G-AFM
Y	0.04	0.00	0.01	0.00
Fe	3.39	3.77	3.92	3.90
O(1)	0.11	0.00	0.19	0.00
O(2)	0.13	0.17	0.02	0.02

For better understanding of Fe-Fe and Fe-O interaction energy dependence of iron t_{2g}- and e_g-orbitals as well as Mulliken populations of its d-states from magnetic configurations were studied (Fig. 2, zero energy is a relative value). The lowest energy state of iron d-electrons corresponds to ferromagnetic ordering, but does not for t_{2g}-orbitals spin up states, which has the lowest energy in G-AFM ordering. Opposite behavior of t_{2g}-orbitals, which interacts with oxygen p-orbitals can relate to the angle change in Fe-O-Fe chains and distance between iron and oxygen atoms.

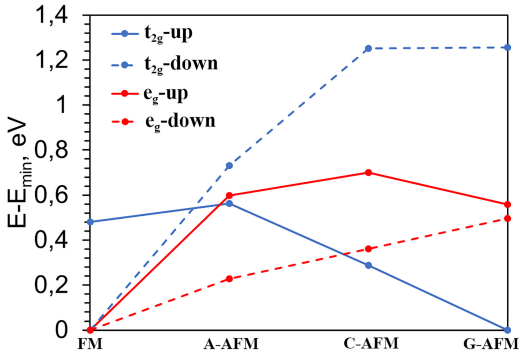

Fig. 2. Spin-resolved energy dependence in different magnetic configurations of $YFeO_3$ Fe t_{2g}- and e_g-orbitals contribution

Conclusion

Thus, in this work we studied the energy contribution dependence for each atom species for various magnetic states in $YFeO_3$ perovskite multiferroic and energy contribution dependence for iron d-shell electrons from the magnetic configuration, by ab-initio methods. It was shown, that the main role in the magnetic properties of configurations, excluding the ground state G-AFM, performs superexchange through Fe-O-Fe chains, which is being replaced by the antisymmetric exchange, or the Dzyaloshinskii – Moriya interaction responsible for the experimentally observed weak magnetism in this material. Changes in magnetic moments of iron atoms are underestimated compared to the experiments, but slightly, about 10 %. Configuration transition to G-AFM showed strong changes in the energetic behavior of t_{2g}-orbitals, related to the rearrangement of crystal lattice and changes in angles of Fe-O-Fe chains and distances between iron and oxygen atoms. The distance between the nearest two magnetic orderings C-AFM – G-AFM is about 90 meV per formulae unit, what allows to save this ordering at room temperatures. It was shown, that density functional theory with localized basis set allows to accurately describe both structural and magnetic properties in perovskite multiferroic $YFeO_3$. A small energetic distance between magnetic configurations and its monotonic changes allows recommend perovskite multiferroics for straintronic memory devices as well as for other applications. We think that describing more complicated materials, such as $NdFeO_3$, $(Y,Nd)(Al,Fe)O_3$ with varying substitution degrees of both yttrium and iron also possible without significant changes in the chosen methods, that is very useful and it inspires to receive new fundamental and practical knowledge in condensed matter physics.

References

1. Khoroshko L., Baglov A. Magnetic configurations in the $YFeO_3$ multiferroic. *Proceedings of VI International conference «Applied Problems of Optics, Informatics, Radiophysics and Condensed Matter Physics»*. Minsk: A. N. Sevchenko Institute of Applied Physical Problems; 2021:251-253.
2. Ozaki T. Variationally optimized atomic orbitals for large-scale electronic structures. *Physical Review B*. 2003;67(15):155108-1–155108-5. DOI: 10.1103/PhysRevB.67.155108.
3. Ozaki T., Kino H. Numerical atomic basis orbitals from H to Kr. *Physical Review B*. 2004;69(19):195113-1–195113-19. DOI: 10.1103/PhysRevB.69.195113.
4. Ozaki T., Kino H. Efficient projector expansion for the ab initio LCAO method. *Physical Review B*. 2004;72:045121-1– 045121-8. DOI: 10.1103/PhysRevB.72.045121.
5. Perdew J.P., Burke K., Ernzerhof M. Generalized Gradient Approximation Made Simple. *Physical Review Letters*. 1996;77:3865-3869. DOI: 10.1103/PhysRevLett.77.3865.
6. Eibschütz M., Shtrikman S., Treves D. Mössbauer Studies of Fe^{57} in Orthoferrites. *Physical Review*. 1967;156:562-577. DOI: 10.1103/PhysRev.156.562.
7. du Boulay D., Maslen E.N., Streltsov V.A., Ishizawa N. A synchrotron X-ray study of the electron density in $YFeO_3$. *Acta Crystallographica: Section B*. 1995;B51:921-929. DOI: 10.1107/S0108768195004010.

Authors' contribution

All authors have equally contributed to the development of the concept and planning provided by research, data acquisition, analysis and interpretation.

Information about the authors

Baglov A.V., Researcher at R&D Lab. 4.4 "Computer-Aided Design of Micro- and Nanoelectronic Systems" of the Belarusian State University of Informatics and Radioelectronics; Senior Lecturer at the Energy Physics Department of Belarusian State University.

Khoroshko L.S., PhD., Associate Professor, Leading Researcher at R&D Lab. 4.4 "Computer-Aided Design of Micro- and Nanoelectronic Systems" of the Belarusian State University of Informatics and Radioelectronics; Associate Professor of Energy Physics Department of Belarusian State University.

Address for correspondence

220013, Republic of Belarus,
Minsk, P. Brovka St., 6,
Belarusian State University
of Informatics and Radioelectronics;
tel. +375-17-293-84-09;
e-mail: L_Khoroshko@bsuir.by
Khoroshko Liudmila Sergeevna

http://dx.doi.org/10.35596/1729-7648-2021-19-8-68-71

Original paper

UDC 621.37

INFLUENCE OF RADIATION EXPOSURE ON THE PROPERTIES OF DIELECTRIC LAYERS BASED ON ANODIC ALUMINUM OXIDE

SERGEY A. BIRAN, DMITRIY A. KOROTKEVICH, ALEXANDER V. KOROTKEVICH, KIRILL V. GARIFOV, ANTON D. DASHKEVICH

Belarusian State University of Informatics and Radioelectronics (Minsk, Republic of Belarus)

Submitted 29 November 2021

Abstract. Devices that are used in the aerospace industry must operate in extreme conditions, so it is important to understand how the properties of materials change under the influence of radiation and low temperatures. Anodic aluminum oxide, due to its mechanical and dielectric properties, is widely used in electronic devices with a high degree of integration. Radiation exposure can lead to degradation of the electrophysical parameters of dielectric films and can also change their chemical composition. The methods for studying the effect of radiation exposure on the dielectric properties of films are shown in this article. The research has been carried out and the results of the influence of α-particles on the dielectric properties of a porous film of anodic aluminum oxide during the influence of low temperature are presented.

Keywords: anodic alumina, radiation exposure, porous film.

Conflict of interests. The authors declare no conflict of interests.

For citation. Biran S.A, Korotkevich D.A., Korotkevich A.V., Garifov K.V., Dashkevich A.D. Influence of radiation exposure on the properties of dielectric layers based on anodic aluminum oxide. Doklady BGUIR. 2021; 19(8): 68-71.

Introduction

Porous anodic alumina is a material with a unique structure. Aluminum oxide film is an ordered structure of hexagonal cells with a pore in the center of the cell. Film parameters such as pore diameter, cell size, oxide film thickness, and structure ordering can be controlled during formation by changing the parameters of the anodizing process [1]. Anodic aluminum oxide films can be used as dielectric bases for integrated circuits, matrices for the synthesis of nanoscale materials, membranes and active elements of sensors. Due to this, alumina is widely used in various fields such as biomedical, nanophotonics, microelectromechanical systems and aerospace industry.

Materials used in the aerospace industry are exposed to various types of radiation. Ionizing radiation, which causes significant changes in the properties of materials, include *x*-rays and γ-radiation, fluxes of electrons, protons, neutrons, as well as the nuclei of atoms of chemical elements. γ-radiation, when passing through a substance, interacts with electrons and atomic nuclei, as a result of which free electrons appear in the substance [2]. The flow of electrons (β-radiation), when exposed to a substance, is able to penetrate to a shallow depth. In this case, electrons lose energy for the excitation and ionization of atoms, for elastic collisions with atoms, for bremsstrahlung radiation, which affects deeper layers of the material. α-particles are nuclei of helium atoms

with a double positive charge. Energy losses during movement in matter are mainly spent on the excitation and ionization of atoms. With a decrease in the energy of α-particles, elastic collisions with the atoms of the substance occur, which leads to the displacement of atoms in the lattice. Devices with a high degree of integration can be sensitive to natural radiation even at the surface of the Earth.

Radiation can affect electronic equipment, degrading performance and resulting in data loss. Degradation of characteristics occurs due to the formation of electron-hole pairs in the gate and insulating dielectrics. Anodic aluminum oxide film shows good resistance to radiation [3] because it captures a significant number of electrons, which compensate for hole traps. In addition, Al_2O_3 has several levels of traps in the band gap, which facilitates easy tunneling of electrons from the dielectric to the substrate [4]. Exposure by medium energy hydrogen and helium ions can lead to the delamination of the anodic alumina film. Oxide delamination is caused by the residual stresses resulting from oxide growth and irregularities in the substrate [5]. The effect of radiation exposure on thin-film structures depends not only on the chemical composition of the films, but also on mechanical stresses at the interfaces [6]. In order to increase the radiation resistance of thin-film structures based on Al_2O_3, it is necessary to improve the technology of forming the interface between layers. To build devices operating in space, it is necessary to know what effect radiation exposure will have on the properties of anodic aluminum oxide films at cryogenic temperatures.

Methods of conducting experiment

Samples for research were made of A0H aluminum with a thickness of 0,9 mm. Substrates with the size of 60×48 mm were cut from a sheet of aluminum. Straightening was carried out to give the substrates flatness. The substrates were heated for an hour at the temperature of 400 °C to remove the internal mechanical stresses arising from the previous stages of processing. The removal of organic contaminants was carried out in a solution of potassium dichromate. The substrates were etched in a NaOH solution for 30 min to remove the upper deformed layer and improve the surface quality. For one-sided anodizing, a photoresist was applied to one of the sides of the substrate.

Anodizing was carried out in a specialized bath with a constant movement of the substrates and maintaining a constant temperature of the electrolyte. An oxalic acid-based solution was used as the electrolyte. Anodizing was carried out in a galvanostatic mode at a current density of 25 mA/cm^2. By varying the anodizing time, films of a given thickness can be obtained. After anodizing, the photoresist layer was removed.

Aluminum film was deposed to the surface of the anodic aluminum oxide to obtain a capacitor structure. The formation of the conducting layer was carried out in an electron-beam deposition unit. By varying the deposition time, it is possible to obtain an aluminum film of the required thickness. Substrates at different stages of manufacturing are shown in Fig. 1.

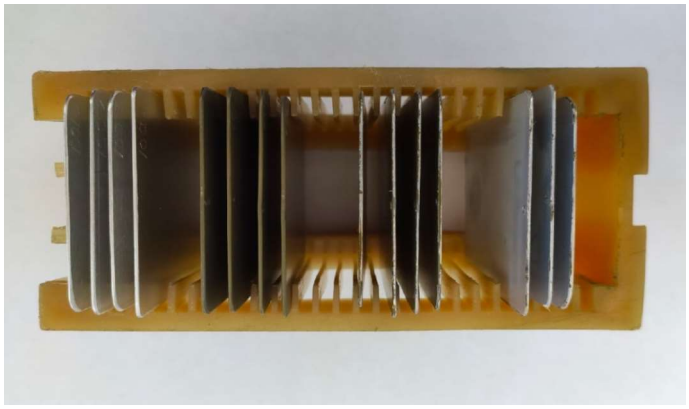

Fig. 1. Substrates at different stages of manufacturing

The samples were irradiated in a special device for studying the radiation properties of materials in a wide range of energies. The samples for the research were loaded into a special container made of a material that quickly looses its activity after irradiation. The container was placed in front of the water moderator. The distance from the water moderator to the sample is selected in

accordance with the required integral fluence of the particles. Particle fluence is controlled by placing activation foils next to the irradiated materials with subsequent measurement of the induced activity. The irradiation time depends on the required particle fluence and varies from several hours to 10 days. The temperature of the samples during irradiation does not exceed 50 °C.

Measurements of the electrical parameters of the capacitor structures in the temperature range from 4,2 to 320 K were carried out in a helium cryostat. For better heat transfer, the samples were attached to the massive copper base of the measuring cell using a thermally conductive adhesive. The change in the temperature regime on the sample during the measurements was carried out using an electric heater of the stove, mounted in the measuring cell. Temperature stabilization on the sample occurred 5 minutes after the change in the power released into the measuring cell. After that, the electrical capacitance of the tested samples was measured. The accuracy of temperature stabilization in the measuring cell was 0,2 K over the entire temperature range. The temperature was measured with a Cu-based thermocouple +0,15 at.%Fe paired with chromel. All contact wires coming from the sample were shielded. The measurement accuracy was no worse than 0,5 %.

Experimental results

The study of the effect of radiation on the dielectric properties of anodic aluminum oxide films was carried out using a capacitor structure in which the aluminum base was used as the lower plate and sprayed contact pad as the upper plate. 1 mm thick aluminum was used as a material for the test structures. Anodizing was carried out in a solution based on oxalic acid with constant stirring of the electrolyte in a galvanostatic mode. The electrolyte temperature was maintained at 15 °C. The thickness of the obtained anodic oxide films of aluminum was 60 μm. 1 μm thick aluminum film was deposited on the surface of the anodic aluminum oxide. Electric capacitance of the samples was measured using an R, L, C meter at a frequency of 1 MHz. The temperature dependence of alumina substrates was studied in a helium cryostat in the range from 4 to 300 K. After measuring the temperature dependence of the electrical capacitance of unirradiated samples, they were irradiated with α-particles with energy 5 MeV from source ^{239}Pu with $3{,}1 \cdot 10^{14}$ sm^{-2} dose. The measurement was repeated after irradiation. Temperature dependence electrical capacity of samples before and after irradiation is presented in Fig. 2.

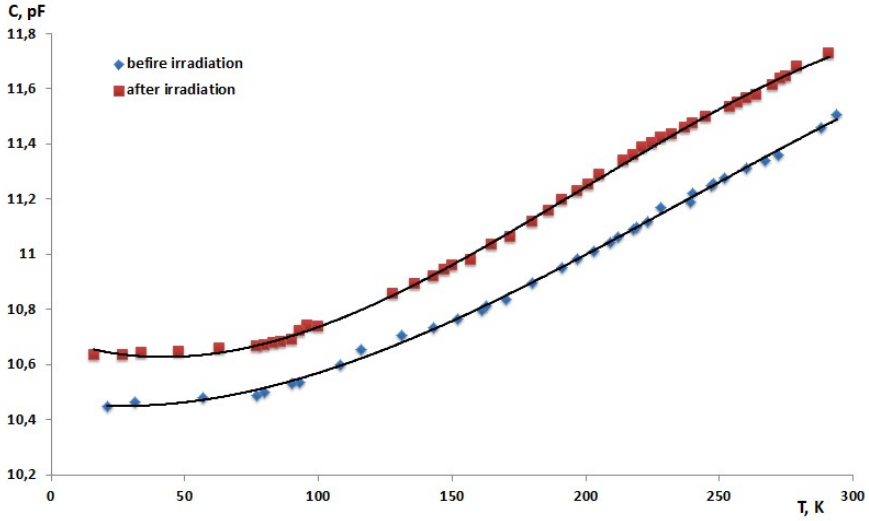

Fig. 2. Temperature dependence electrical capacity of samples before and after irradiation with α-particles

Conclusion

Temperature dependence of the electrical capacitance for unirradiated and irradiated samples has the same form in the entire temperature range. This indicates the absence of any significant changes in the internal structure of the investigated dielectric layers. Quantitative differences in the capacity of unirradiated and irradiated samples are 2 %, the formation of radiation defects

in a dielectric leads to a decrease in its dielectric constant. Taking into account the high ionizing ability of α-particles and their high energy, it can be concluded that capacitor structures are resistant to this radiation effect.

References

1. Lee W., Park S.-J. Porous Anodic Aluminum Oxide: Anodization and Templated Synthesis of Functional Nanostructures. *Chem. Rev.* 2014;(114):7487-7556. DOI: 10.1021/cr500002z.
2. Sidorov N., Knyazeva V. Radiation resistance of materials of radio engineering structures. Moskow: Soviet Radio; 1976.
3. Felix J., Schwank J., Fleetwood D. Effects of radiation and charge trapping on the reliability of high-k gate dielectrics. *Microelectronics Reliability.* 2004;44:563-575.
4. Harari E., Royce B.S.H. Trap structure of pyrolytic Al_2O_3 in MOS capacitors. *Appl. Phys. Lett.* 1973;22:106-107
5. Li M., Xie DG., Ma E. Effect of hydrogen on the integrity of aluminium–oxide interface at elevated temperatures. *Nat Commun.* 2017;8:14564. DOI:10.1038/ncomms14564.
6. Vavilov V., Gorin B., Danilin N. Radiation methods in solid-state electronics. *Radio and communication.* 1990.

Authors' contribution

Biran S.A. developed an experimental technique, analyzed obtained data.
Korotkevich D.A. processed the obtained experimental data, prepared the manuscript of the article.
Korotkevich A.V. performed the task for the study, prepared the manuscript of the article.
Garifov K.V. conducted the research and obtained experimental data.
Dashkevich A.D. made samples for the research.

Information about the authors

Biran S.A., Deputy Dean of the Faculty of Radioengineering and Electronics of the Belarusian State University of Informatics and Radioelectronics.

Korotkevich D.A., Assistant at the Department of Electronics of the Belarusian State University of Informatics and Radioelectronics.

Korotkevich A.V., PhD., Associate Professor, Dean of the Faculty of Radioengineering and Electronics of the Belarusian State University of Informatics and Radioelectronics.

Garifov K.V., Undergraduate at the Department of Micro- and Nanoelectronics of the Belarusian State University of Informatics and Radioelectronics.

Dashkevich A.D., Undergraduate at the Department of Micro- and Nanoelectronics of the Belarusian State University of Informatics and Radioelectronics.

Address for correspondence

220013, Republic of Belarus,
Minsk, P. Brovka St., 6,
Belarusian State University
of Informatics and Radioelectronics;
tel. +372-17-293-89-96;
e-mail: biran@bsuir.by
Biran Sergey Andreevich

http://dx.doi.org/10.35596/1729-7648-2021-19-8-72-80

Original paper

UDC 004.8

SOFTWARE TOOL FOR EVALUATION OF RELIABILITY AND SURVIVABILITY OF COMPLEX TECHNICAL SYSTEM BASED ON LOGICAL-PROBABILISTIC METHODOLOGY

VADIM YU. SKOBTSOV[1], NATALIA V. LAPITSKAYA[2]

[1]*United Institute of Informatics Problems, National Academy of Sciences of Belarus (Minsk, Republic of Belarus)*

[2]*Belarusian State University of Informatics and Radioelectronics (Minsk, Republic of Belarus)*

Submitted 29 November 2021

Abstract. The paper presents solutions for estimation and analysis of complex system (CS) reliability and survivability indicators based on the logical-probabilistic approach. Modified logical-probabilistic method and software tool for evaluating the reliability and survivability of onboard equipment (OE) of small satellites were developed (SS). The correctness of the suggested method and software tool was shown by computational experiments on some systems of CS SS similar to Belarusian SS, and later compared with the "Arbitr" software complex results.

Keywords: logical-probabilistic method, reliability, survivability, onboard equipment for small satellites, diagram of functional integrity, system operability function.

Conflict of interests. The authors declare no conflict of interests.

Gratitude. The research described in subsection 2 of the paper is supported by project No. 17-11-01254 of Russian Science Foundation, the research described in subsection 3 of the paper is supported by the state research0073–2018–0003. All research results represented in the paper were supported by Program STC of Union State "Monitoring-SG" (project 6МСГ/13-224-2, the Belarusian side).

For citation. Skobtsov V.Yu., Lapitskaya N.V. Software tool for evaluation of reliability and survivability of complex technical system based on logical-probabilistic methodology. Doklady BGUIR. 2021; 19(8): 72-80.

Introduction

The evaluation of reliability and survivability of the complex technical systems, like OE for SS, is an important task of their safe and reliable design and operation.

Logic-probabilistic modeling is a method for analyzing the sensitivity of a complex system operating under conditions of uncertainty. The method boasts clarity and a wide range of possibilities to detect the influence of any argument on the reliability and survivability of the entire system.

In this paper the automated logical-probabilistic methodology and software tool for evaluating CS reliability and survivability is suggested. The logical-probabilistic software tool was combined with the CS SS telemetry data analysis software tool and some other methodologies and tools in the complex of methodologies and software tools for evaluating the reliability and survivability

of the CS SS. The complex was integrated into the software complex for multi-objective assessment, analysis, and prediction of values of reliability and survivability for CS SS developed in SPIIRAS.

The logical-probabilistic methodology

The usage of logical-probabilistic approach in evaluating the reliability and survivability of a structurally complex system provides sequential construction of two computational model types [1, 2]:

– boolean function of the system operability:

$$Y_F = Y_F(\{\widetilde{x}_i\}, i = 1,2,..., H). \quad (1)$$

– polynomial of the estimated probability function:

$$P_F = P_F(\{p_i, q_i\}, i = 1,2,..., H). \quad (2)$$

Logical function of the system operability

In logic-probabilistic methodology a Boolean function as a logical model of system reliability and survivability is applied. It is called a logical function of the system operability that represents a set of states in which the system implements an appropriate criterion of its functioning (system health state). A logical criterion can be determined by different properties of the system.

The initial data for determining a logical FSO are:

– diagram of functional integrity (DFI),

– logical criteria of functioning (LCF) of system.

The features and restrictions of CS SS design allow to apply one of the simplest methods of direct analytic substitution for FSO construction.

It provides a consistent replacement in the logical FSO of all integrative functions by their equations selected from the system. Such substitution is performed until there are no undeclared functions y_i in the resulting expression. In other words, all integrative functions y_i will be replaced by simple logical variables x_i.

Computational probability model of system reliability

Polynomial of the estimated probability function (PF) P_F (2) is used as a computational probabilistic model of system reliability. The polynomial should clearly define (within limitations and assumptions) the probability of failure-free system operation, as well as all health states represented using the logical FSO Y_F (1).

In terms of physical meaning, P_F determines the probability of implementing the given logical criterion Y_F of system functioning. A polynomial P_F is a rule for aggregation of particular parameters of system elements, i.e. compositions of elementary probabilities p_i in a system probability characteristic. P_F defines an algorithm for calculating the probability of a complex event Y_F consisting of products, sums, and inversions of its simple random events, whose own probabilistic parameters p_i are known [1–3].

The parameters $p_i, q_i = 1 - p_i$ of the P_F polynomial are intrinsic probabilities of failure-free operation or availability coefficients of system elements.

As for P_F determining, the combined method is applied, one of the most effective and simplest approaches [1]. In general, two successive transformations of the original FSO are performed for accurate determination of P_F using a combined method:

– quasiorthogonalization of the FSO by a single logical variable;

– a symbolic transition to the P_F polynomial.

The conjunctions of a logical function are called orthogonal if their logical product is zero. Therefore, the events representing these conjunctions are inconsistent, and the probability of their sum equals a simple sum of their own probabilities of each event.

Assuming the independence in the aggregate of all elementary binary events $\tilde{x}_i, i = 1,2,...,H$, the algorithm for performing these two steps is as follows.

Quasiorthogonalization by a single logical variable. All pairs of non-orthogonal conjunctions of the original FSO are checked for a possibility of their orthogonalization by the following rule

$$\gamma \times \tilde{x}_i \vee \gamma \cdot \varphi = \gamma \cdot x_i \vee \gamma \cdot \varphi \cdot \overline{\tilde{x}_i}, \tag{3}$$

where γ and φ are parts of the tested conjunctions, in which there is no variable $\tilde{x}_i$. Orthogonalization does not increase the total number of conjunctions in the original FSO. Having performed these transformations with the example illustrated over the function (3), we obtained

$$\begin{aligned} Y_p &= y_3 \cdot y_4 = x_3 \cdot x_4 \cdot x_1 \cdot x_2 \vee x_3 \cdot x_4 \cdot x_1 \cdot x_5 \vee x_3 \cdot x_4 \cdot x_2 \cdot x_5 = \\ &= x_3 \cdot x_4 \cdot x_1 \cdot x_2 \vee x_3 \cdot x_4 \cdot x_1 \cdot x_5 \cdot \overline{x}_2 \vee x_3 \cdot x_4 \cdot x_2 \cdot x_5 \cdot \overline{x}_1. \end{aligned} \tag{4}$$

The resulting function is completely orthogonal, so all its conjunctions represent incompatible events.

A symbolic transition to P_F polynomial. A logical FSO is a rigorous analytical form of describing a complex random event in which:

- a conjunction is a product of random events;
- a disjunction is their sum;
- an inversion is the opposite outcome of an event whose probability is to be determined with the help of the desired P_F.

In order to obtain the P_F polynomial from the FSO, it is enough to perform some transformations to labeling of logical variables and operations in the labeling of probability variables and arithmetic operations. These symbolic transformations must be carried out in a strict accordance with the laws of probability theory for calculating the probabilities of products, sums, and additions of random events.

Operability (FSO), a logical function.

Having applied these rules to the orthogonalized FSO (4), we obtained the polynomial of the required P_F:

$$P_p = p_F(y_3 \cdot y_4) = p_3 p_4 p_1 p_2 + p_3 p_4 p_1 p_5 q_2 + p_3 p_4 p_2 p_5 q_1. \tag{5}$$

Survivability model

Survivability [2] is an ability of a system to keep operating capacity at random damages of its elements owing to random emergence of the striking factors (blows, explosions, fires, etc.) In order to account for a random damaging factor in the structural model of the system survivability, another new event x_5 is added to the developed DFI: the emergence of the damaging factor (Fig. 1). The occurrence of this event is a prerequisite for a subsequent impact and accidental destruction of system elements 3 and/or 4. If a damaging factor does not arise, elements 3 and 4 are not significantly affected.

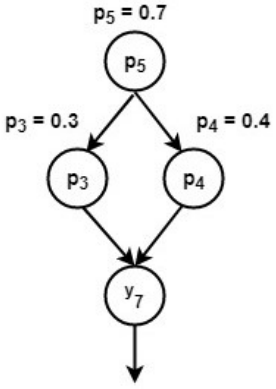

Fig. 1. The damaging factor for a two-element system

There is an operability persistence equation at the output of the fictitious vertex 7:

$$y_7 = \overline{y_3} \vee \overline{y_4}. \quad (6)$$

Operability persistence is sustained by at least one element, which is the criterion Y – the survivability of the system for accidental occurrence and impact of the damaging factor. If the onset of the damaging factor occurs with a probability of $p_5 = 0.7$, $p_3 = 0.3$, $p_4 = 0.4$, a polynomial of survivability probability function is as follows:

$$P_s = q_4 + p_4 q_5 + p_4 p_5 q_3 = 0.916. \quad (7)$$

It should be noted that the DFI of the total survivability of the considered two-element system (see Fig. 1) is nonmonotonic in construction. In particular, it means that an analogous structural model of total survivability cannot be constructed using standard block patterns or typical failure trees. At the same time, the obtained logical and probabilistic survivability functions are still monotonous, within the limits of the accepted substantive definitions for the used elementary events.

Method and software tool for estimating reliability and survivability

Method for calculating reliability and survivability

The software implementation of the considered methodology used for determining the logical FSO and P_F polynomials for the analysis of real structurally complex systems of CS SS with a large number of elements is difficult because of the complexity of automatic analytical simulation processes.

Therefore, we made a modification to the DFI graph while comparing with classical representation of DFI [1, 2]: in addition to the linking arcs and functional vertices, the logical vertices “AND” and “OR” were introduced instead of according arcs (Fig. 2).

Firstly, it helps to see more clearly which systems are redundant and which are not.

Secondly, logical vertices can be used more effectively in algorithms for automatic calculation of the probability of a failure-free operation and survivability of systems. In this case, the FSO Y_F and probability function P_F polynomials are computed implicitly for computing complexity reduction.

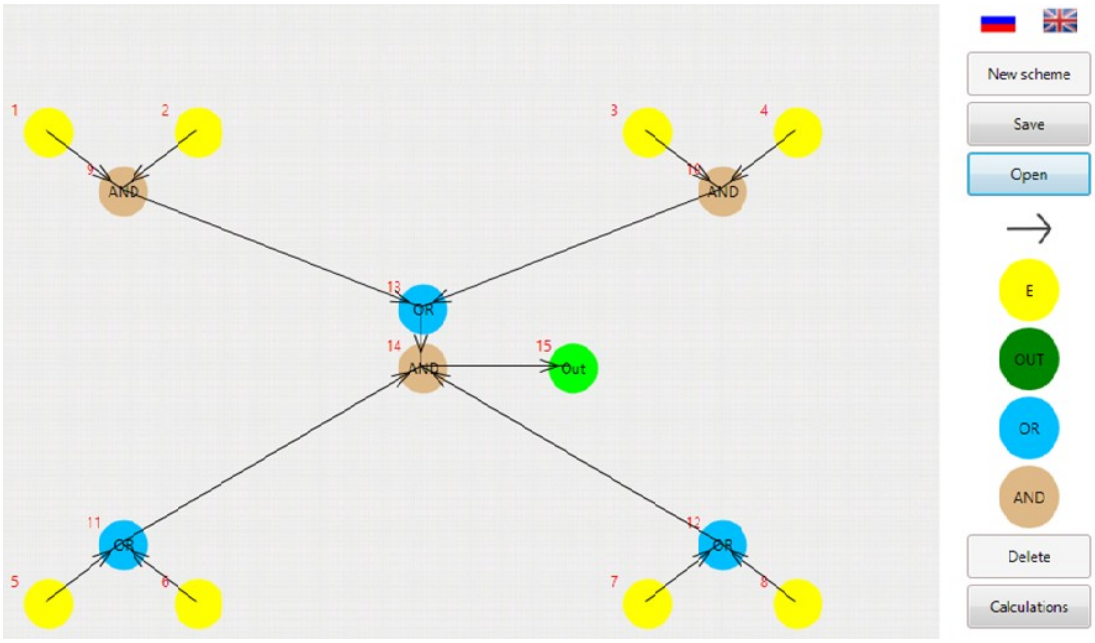

Fig. 2. Example of oriented graph as DFI of the multispectral camera subsystem (MCS) of the Belarussian SS, DFI graphical input window, desktop-version

Thirdly, there are systems consisting of *X* vertices that remain operative when any of the *Y* vertices work. For example, the flywheel group of satellite orientation system very often consists of 4 flywheels and in order to operate correctly, the presence of any three operable flywheels out of 4 is required. It is possible to create and analyze such systems using logical vertices.

The graph will be designed in such way that the functional elements commute with each other only through logical elements.

Introduction of these vertices does not change the probability of failure-free operation and the reliability and survivability of the systems at all. As a rule, the scheme is created on the basis of four logical constructions (Fig. 3). In order to create more complex structures, logical elements can be commuted with each other in any quantity. The width and depth search algorithms are used for graph navigation.

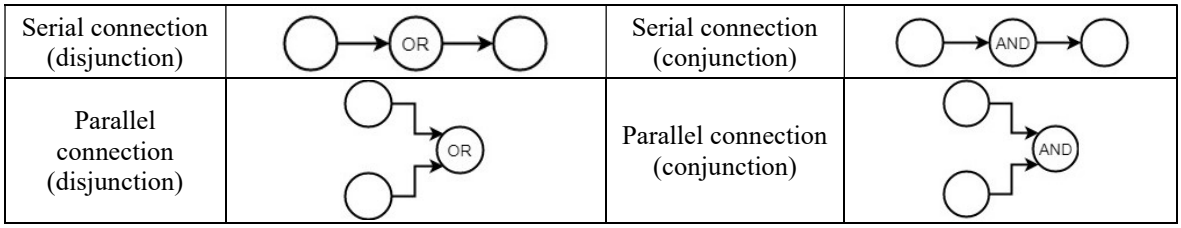

Fig. 3. Basic types of logical constructions

At each stage for each structural node, the probabilities of a failure-free operation and survivability are recalculated and transferred to the next vertex. Thus, each vertex contains information about the calculations on all previous vertices. And whenever we get to any vertex, we can always get the probabilities obtained for the previous vertices. Algorithm operation is finished when all final vertices are reached [4] (Fig. 4).

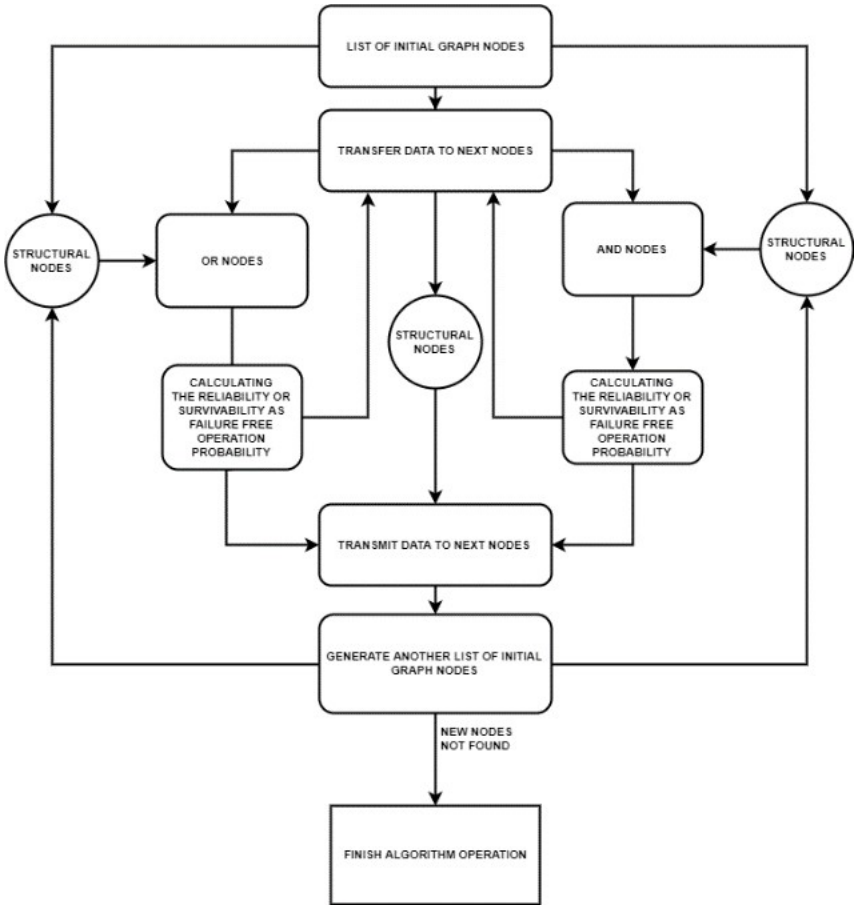

Fig. 4. The algorithm for calculating the probability of a failure-free operation and survivability

Software tool of logical-probabilistic estimating the reliability and survivability of system operating

Correspondent software tool, based on the logical-probabilistic approach and the proposed algorithm, was developed in two versions: a desktop version and a web one. The software tool was designed to automate the process of evaluating the reliability and survivability of CS SS systems. The tool implements the following functions:

– graphical input and editing DFI representing a device under analysis (Fig. 2, 6);

– input and editing the system element parameters including failure-free operation probabilities p_i and a redundancy level of the system elements;

– calculating the single value of the system reliability for the given single arguments of failure a free operation probability p_i for structural nodes;

– reliability analysis – calculating the values of the CS SS systems reliability for the series of element probability arguments and drawing graphics (Fig. 6, 7), in this case element probability parameters p_i are equally changed in the range ($p_{ini} > 0$; $p_{fin} \le 1$) by step Δp. During the reliability analysis, failure free operation probabilities p_i of some elements could be fixed to the value in their properties by setting on according checkboxes in the elements list (Fig. 6, 7);

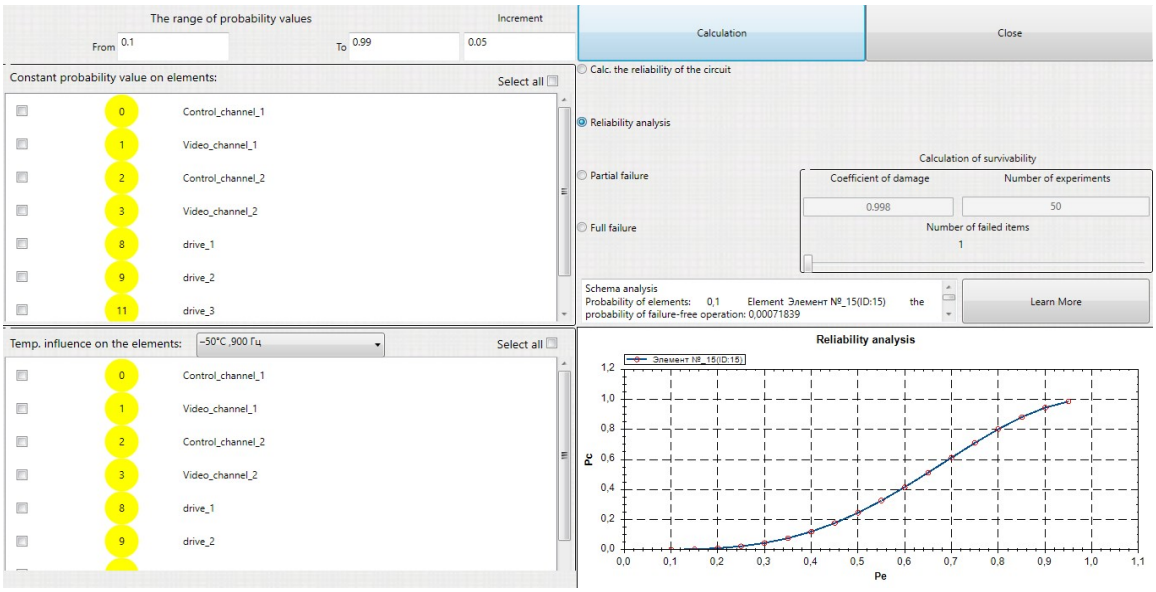

Fig. 5. Window for calculating, reliability analysis, desktop-version

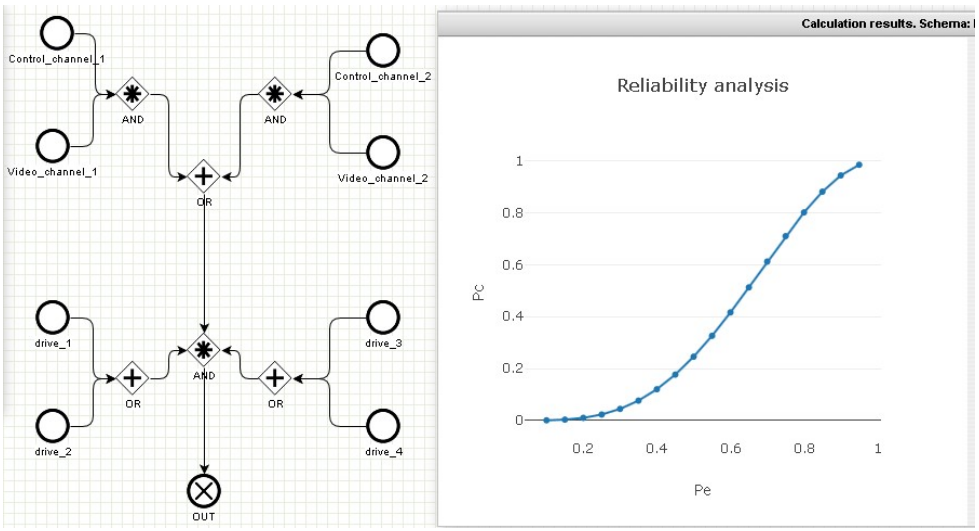

Fig. 6. Web-interface, example of graphical input and editing the DFI of the multispectral camera subsystem (MCS) of the Belarussian SS, reliability analysis results

– Survivability analysis – calculating the survivability of CS SS systems with full and partial failure and drawing a graphic. The damaging factor is applied to randomly selected k elements which reduces the probability of a failure-free operation p_i of these elements to 0 in case of full failure and in case of partial failure to $\tilde{p}_i < p_i$ that can CS set throw interface (Fig. 5, 6). The experiment is repeated N (50 by default) times (Fig. 7, 8). During survivability analysis some elements can be excluded from the impact of damaging factors by setting corresponding checkboxes in the elements list.

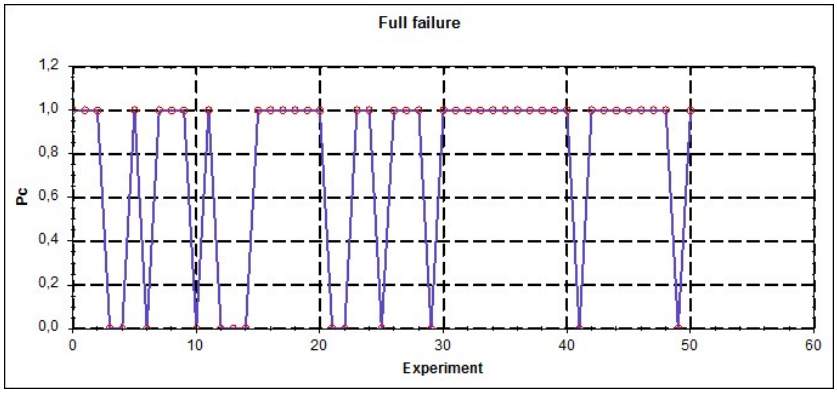

Fig. 7. Determining the survivability of the MCS under full failure

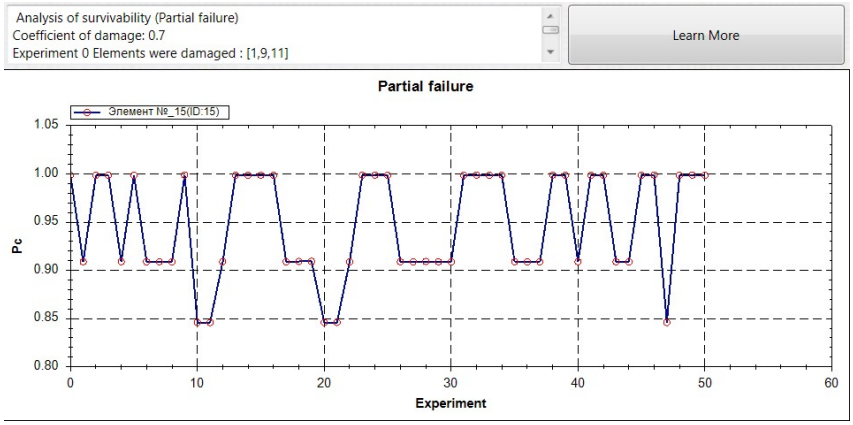

Fig. 8. Determining the survivability of the MCS under partial failure

Moreover, during the analysis of reliability and survivability of CS SS systems, the impact of thermal and mechanical factors on some system elements could be taken into account. It can be achieved through setting corresponding checkboxes in the elements list.

Computational experiments

The correctness of the developed methodology and software tool was tested on some test systems of CS for Belarusian SS, later compared with the "Arbitr" software complex results [1, 2], certified in 2007 by Rostechnadzor (RF) for industrial application. In Tab. 1–3 the comparison results for MCS – the component of OE for Belarusian SS (Fig. 2) are represented. In Tab. 4 the reliability analysis comparison of the results for other three systems of OE SS similar to Belarusian SS are represented.

Table 1. Comparison results for MCS – component of OE of Belarusian SS. Single reliability index value

Reliability Calculating	Developed tool: Pc = 0.99940407919804	Software complex "Arbitr": Pc = 0.999404079

Table 2. Comparison results for MCS – component of OE of Belarusian SS. Reliability analysis

Elements probability p_i	Pc, Developed tool	Pc, Software complex "Arbitr"	Term and mechanical influence on the elements:	Constant reliability on the elements:	Pc, Developed tool	Pc, Software complex "Arbitr"
0.1	0.0007183	0.000718	–	–	–	–
0.3	0.0447111	0.044711	–	–	–	–
0.6	0.4165862	0.416586	–	–	–	–
0.8	–	–	3,6,7	1.8	0.88408152961	0.88408153
0.9	–	–	1	1	0.958474759968	0.95847476
1	–	–	1,2,3,4,5,6,7,8	2	0.999461280139	0.99946128

Table 3. Comparison results for MCS – component of OE for Belarusian SS. Survivability analysis. The damaging factor 0,998, failure of 3 elements

The following elements are failure ed:	Pc, Develop ed tool	Pc, Software complex "Arbitr"	Temperature influence on the elements:	Constant reliability on the elements:	Pc, Developed tool	Pc, Software complex "Arbitr"
7,2,4	0	1,9404E-50	–	–	–	–
8,2,1	0.97020197	0.97020197	–	–	–	–
8,6,1	0.96059601	0.96059601	–	–	–	–
8,5,6	–	–	1,3	2.4	0	1.95869E-50
6,7,3	–	–	1,3	24	0.95291124192	0.952911242

Table 4. Comparison results for systems of OE SS similar to Belarusian SS. Reliability analysis

Elements probability p_i	Navigation system equipment		Multispectral camera system		Orientation and stabilization system	
	Pc, Developed tool	Pc, Software complex "Arbitr"	Pc, Developed tool	Pc, Software complex "Arbitr"	Pc, Developed tool	Pc, Software complex "Arbitr"
0.60	0.027546	0.027546	0.064524	0.064524	0.090334	0.090334
0.70	0.087048	0.087048	0.164648	0.164648	0.214043	0.214043
0.80	0.228170	0.228170	0.347892	0.347892	0.417471	0.417471
0.90	0.512256	0.512256	0.630247	0.630247	0.693272	0.693272

Represented computational experiments show equality of the results for the developed methodology and software tool with the results of the software complex "Arbitr" and hence the correctness of the suggested method and developed tool.

Conclusion

In the paper an effective logic-probabilistic methodology and approach to estimating reliability of complex systems was considered. The methodology was applied to the problem of estimating the reliability and survivability of on-board equipment for small satellite systems. A modified logical-probabilistic method and a software tool for evaluating the reliability and survivability of OE SS systems were developed. The developed software tool automatizes the reliability and survivability estimating process. It also enables graphical input of DFI data and survivability analysis through drawing the graphics of obtained results. The correctness of the suggested method and software tool was shown by computational experiments on some systems of OE SS similar to Belarusian SS, later compared with the "Arbitr" software complex results. The logical-probabilistic software tool was combined with the OE SS telemetry data analysis software tool, represented in CSOC'2017 proceedings [3], and some other methodologies and tools in the complex of methodologies and software tools for evaluating the reliability and survivability of the OE SS.

References

1. Mozhaev A.S. The technology of automated structural and logical modeling of reliability, survivability, safety, efficiency and risk of functioning the systems. *Instruments and Systems: Monitoring, Control, and Diagnostics*. 2008 9:1-14.
2. Mozhaev A.S. and Grommov V.N. *Theoretical foundations of the general logical-probabilistic method of automated systems modeling*. St. Petersburg: VITU; 2000.
3. Skobtsov V., Novoselova N., Arhipov V., Potryasaev S. Intelligent telemetry data analysis of small satellites. Cybernetics and Mathematics Applications in Intelligent Systems. CSOC 2017. *Advances in Intelligent Systems and Computing*. Springer International Publishing Switzerland. 2017;574:351-361.
4. Cormen T.H., Leiserson C.E., Rivest R.L., Stein C. *Introduction to Algorithms.* 3rd edition. The MIT Press; 2009.

Authors' contribution

Skobtsov V.Yu. performed a full cycle of work, including problem statement, research and development of a modified logical-probabilistic method for analyzing the reliability and survivability of complex systems, work related to the software implementation of the method, and project management.

Lapitskaya N.V. took part in the problem statement and graphic-analytical investigation method to determine the logical FSO.

Information about the authors

Skobtsov V.Yu., PhD., Associate Professor, Leading Researcher at the United Institute of Informatics Problems of the National Academy of Sciences of Belarus.

Lapitskaya N.V., PhD., Associate Professor, Head of POIT Department of the Belarusian State University of Informatics and Radioelectronics.

Address for correspondence

220012, Republic of Belarus,
Minsk, Surganova St., 6,
United Institute of Informatics Problems
of the National Academy of Sciences of Belarus;
tel. +375-29-912-62-05;
e-mail: vasko_vasko@mail.ru
Skobtsov Vadim Yurievich

http://dx.doi.org/10.35596/1729-7648-2021-19-8-81-86

Original paper

UDC 621.382

THE PROTON FLUX INFLUENCE ON ELECTRICAL CHARACTERISTICS OF A DUAL-CHANNEL HEMT BASED ON GAAS

IVAN YU. LOVSHENKO[1], ALEKSEI YU. VORONOV[1], POLINA S. ROSHCHENKO[1], ROMAN E. TERNOV[1], YAROSLAV D. GALKIN[2], ALEXEY V. KUNTS[2], VICTOR R. STEMPITSKY[1], JINSHUN BI[3]

[1]*Belarusian State University of Informatics and Radioelectronics (Minsk, Republic of Belarus)*

[2]*Research Institute for Nuclear Problems of Belarusian State University (Minsk, Republic of Belarus)*

[3]*Institute of Microelectronics of Chinese Academy of Sciences (Beijing, People's Republic of China)*

Submitted 8 December 2021

Abstract. The results of the simulation the influence of the proton flux on the electrical characteristics of the device structure of dual-channel high electron mobility field effect transistor based on GaAs are presented. The dependences of the drain current I_D and cut-off voltage on the fluence value and proton energy, as well as on the ambient temperature are shown.

Keywords: HEMT, GaAs, proton fluence, displacement effects, nonionizing energy loss, simulation.

Conflict of interests. The authors declare no conflict of interests.

Gratitude. The research is funded by and carried out within the state program of scientific research “Photonics and electronics for innovations” (task 3.4).

For citation. Lovshenko I.Yu, Voronov A.Yu., Roshchenko P.S., Ternov R.E., Galkin Ya.D., Kunts A.V., Stempitsky V.R., Jinshun Bi. The proton flux influence on electrical characteristics of a dual-channel hemt based on GaAs. Doklady BGUIR. 2021; 19(8): 81-86.

Introduction

The Element base of modern objects of space and nuclear technology is exposed to ionizing radiations, the primary of which are gamma rays (γ), neutron (n), electron (e), and proton (p) radiations. Alfa-particles (α), fission fragments F_p, and other particles from a nuclear reactor or nuclear explosion zone can also influence the degradation of performance characteristics. However, their influence is not so significant (for example, neutrinos, mesons, etc.) [1].

When a particle flux affects a microelectronic device structure, two main mechanisms are possible: ionization and damages caused as a result of elastic scattering of primary particles and fragments formed in nuclear reactions (inelastic scattering) of incident protons or neutrons on target's nucleuses. Ionization is not considered in this work. Neutrons, protons, alpha particles, heavy ions, and photons with very high energies cause displacement effects: the arrangement of atoms in the crystal lattice changes and the number of recombination centers (defects) increases, decreasing the concentration of free charge carriers and deteriorating the performance of device structures.

The parameters of the bulk material most sensitive to the effects of displacements are the lifetime and diffusion length of minority charge carriers, the mobility and concentration of charge carriers [2].

The magnitude of the manifestation of displacement effects depends on the type of particle radiation, the total dose, radiation flux and energy, ambient temperature, operating voltage, as well as the state of the device at the moment of irradiation. These problems complicate testing, increase the complexity of using theoretical calculations to predict radiation effects, increase the time of designing device structures and require a significant number of test samples. In modern computer-aided design systems in microelectronics like Silvaco [3] and Synopsys [4], the modules for accounting for displacement effects are implemented, which require adjustment and calibration.

Thus, the paper represents the results of evaluating the processes of degradation of the electrical characteristics of device structures dual-channel high electron mobility field effect transistor (HEMT) based on GaAs under the influence of the proton flux by means of a computer simulation.

Dual-channel GaAs-HEMT device structure and experimental technique

A typical device structure of a dual-channel GaAs-HEMT is shown in Fig. 1. The cut-off voltage and drain current for the resulting structure at ambient temperature $T = 303$ K are equal to $V_{TH} = -0.9$ V and $I_D = 0.48$ mA (at drain voltage $V_D = 1$ V and gate $V_G = 0$ V), respectively.

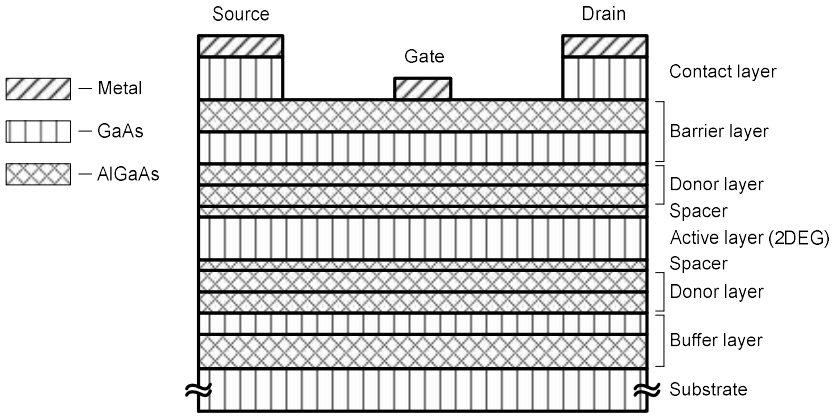

Fig. 1. Device structure of a dual-channel GaAs-HEMT

Fig 2. shows an energy diagram of the region under the gate for a device structure of a dual-channel GaAs-HEMT.

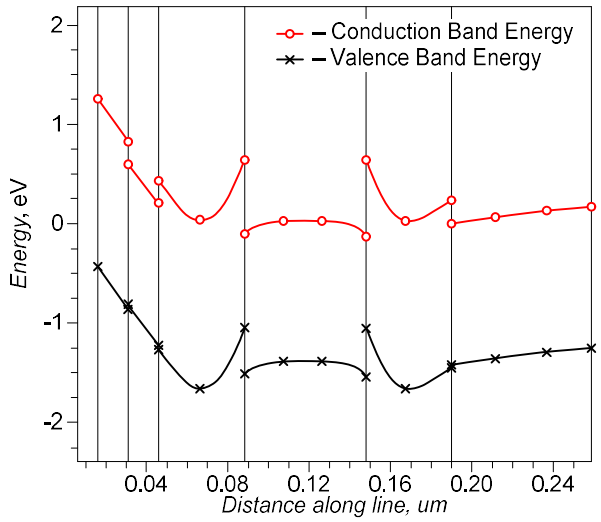

Fig. 2. Energy diagram of the region under the gate for a device structure of a dual-channel GaAs-HEMT

To predict the degradation of device parameters caused by penetrating radiation, it is often sufficient to consider only the first stage of the defect formation process. The formation of bulk defects in a semiconductor device structure is proportional to a *non-ionizing energy loss* (*NIEL*) – the total kinetic energy transferred to the lattice atoms. In modeling and calculations, in addition to the *NIEL* parameter [MeV·cm^2/g], the term kinetic energy released in matter *Kinetic Energy Released in Material* (*KERMA*) is also used. The relationship between *KERMA* and *NIEL* can be written as

$$KERMA = NIEL \cdot F \cdot m, \quad (1)$$

where F – integral radiation flux (fluence), cm^{-2}; m – mass of irradiated material, g.

Parameter *NIEL* can be used to the extrapolation of a device parameter degradation measured for a particle with the given energy to other energies ("NIEL scaling"). The Radiation Fluence Model is used in the microelectronics TCAD software packages to describe the impact of particle flux on material characteristics, which makes it possible to predict the rate of defect generation. According to the model the total density of defect states depends on the radiation flux, *NIEL*, damage coefficient, and the density of material.

The non-ionizing energy losses for GaAs are determined using the SR-NIEL[5] project for displacement threshold energy values E_{d1} = 9,5 eV [6], E_{d2} = 10 eV [7], E_{d3} = 21 eV [8], and E_{d4} = 25 eV [9]. For the obtained values, mean values were determined, which are described by approximating dependence (Fig. 3).

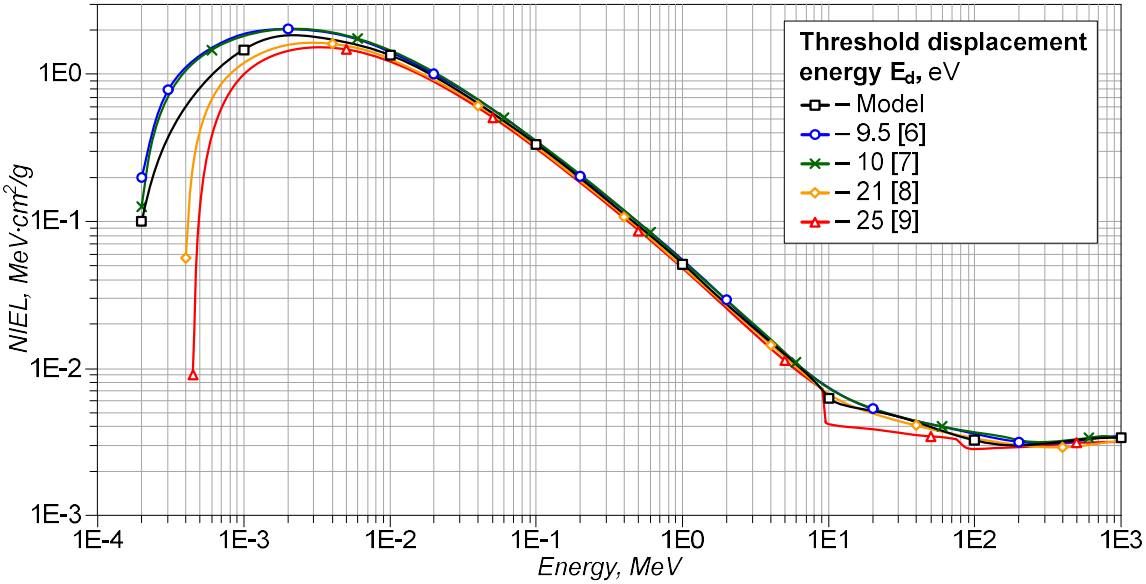

Fig. 3. The dependence of non-ionizing energy loss on the proton energy

The obtained results fully agree with the data presented in the paper [10]. The total NIEL for GaAs is calculated by summing the contributions of each element weighted by its atomic fraction [11].

The simulation of the effect of a proton flux on the performance of a device structure of a dual-channel GaAs-HEMT is carried out. The results of the influence of the flux of protons with an energy of E = 2 keV at the temperature of T = 303 K are shown in Fig. 4.

Fig. 5 shows the graphs of the dependence of the drain current I_D (at V_G = 0 V and V_D = 1 V) and the cut-off voltage on the fluence of protons F with energy E = 2 keV. The parameters are expressed in relative units (the values without penetrating radiation are taken as 100 %).

It is shown that the effect of the proton fluence on the values of the drain current and cut-off voltage does not coincide in magnitude, however, starting from values of 10^{12} cm^{-2}, a significant deterioration in the operational parameters of the transistor is observed. So, at $F = 10^{12}$ cm^{-2}, the drain current and cut-off voltage are 0.357 mA and –0.757 V, respectively, and at $F = 5 \cdot 10^{12}$ cm^{-2} – I_D = 0.243 mA (decrease by 32.4 %) and V_{TH} = –0.698 V (7.8 %). The dependence of the drain current and cutoff voltage deviation obeys the linear law (approximation reliability R_2 = 0.993 for I_D and R_2 = 0.996 for V_{TH}).

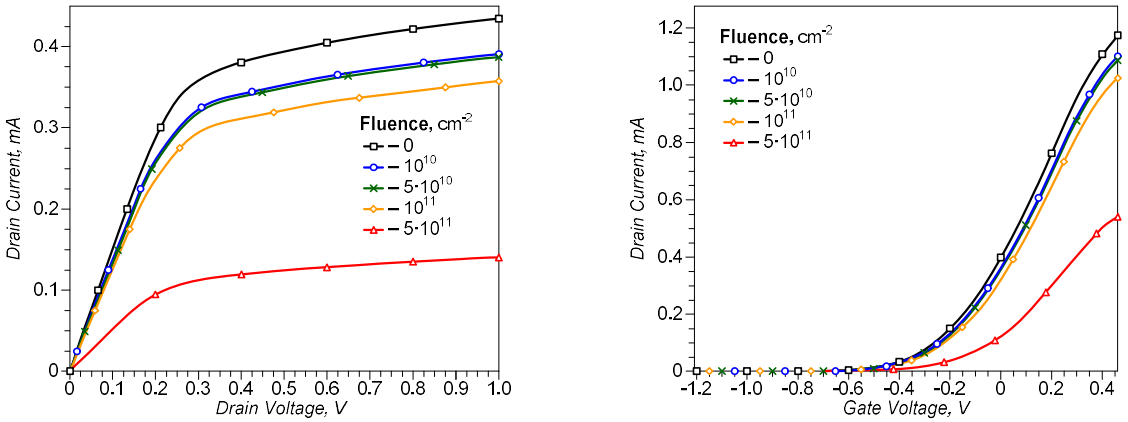

a *b*

Fig. 4. *I–V* characteristics with a change in the fluence of protons with an energy of $E = 20$ keV: *a* – Drain-Drain; *b* – Drain-Gate

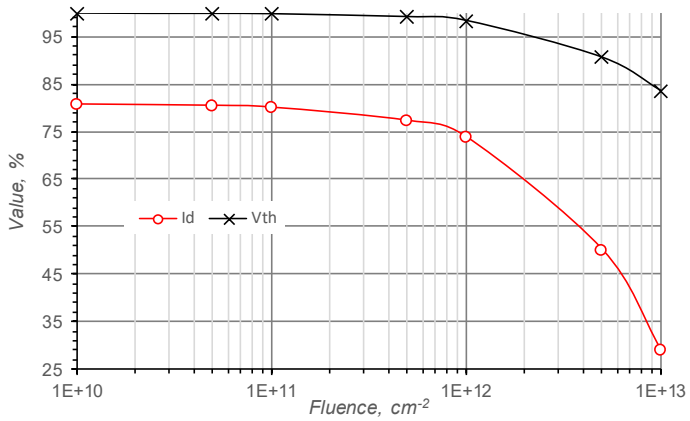

Fig. 5. Dependence of the parameters of dual-channel GaAs-HEMT on the proton fluence F (energy $E = 2$ keV, temperature $T = 303$ K)

Also noteworthy is the different effect of the proton flux on the drain current at different drain voltages (Fig. 6). At proton fluence $F < 5\times10^{12}$ cm^{-2}, its effect on the drain current is higher, the lower the drain voltage is. This is especially noticeable when the voltage at the drain is $V_D < 0.3$ V. At values of the proton fluence $F \geq 5\times10^{12}$ cm^{-2}, there is a shift in the voltage at the drain, at which the effect of radiation is the greatest. It is recommended to limit the use of low drain voltages at the circuit level to increase the radiation resistance of devices using the considered instrument structures.

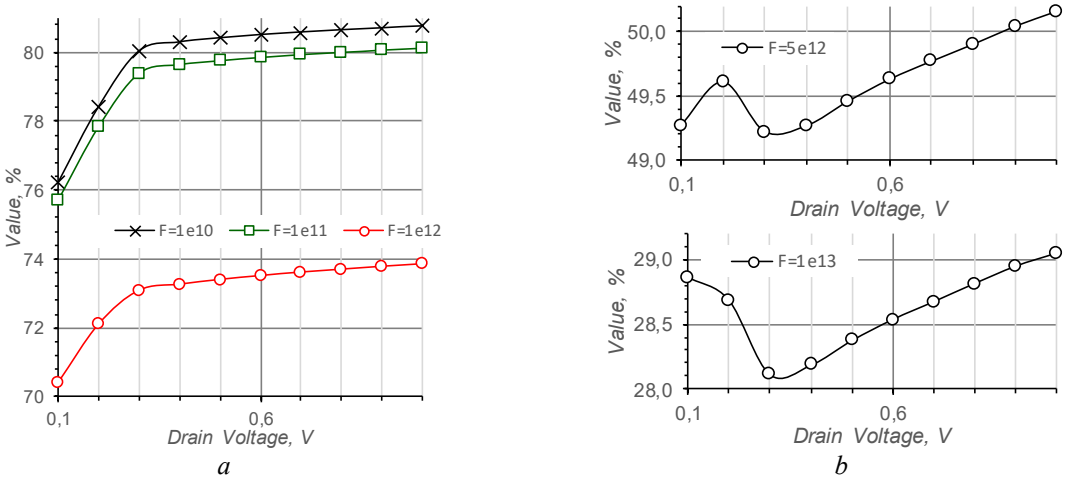

a *b*

Fig. 6. Drain current versus drain voltage at proton fluence values (energy $E = 2$ keV, temperature $T = 303$ K): *a* – $F < 5\cdot10^{12}$ cm^{-2}; *b* – $F \geq 5\cdot10^{12}$ cm^{-2}

Fig. 7 shows the graphs of the dependence of the drain current and cutoff voltage on the value of the proton energy E for the fluence $F = 10^{12}$ cm^{-2}.

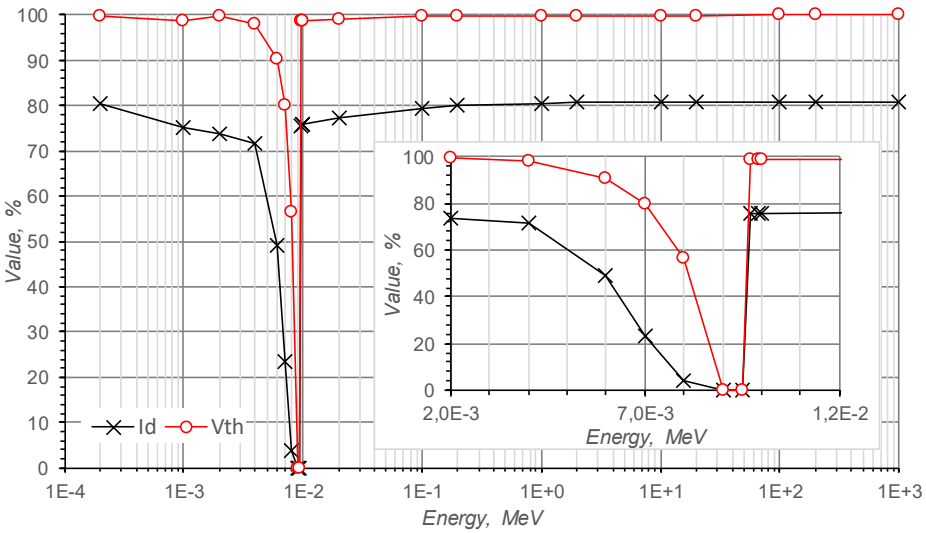

Fig. 7. Dependence of the parameters of a gallium arsenide field-effect transistor on the proton energy E (fluence $F = 5 \cdot 10^{10}$ cm^{-2}, temperature $T = 303$ K)

Based on the simulation results, it was found that the proton energy has the greatest effect on the electrical characteristics of a gallium arsenide field-effect transistor in the range from hundreds of eV to 100 keV, which correlates with the data presented in Fig. 3., with the exception of the energy range from 4 to 10 keV (i. e., when E is 6 keV higher than expected), at which there is a strong degradation of the electrical properties of the device structure up to a failure. At energies E greater than 1 MeV, the deviation of the parameters from the values without irradiation does not exceed 20 % for the drain current and 0.1 % for the cutoff voltage.

Conclusion

The model of the dependence of NIEL on the proton energy with different values of the threshold energy of defect formation for GaAs and AlGaAs, that are described in the literature and comply with the latest theoretical and experimental data, has been developed.

The analysis of the simulation results of the effect of the proton flux on the device structure of a dual-channel GaAs-HEMT allows us to reach the following conclusions: the proton fluence has a different effect on the drain current and cutoff voltage (the ratio of the degradation effect that increments $\Delta I_D / \Delta V_{TH}$ is not constant and varies from 4,07 to 6,19 for the cases under consideration); the energy of protons has the greatest influence in the region from hundreds of eV to 100 keV (up to the failure of the transistor). To increase the radiation resistance of devices using the considered device structures, it is recommended to provide protection from the proton flux in a narrow energy band (from 4 to 10 keV), and at the circuit level to limit the use of low voltage values at the drain.

References

1. Kulakov V.M., Ladygin E.A., Shahovcov V.I. The effect of penetrating radiation on electronic products. M. : Sov. Radio; 1980. (In Russ.)
2. Allam E.E., Inguimbert C., Meulenberg A., Jorio A., Zorkani I. Gamma non-ionizing energy loss:Comparison with the damage factor in silicon devices. Journal of Applied Physics. 2018;123 (095703):1-5.
3. Silvaco International. Victory Device : User Manual, Santa Clara : Silvaco; 2019.
4. Synopsys Inc. Sentaurus Device : User Guide, Version L-2016.03. San Jose : Synopsys; 2016.
5. Site of the SR-NIEL project [Electronic resource]. – Access mode: http://www.sr-niel.org/index.php.

6. Mansouri E. Studies on Radiation-induced Defects in InP/InAsP Nanowire-based Quantum Disc-in-wire Photodetectors. Halmstad : Halmstad University; 2018.
7. Pons D., Mooney P.M., Bourgoin J.C. Energy Dependence of Deep Level Introduction in Electron Irradiated GaAs. J. Appl. Phys. 1980;51:2038-2042.
8. Allam M.E., Inguimbert C., Nuns T., Meulenberg A., Jorio A., Zorkani I. Gamma and Electron NIEL Dependence of Irradiated GaAs. NSREC. 2016:7.
9. Claeys C., Simoen E. Radiation effects in Advanced Semiconductor Materials and Devices. Berlin: Springer; 2002.
10. Chen N., Gray S., Hernandez-Rivera E., Huang D., LeVan P. D., Gao F.. Computational simulation of threshold displacement energies of GaAs. Journal of Materials Research. 2017; 32(8):1555-1562.
11. Ziegler J.F., Biersack J. P., Littmark U. The Stopping and Range of Ions in Solids. Pergamon; 1985.

Authors' contribution

Lovshenko I.Yu. developed a model of the dependence of NIEL on the energy of protons, prepared the manuscript of the article.

Voronov A.Yu., Roshchenko P.S., Ternov R.E. performed computer calculations and processed the obtained data.

Galkin Ya. D., Kunts A. V. has simulated and took part in measuring device parameters.

Stempitsky V.R. and Bi Jinshun set a task for the study and analyzed the results.

Information about the authors

Lovshenko I.Yu., Head of R&D Lab. "CAD in Micro- and Nanoelectronics" of R&D Department of the Belarusian State University of Informatics and Radioelectronics.

Voronov A.Yu., Master's student at the Belarusian State University of Informatics and Radioelectronics.

Roshchenko P.S., Master's student, Electronic Engineer at R&D Lab. "CAD in Micro- and Nanoelectronics" of R&D Department of the Belarusian State University of Informatics and Radioelectronics.

Ternov R.E., Master's student at the Belarusian State University of Informatics and Radioelectronics.

Galkin Ya.D., Postgraduate student, Electronics Engineer at Electronic Methods and Experiment Means Laboratory of Research Institute for Nuclear Problems of Belarusian State University.

Kunts A.V., Postgraduate Student, Electronics Engineer at Electronic Methods and Experiment Means Laboratory of Research Institute for Nuclear Problems of Belarusian State University.

Stempitsky V.R., PhD., Associate Professor, Vice-Rector of Research and Development, Head of R&D Department, Scientific Supervisor of R&D Lab. "CAD in Micro- and Nanoelectronics".

Bi Jinshun – Professor at the Institute of Microelectronics of Chinese Academy of Sciences.

Address for correspondence

220013, Republic of Belarus,
Minsk, P. Brovka St., 6,
Belarusian State University
of Informatics and Radioelectronics;
e-mail: lovshenko@bsuir.by;
tel. +375-17-293-88-90;
Lovshenko Ivan Yur'evich

http://dx.doi.org/10.35596/1729-7648-2021-19-8-87-91

Original paper

UDC 621.37

INFLUENCE OF EXCHANGE-CORRELATION FUNCTIONAL ON THE STRUCTURAL AND ELECTRONIC PROPERTIES OF PERIODIC STRUCTURES WITH TRANSITION METAL ATOMS

MARYIA S. BARANAVA

Belarusian State University of Informatics and Radioelectronics (Minsk, Republic of Belarus)

Submitted 9 December 2021

Abstract. The influence of the exchange-correlation functional on the crystal fundamental property calculation is shown. CrGeTe3, compound with transition metals, was used for the simulation of structural and electronic properties. The calculations were carried out using such functional classes as LDA and GGA. It has been shown that LDA exhibits 0.4 % and 5.2 % overestimations of the lattice constants for *a* and *c*, respectively. GGA (OR) overestimates *a* by 0.58 % and underestimates *c* by 4 %. The influence of the Hubbard correction on the band gap was also investigated. If Ueff is applied to the *d*-electrons, then the band gap will decrease. This is due to the hybridization of the *p*-electrons of the chalcogen and the *d*-electrons of the transition metal. Thus, GGA demonstrates better agreement with the experiment. The convergence of the calculation of the total energy with a change in the *k*-points and the cutoff energy were also investigated.

Keywords: exchange-correlation functional, DFT, VASP, GGA, LDA.

Conflict of interests. The author declares no conflict of interests.

For citation. Baranava M.S. Influence of exchange-correlation functional on the structural and electronic properties of periodic structures with transition metal atoms. Doklady BGUIR. 2021; 19(8): 87-91.

Introduction

Most quantum mechanical simulation methods are *ab initio* methods, i. e. they do not require experimental parameters to obtain results. The main source of errors and inaccuracies in calculations by DFT methods is the exchange-correlation functional (Eex). The form of the exchange-correlation functional is determined by the approximation that is used to take this component into account. The local density approximation (LDA), the generalized gradient approximation (GGA), and other approaches, which are used in DFT (Density Functional Theory), have their drawbacks and are sources of errors. This leads to the need of verifying the simulation results for each specific compound.

The validity of the calculations by the DFT methods, i. e., the approximations used, can be checked by comparing the structural and electronic properties obtained in quantum mechanical calculations and the data obtained from experiments.

DFT functional for structure parameters

There are two main methods of accounting for E_{ex} such as the LDA and the GGA. The difference between the methods lies in the fact that in the second case, the dependence of the exchange and correlation energies on the gradient of the electron density is taken into account. Based on these methods, the corresponding classes of functionals have been developed.

Structural properties, in particular the parameters of the space lattice, depend on the choice of the pseudopotential. We performed the relaxation procedure for bulk $CrGeTe_3$ using four types of pseudopotentials (Tab. 1). In particular, from the class of GGA functionals, we used Perdew–Wang 91 (91) [1], PBE-sol (PS) [2], and optPBE [3]. The simulation results are presented in Tab. 1. All calculations were performed in the VASP software package.

Table 1. Structural properties of $CrGeTe_3$

Lattice constant	LDA	GGA (91)	GGA (OR)	GGA (PS)	Experiment
a	6.8546	6.9059	6.8660	6.7885	6.8263 [4], 6.820 [5]
c	21.6085	18.9652	19.7164	15.1656	20.5314 [4], 20.371 [5]

According to the results, the best agreement with experiment is obtained by the functionals GGA (OR). The LDA exhibits 0.4 % and 5.2 % overestimations of the lattice constants for *a* and *c*, respectively. GGA (OR) overestimates *a* by 0.58 % and underestimates *c* by 4 %.

DFT functional for electronic calculation

Classical LDA and GGA functionals often underestimate the band gap [6]. To overcome the difficulties that arise, new classes of functionals such as meta-GGA, hybrid, and also a method that introduces an additional correction (DFT+U) have been developed. However, hybrid functionals and functionals from the meta-GGA class require significant computing resources for all its efficiency. For example, Borlido and al. [7] provides a comparison of the average of the estimated time. Thus, meta-GGA, mBJ, and hybrid functionals are 5, 10–50, and 100 or more times slower than GGA.

DFT+U is a computationally simpler method. An additional correction for strongly correlated electrons, which takes into account the single-site Coulomb interaction, is used in framework ones. The rest of the electrons are described by the classical DFT functional. Within the framework of this method, two parameters are introduced. The first one (U) characterizes the local Coulomb interaction, and the second one (J) is a characteristic of the exchange interaction. The sum of these parameters is called "the effective Hubbard coefficient (U_{eff})". U_{eff} can be calculated using the *ab initio* simulation [8, 9]. However, U_{eff} values are usually obtained semi-empirically by comparison with the experimental band gap [10, 11]. The semiempirical technique allows one to avoid significant computational costs for calculating U_{eff} from the first principles.

We performed calculations of electronic properties and energy band diagrams for the LDA (U) and GGA (U) functionals (Fig 1). GGA, quite expectedly, gives a larger bandgap than LDA. This amounts to 0.20 and 0.30 eV, respectively. The experimental value is 0.38 eV [12]. Both functionals underestimate the band gap.

The obtained data for functionals with Hubbard correction differs from the expected ones. We got a lower value than for classical functionals. GGA+U demonstrates 0.16 eV and LDA + U gives a completely metallic type of conductivity. The Hubbard coefficient was 5 eV and was used for *d*-electrons of chromium. The same results for $CrGeTe_3$ were obtained by the authors in the work [13].

Other research groups obtained similar results as well. Boukhvalov et al. [14] noted that a large Hubbard coefficient decreases *3d-2p* hybridization in $BiMnO_3$. Therefore, it affects the characteristics of the Mn-O chemical bond (bond length and angle). $CrGeTe_3$ has a similar structure to $BiMnO_3$. A transition metal (in our case Cr, in [14] work it is Mn) with a valence *d* shell is surrounded by six atoms with a valence *p* shell (in our work it is Te, in [14] work it is O).

All this leads to hybridization of the *p*- and *d*- orbitals and the formation of a covalent bond. Usually, the Hubbard parameter is added only for *d*- and *f*-electrons. Thus, in $CrGeTe_3$, the *d*-orbitals are shifted, like $BiMnO_3$. The energy of *p*-electrons remains unchanged. This leads to the distortion

of the octahedral environment of Cr in $CrGeTe_3$ or Mn in $BiMnO_3$. A decrease of the band gap with an increase of the Hubbrad coefficient in TiO_2 [11] has been observed.

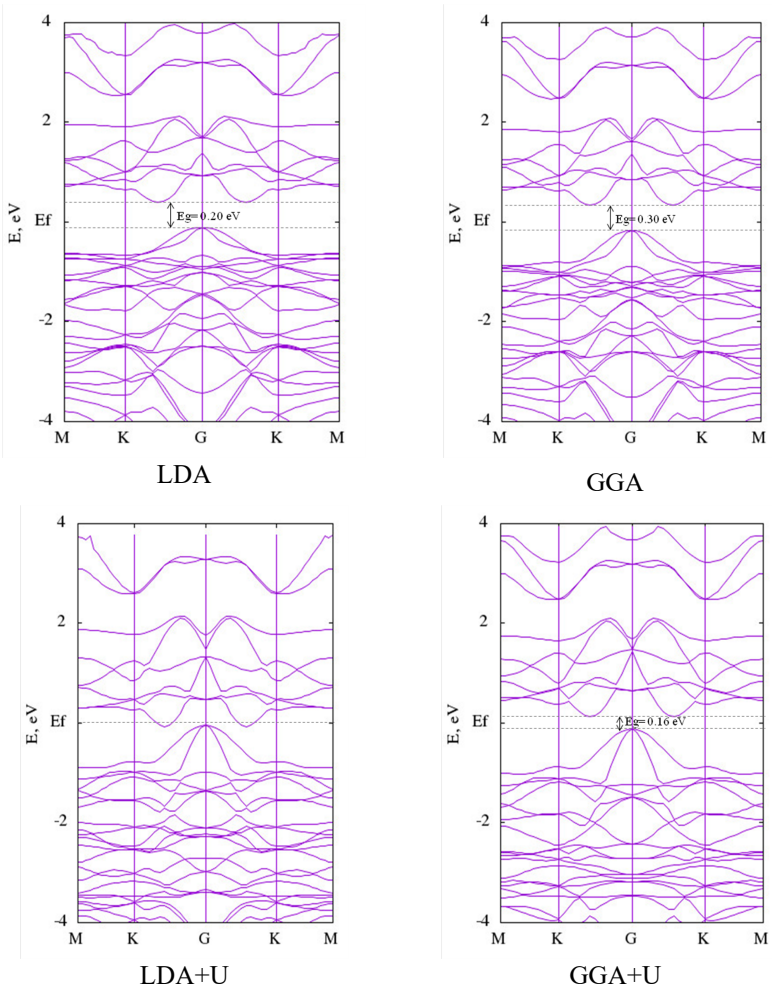

Fig. 1. Band structure of $CrGeTe_3$ obtained by different functionals

Cutoff energy and *k*-points

The exchange correlation functional is the only approximation in the DFT. However, the Kohn–Sham equations are a system of coupled, nonlinear, and partial differential equations. These equations are solved numerically using additional approximations. One of such approaches is the Born-Opergeimer approximation, which allows to separate the electrons of an atom into core (inner electron shell) and valence electrons (outer electron shell). Thus, the inner shell can be described by an effective pseudopotential, which is calculated by the ab initio methods once and forms a database of such pseudopotentials. The effective method of plane waves is used to solve the Kohn–Sham equations describing the wave functions of valence electrons [15].

The cutoff energy (E_{cut}) controls the completeness of the base set of plane waves. An increase in the cutoff energy leads to an increase in the calculation accuracy. However, the number of plane waves can become so large as to be computationally incredibly expensive. Thus, a trade-off has to be found between the accuracy, which is influenced by the cutoff energy, and the computational cost.

We calculated the dependence of the total energy of the system on the completeness of the basis set (cutoff energy). The calculation results are shown in Fig. 2, *a*. It was found that saturation occurs at 250 eV and above, i. e. the relative error between the obtained values does not exceed 2 %.

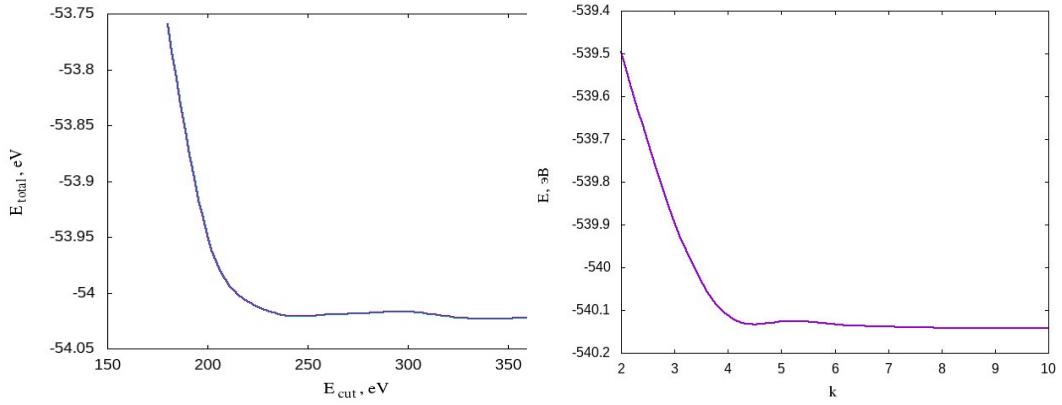

a *b*

Fig. 2. The dependence of the total energy on the cutoff energy (*a*) and dependence of the total energy on the *k*-points mesh (*b*)

The efficiency of quantum-mechanical calculations by DFT methods is determined, among other things, as a set of special points of reciprocal space (*k*-points). The number of *k*-points strongly affects the computational resources spent. Too many can lead to the fact that the time is too large or there is not enough computing power. On the other hand, setting a small set of *k*-points can lead to computational errors. *k*-points are specified to define Bloch vectors. This should be an optimal set of interpolation points of the Fourier coefficients for the expansion of the Kohn-Sham wave functions in the basis of plane waves. The optimal number of *k*-points was determined by test calculations. Fig. 2, *b* shows the dependence of the total energy of the system on a set of $n \times n \times 2$ ($n = 1, 2 \ldots 8$) *k*-points for the same atomic system. According to the graph shown in Fig. 2, the optimal set, i. e., which will allow obtaining sufficient accuracy with adequate computing resources, has a set of 8.

Conclusion

The article presented the investigation of quantum mechanical simulation parameter effects on the reliability of the results. The simulation results were compared with the known experimental data. The influence of the functional choice on the structural and electronic properties is established. Convergence tests were performed. This helped to determine the optimal set of *k*-points and establish an effective value of the cutoff energy. Thus, the reliability of the results of the CrGeTe3 simulation of the fundamental properties in the framework of the theory of the electron density functional has been confirmed.

References

1. Perdew J.P., Wang Y. Accurate and simple analytic representation of the electron-gas correlation energy. *Phys. Rev. B,* 1992;45:13244.
2. Perdew J.P., Ruzsinszky A., Csonka G.I., Vydrov O.A., Scuseria G.E., Constantin L.A., Zhou X., Burke K. Restoring the Density-Gradient Expansion for Exchange in Solids and Surfaces. *Phys. Rev. Lett.* 2008;100:136406.
3. Klimeš J., Bowler D.R., Michaelides A. Chemical accuracy for the van der Waals density functional. *J. Phys.: Cond. Matt.* 2010;22:022201.
4. Liu Yu, Petrovic C. Critical behavior of quasi-two-dimensional semiconducting ferromagnet $CrGeTe_3$, *Phys. Rev. B.* 2017;96:054406.
5. Carteaux V., Ouvrard G., Grenier J.C., Laligant Y. Magnetic structure of the new layered ferromagnetic chromium hexatellurosilicate $Cr_2Si_2Te_6$. J. *Magn. Magn. Mater.* 1991;94:127-133.
6. Tolba S.A., Gameel K.M., Ali B.A., Almossalami H.A., Allam N.K. The DFT+ U: Approaches, accuracy, and applications. *Density Functional Calculations-Recent Progresses of Theory and Application*. 2018:3-30.
7. Borlido P., Schmidt J., Huran A.W. Exchange-correlation functionals for band gaps of solids: benchmark, reparametrization and machine learning. *npj Comput. Mater.* 2020;6:96.
8. Giannozzi P., Baroni S., Bonini N., Calandra M., Car R., Cavazzoni C. and Wentzcovitch R.M. Quantum espresso: a modular and open-source software project for quantum simulations of materials. *J. Phys. Condens. Matter.* 2009;39:395502.

9. Cococcioni M., de Gironcoli S. A linear response approach to the calculation of the effective interaction parameters in the LDA+U method. *Physical Review B*. 2004;71:035105.
10. Himmetoglu B., Floris A., De Gironcoli S., Cococcioni M. Hubbard-corrected DFT energy functionals: The LDA+U description of correlated systems. *Int. J. Quant. Chem*. 2014:14-49.
11. Cococcioni M. The LDA+ U approach: a simple Hubbard correction for correlated ground states. *Correlated Electrons: From Models to Materials Modeling and Simulation* 2. 2012.
12. Li Y.F., Wang W., Guo W., Gu C. Y., Sun H. Y., He L., Zhou J.,Gu Z.B., Nie Y.F., Pan X., Q.Li Y.F. Electronic structure of ferromagnetic semiconductor $CrGeTe_3$ by angle-resolved photoemission spectroscopy. *Physical Review B* 98. 2018;12:125127.
13. Guido M., Calandra M., Polini M. Electronic structure and magnetic properties of few-layer $Cr_2Ge_2Te_6$: the key role of nonlocal electron–electron interaction effects. *2D Materials* 6. 2019;4:045042.
14. Boukhvalov D.W., Solovyev I.V. Defects of the crystal structure and Jahn-Teller distortion in BiMnO 3. *Physical Review B* 82. 2010;24:245101.
15. Pickett Warren E. Pseudopotential methods in condensed matter applications. *Computer Physics Reports* 9. 1989;3:115-197.

Information about the authors

Baranava M.S., Researcher at R&D Lab. 4.4 “Computer-Aided Design of Micro- and Nanoelectronic Systems” at the Belarusian State University of Informatics and Radioelectronics.

Address for correspondence

220013, Republic of Belarus,
Minsk, P. Brovka St., 6,
Belarusian State University
of Informatics and Radioelectronics;
e-mail: baranova@bsuir.by;
tel. +372-17-293-88-90;
Baranava Maryia Sergeevna

http://dx.doi.org/10.35596/1729-7648-2021-19-8-92-98

Original paper

UDC 537.9

FIRST-PRINCIPLES STUDY OF STABILITY AND ELECTRONIC PROPERTIES OF SINGLE-ELEMENT 2D MATERIALS

DZMITRY C. HVAZDOUSKI

Belarusian State University of Informatics and Radioelectronics (Minsk, Republic of Belarus)

Submitted 9 December 2021

Abstract. We have estimated stability of single-element 2D materials (C_2, N_2, Si_2, P_2, Ge_2, As_2, Sn_2, Sb_2, Pb_2, and Bi_2) by *ab initio* calculations. The calculations of structural and mechanical properties of 2D materials were performed using the VASP software package. The results of calculations of stiffness tensors, Young's modulus, and Poisson's ratios show that all studied single-element 2D materials are mechanically stable. Dynamic stability was investigated by calculating the phonon dispersion of the materials using the finite displacement method. Only Pb_2 has imaginary modes in the phonon dispersion curves and therefore it has dynamic unstable structure at low temperatures. The analysis of the band structures indicates the presence of insulators (N_2), semiconductors (P_2, As_2, Bi_2, Sb_2), semimetals, and metals among the studied group of single-element 2D materials.

Keywords: 2D material, ab initio, elastic constants, phonon dispersion, band structure.

Conflict of interests. The author declares no conflict of interests.

Gratitude. This work was supported by the grant 3.02.3 of Belarusian National Scientific Research Program "Convergence-2025" and the grant of The Belarusian Republican Foundation for Fundamental Research for young scientists "Science M - 2021" (contract № F21M-122). Computing cluster of BSUIR was used for computer modeling.

For citation. Hvazdouski D.C. First-principles study of stability and electronic properties of single-element 2D materials. Doklady BGUIR. 2021; 19(8): 92-98.

Introduction

Atomically thin two-dimensional (2D) materials have made their way to the forefront of several research areas including batteries, electrocatalysis, electronics, and photonics [1]. This development has been prompted by easily tunable properties of atomically thin crystals. Recently, the concepts of horizontal [2] and vertical [3] 2D heterostructures have appeared, it provides new possibilities to create materials with special electrophysical properties.

So far more than fifty compounds have been synthesized or exfoliated as single layers. These include the well-known single-elemental crystals and their ligand functionalized derivatives, transition metal dichalcogenides, transition metal carbides and -nitrides, group III–V semiconductors and insulators, transition metal halides, post-transition metal chalcogenides, and organic-inorganic hybrid perovskites.

A common feature of 2D materials is that they are formed from bulk materials with strong in-plane interatomic bonds and weak van der Waals (vdW) interaction between layers. It allows them to delaminate into atomically thin layers that can be investigated separately.

An important task is to determine the stability of two-dimensional materials using a numerical experiment, in particular, using the *ab initio* methods, it is much cheaper than a physical one. There is a possibility to simulate conditions that cannot be created in the laboratory in the course of a numerical experiment. Therefore, the material over a wide range of characteristics can be investigated. Synthesized materials must simultaneously satisfy thermodynamic, mechanical, dynamic, and thermal stability.

First-principles calculations are playing an increasingly important role in the search for new materials with required properties and functionalities. First-principles calculations are comparable with the experiments in terms of accuracy and greatly surpass them in terms of speed and cost through the continuous increase of computing power and significant advancements of theoretical methods and numerical algorithms. Structural, thermal, and electronic properties of 2D materials have been an insufficiently explored area of material science and, in the last decade, the experimental data has been augmented by an explosion of the computational data obtained from first-principles calculations. Density functional theory (DFT) methods are quite reliable for ground state properties such as structural and thermodynamic properties. They are generally not quantitatively accurate for excited state properties such as electronic band structures and optical absorption spectra.

In this work we performed a series of *ab initio* calculations to investigate the stability and electronic properties of single-elemental 2D materials previously unknown and potentially synthesizable monolayers.

Methods of calculation

Calculations of the total energy and electronic structure of the materials under study were performed using the VASP software package [4]. The electron-ion interaction was described using the projection augmented wave (PAW) method, and exchange correlation energy (XC) was taken into account using the GGA functional in the form of a PBE potential [5]. For the basis of plane waves, a cutoff energy of 450 eV was taken. To avoid the influence of wave functions on each other, arising from the translation of cells in a plane model of 2D systems, periodic plates of single-element 2D materials were separated by a 15 Å-thick vacuum layer along the crystallographic direction "*c*". The nonbonding van der Waals (vdW) interaction between atoms is taken into account using the semiempirical Green's dispersion correction scheme with Becke and Johnson's corrections [6] named "DFT-D3(BJ)". It is known that the studied monolayers of Si, Ge, and Sn don't possess spin polarization (they are nonmagnetic materials) and further calculations were performed without taking into account the spin polarization. The Bloch vectors of the first Brillouin zone were carried out using the *k*-point sampling. Self-consistent calculations were carried out with *k*-point grids generated automatically by the Monkhorst–Pack scheme with inverse spatial resolution of $2\pi \cdot 0.03$ Å^{-1}. Structural relaxation of the geometry and structural parameters of the primary unit cells were carried out until the residual force per atom became less than 0.001 eV/Å.

For a two-dimensional crystal, the stiffness tensor in the plane C_{ij} (i, j = 1, 2, 6) can be obtained by the following formula:

$$E_s = \frac{1}{2}C_{11}\varepsilon_{xx}^2 + \frac{1}{2}C_{22}\varepsilon_{yy}^2 + C_{12}\varepsilon_{xx}\varepsilon_{yy} + 2C_{66}\varepsilon_{xy}^2, \quad (1)$$

where ε is the tensile/compressive strain, which is defined as:

$$\varepsilon = \frac{a - a_0}{a}, \quad (2)$$

where a and a_0 are the lattice constants of the deformed and undeformed crystal, respectively.

To calculate the elasticity constants, the $E_s(\varepsilon)$ function was investigated in the deformation range of $-1.5\ \% \le \varepsilon \le 1.5\ \%$ with a step of 0.5 %. The elasticity constants C_{ij} were obtained by fitting a second-order polynomial of the total energy change function of the system depending on the applied deformation. Post-processing of the calculated data was carried out the VASPKIT code [7].

Dynamical stability of the 2D materials has been defined by phonon dispersion which is evaluated by the finite displacement method realized in the Phonopy program [8]. We have utilized a 5×5×1 supercell for 2D structures and the atomic displacement distance of 0.01 Å. Force constants

based on the forces on atoms were calculated using the POSCAR-{number} files to VASP calculations. Then a part of dynamical matrix was built in the Phonopy program from the force constants. Phonon frequencies and eigenvectors are calculated from the dynamical matrices with the specified *q*-points.

Structure optimization of single-elemental 2D materials

Configurations of potential single-element two-dimensional materials based on 10 chemical elements were proposed. For each of the chemical elements, 5 configurations with a hexagonal type of crystal lattice were proposed (Fig. 1).

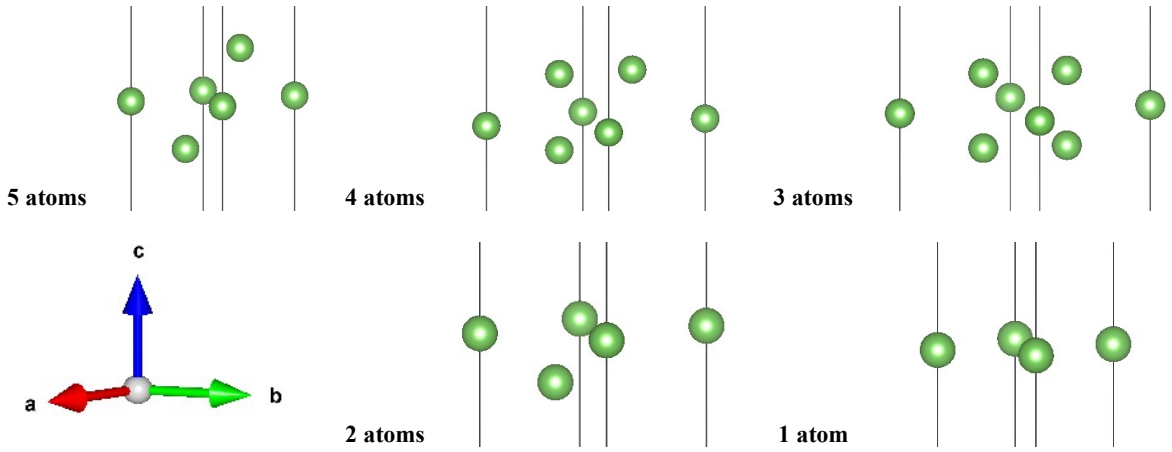

Fig. 1. Configurations of potential single-element 2D materials with a hexagonal lattice type

Structural optimization of the these configurations has been carried out. Based on the obtained values of the total energies of the systems (Tab. 1), it was concluded that configurations of two atoms are energetically favorable for the 2D systems under study. Thus, further calculations of stability and electronic properties were carried out for 2D systems with unit cells of two atoms.

Table 1. Values of total energies of systems for different single-element 2D material configurations

Atoms in a cell	Total energy of cell, eV/atom									
	As	Bi	C	Ge	N	P	Pb	Sb	Si	Sn
1	–4.05	–3.49	–5.33	–3.87	–4.24	–3.85	–3.19	–3.65	–3.98	–3.42
2	–4.87	–4.01	–9.31	–4.59	–6.76	–5.57	–3.66	–4.28	–4.97	–3.88
3	–4.54	–3.91	–6.32	–4.20	–5.11	–5.26	–1.15	–4.11	–4.87	–3.71
4	–4.45	–3.60	–9.11	–4.32	–4.77	–5.07	–3.13	–4.02	–4.56	–3.76
5	–4.58	–3.94	–8.22	–4.28	–4.72	–5.01	–3.39	–4.13	–4.77	–3.64

The calculated total energies E_{tot} and lattice constants "*a*" of all studied 2D systems after structural relaxation are listed in Tab. 2.

Table 2. Structural properties of single-element 2D materials

Parameter		Single-element 2D material									
		C_2	N_2	Si_2	P_2	Ge_2	As_2	Sn_2	Sb_2	Pb_2	Bi_2
a, Å	LDA	2.45	2.29	3.83	3.21	3.96	3.53	4.56	4.02	3.55	4.29
	PBE	2.46	2.29	3.86	3.25	4.02	3.59	4.65	4.08	3.62	4.36
	Ref. [9]	2.46	–	3.88	–	4.02	–	4.66	–	–	–
E_{tot}, eV	LDA	–20.18	–13.37	–10.41	–11.84	–9.16	–10.46	–7.79	–9.13	–7.93	–8.58
	PBE	–18.63	–13.52	–9.95	–11.15	–8.39	–9.74	–7.13	–8.57	–7.23	–7.99

The presented results of calculations with a PBE exchange correlation functional are in good agreement with previous theoretical investigations. The calculated value of lattice constant "*a*" has PBE only 0.8 % smaller than the theoretical value, which points it out as a good approach of an exchange

correlation energy functional in order to calculate the lattice parameters. The observed discrepancy of LDA and PBE of our results compared to the experimental values is a well-established fact.

Stability of single-elemental 2D materials

Dynamic stability reflects the ability of a material to maintain its shape under mechanical perturbations of the structure, which can be determined by calculating the phonon spectrum of the material using the finite displacement method [10] or the density functional perturbation theory. If imaginary modes exist in the phonon spectra, this means that the material, after a slight distortion of the crystal lattice, will undergo reconstructive or martensitic phase transformations. Thermal stability reflects the resistance to the degradation at high temperatures, which can be estimated by performing *ab initio* simulations using molecular dynamics methods. The thermodynamic stability of two-dimensional materials is characterized by the formation energy ΔE_f. It is defined as the difference between the energies of the investigated 2D material and its pure elementary components. A negative value of ΔE_f for a material indicates its thermodynamic stability. In other words, any processes that lead to transformation or decomposition of the material are unacceptable or kinetically slow. In this study, only dynamic and mechanical stability were used as two stability criteria for the selection of potential 2D materials. Thus, if a 2D material is found to be stable and has a band gap unlike zero eV, this means, that it may be a new potential two-dimensional semiconductor.

In this work, only the phonon dispersion and elastic constants of two-dimensional materials were calculated. In this case, it is possible to achieve a better ratio between the expenditure of computer time and the deviation of the simulation results from the experimental data.

According to the Born – Huang criteria [11], a mechanically stable 2D sheet must match the requirements of $C_{11} > 0$ and $C_{11} > |C_{12}|$. Then Young's modulus Y and Poisson's ratios ν for a two-dimensional material can be defined as:

$$Y(x) = \frac{C_{11}C_{22} - C_{12}^2}{C_{22}}, \quad Y(y) = \frac{C_{11}C_{22} - C_{12}^2}{C_{11}}, \tag{3}$$

$$\nu(x) = \frac{C_{12}}{C_{22}}, \quad \nu(y) = \frac{C_{12}}{C_{11}}. \tag{4}$$

where x and y correspond to the lattice directions a and b, respectively.

The mechanical properties of single-element 2D materials calculated using *ab initio* methods and presented in Tab. 3. Authors [9] calculated the planar elastic stiffness coefficients C_{11}, C_{22}, and C_{12} using a central difference approximation to the derivative of the stress tensor for the studied materials. The calculated Young's modulus is in good agreement with the previous theoretical calculations for silicene (61.33 N/m), germanene (42.05 N/m), and stanene (24.46 N/m) [12]. According to the Born–Huang criteria, it was found that all studied single-element 2D materials are mechanically stable.

Table 3. Mechanical properties of single-element 2D materials

Parameter		Single-element 2D material									
		C_2	N_2	Si_2	Ge_2	Sn_2	Pb_2	P_2	As_2	Sb_2	Bi_2
This work	C_{11}, N/m	343.07	269.68	69.28	49.78	27.04	15.62	77.73	52.91	32.89	25.04
	C_{12}, N/m	78.82	27.31	22.19	17.69	10.99	5.65	8.73	9.57	5.74	6.27
	ν	0.23	0.11	0.32	0.35	0.41	0.36	0.11	0.18	0.17	0.25
	Y, N/m	324.96	266.92	62.17	43.49	22.57	13.58	76.75	51.16	31.89	23.47
Ref. [9]	C_{11}, N/m	345.65	–	66.62	48.87	28.56	–	77.37	52.51	32.61	24.49
	C_{12}, N/m	70.61	–	21.51	16.22	11.41	–	7.95	8.50	6.23	6.05

A crystal will be dynamically stable, if its potential energy always increases against any combinations of atomic displacements (all phonons have real and positive frequencies). However under virtual thermodynamic conditions, imaginary frequency or negative eigenvalue can appear. This indicates dynamical instability of the 2D crystal phase. The calculated phonon dispersions of single-element 2D materials are shown in Fig. 2.

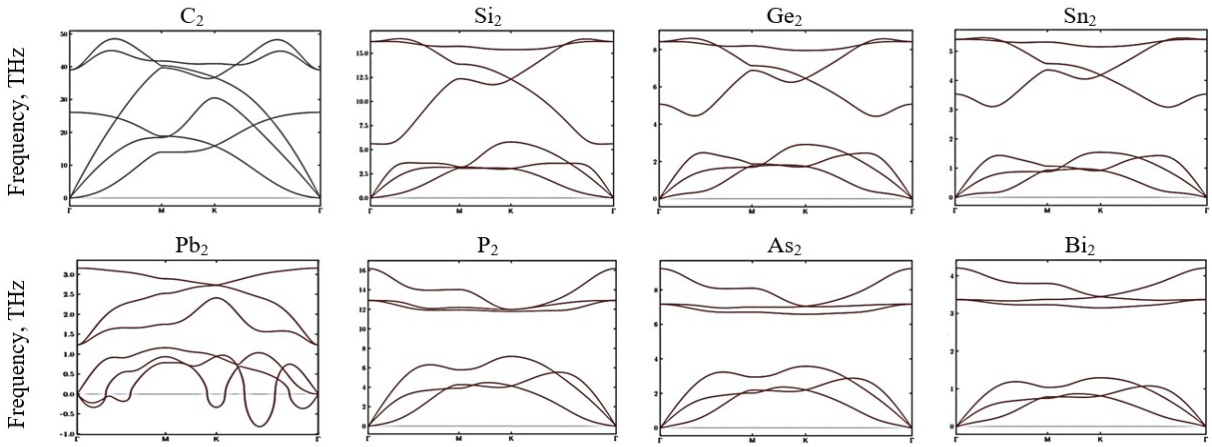

Fig. 2. Phonon dispersions of single-element 2D materials

Almost all single-element 2D materials do not have imaginary frequencies in the phonon dispersion curves and they can be viewed as dynamically stable structures. However, Pb_2 has imaginary frequencies (negative values) in the vicinity of the Γ, M, and K points indicating instability against phonon excitation. This indicates that Pb_2 is unstable at low temperatures. The imaginary frequencies can arise from the numerical inaccuracy because of the limited supercell size.

For a more accurate analysis of the stability of materials, it is planned to carry out a number of calculations based on the theory of perturbations of the density functional and molecular dynamics to determine the thermal stability of two-dimensional materials.

Electronic properties of single-elemental 2D materials

Electronic band structures are calculated along the high symmetry paths of 2D Bravais lattices. The band energies are computed within DFT method using three different XC-functionals: LDA, PBE, and HSE06. The electron density is determined self-consistency on a uniform *k*-point grid of density 10.0/ $Å^{-1}$. From this density, the PBE band structure is computed non-selfconsistency at 200 *k*-points distributed along the band path. The band structure is calculated non-selfconsistently using the range-separated hybrid functional HSE06 on top of a PBE calculation with *k*-point density 12.0/ $Å^{-1}$ and 600 eV plane wave cutoff.

Tab. 3 shows the results of calculating the electronic properties of single-element 2D materials using LDA, PBE, and HSE06 XC-functionals.

Table 3. Electronic properties of single-element 2D materials

Single-element 2D material	Band gap, eV			Band Character	Location of valence band maximum			Location of conduction band minimum		
	LDA	PBE-D3(BJ)	HSE06-D3(BJ)							
C_2	0.000	0.000	0.000	Semimetallic	0.333	0.333	0.000	0.333	0.333	0.000
N_2	3.845	3.878	5.809	Indirect gap	0.144	0.144	0.000	0.329	0.000	0.000
Si_2	0.000	0.000	0.000	Semimetallic	0.333	0.333	0.000	0.333	0.333	0.000
P_2	1.863	1.987	2.753	Indirect gap	0.000	0.000	0.000	0.362	0.000	0.000
Ge_2	0.000	0.000	0.000	Semimetallic	0.333	0.333	0.000	0.333	0.333	0.000
As_2	1.455	1.564	2.189	Indirect gap	0.000	0.000	0.000	0.313	0.000	0.000
Sn_2	0.000	0.000	0.000	Semimetallic	0.333	0.333	0.000	0.333	0.333	0.000
Sb_2	1.113	1.485	1.183	Indirect gap	0.000	0.000	0.000	0.310	0.000	0.000
Pb_2	–	–	–	Metallic	–	–	–	–	–	–
Bi_2	0.566	0.568	0.977	Direct gap	0.000	0.000	0.000	0.000	0.000	0.000

The band gap and the type of semiconductor were indicated for the studied compounds. The band gap of semiconductors is greatly underestimated when calculating the traditional density functional theory (DFT) with local or semilocal exchange correlation functionals. The results obtained may differ from the experimental values ones in the direction of underestimating the band gap due to the well-known difficulties arising in the framework of the DFT.

The calculated band structures of single-element 2D materials (As_2, C_2, Bi_2, N_2) with LDA, PBE, and HSE06 XC-functionals are presented in Fig. 3.

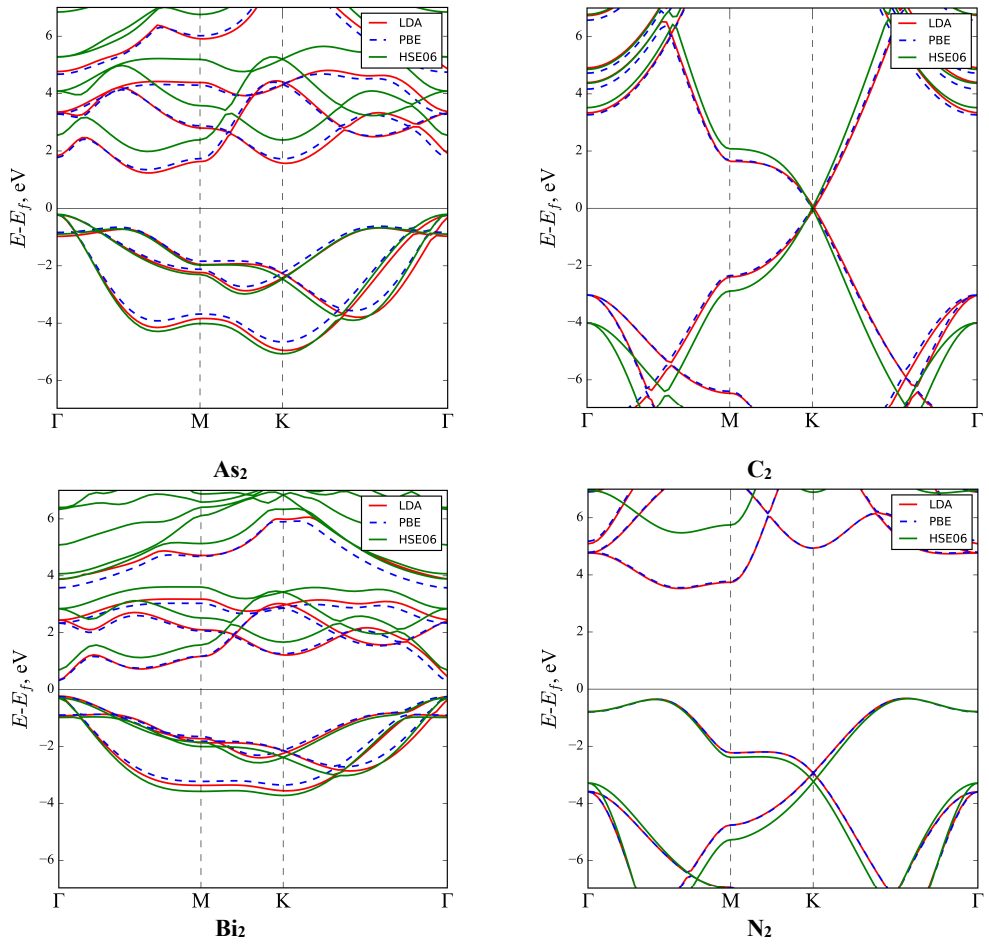

Fig. 3. Electronic band structures of single-element 2D materials

The band structures of the studied single-element 2D materials were obtained and according to which the type of conductivity was established. It was found that N_2 is indirect-gap insulator with a band gap of 5.809 eV. P_2, As_2, and Sb_2 are indirect-gap semiconductors with bandgaps of 2.753, 2.189, and 1.183 eV, respectively. Bi_2 is a direct-gap semiconductor with a band gap of 0.977 eV. C_2, Si_2, Ge_2, and Sn_2 are semimetals with direct transitions. Pb_2 is a 2D metal-type material (the Fermi level in this case crosses the conduction bands).

Conclusion

The results of *ab initio* calculations of mechanical properties in the present study are in good agreement with the previous theoretical calculations. It shows that all studied single-element 2D materials are mechanically stable. The calculated phonon properties of almost all 2D materials (except Pb_2) don't have imaginary frequencies in the phonon dispersion curves and they can be viewed as dynamically stable structures. Pb_2 is unstable at low temperatures. It is necessary to carry out additional calculations based on the molecular dynamics for a more accurate analysis of the stability of materials.

The analysis of band structures indicates the presence of insulators (N_2), semiconductors (P_2, As_2, Bi_2, Sb_2), semimetals, and metals among the studied group of single-element 2D materials. The results obtained quantitatively and qualitatively characterize the structural and electronic properties of crystal structures based on 2D materials. The results can be used in the development of methods for calculating the basic electrophysical parameters of promising devices for nanoelectronics and optoelectronics.

References

1. Ferrari A. C., Bonaccorso F., Fal'ko V., Novoselov K. S., Roche S., Bøggild P., Pugno N. Science and technology roadmap for graphene, related two-dimensional crystals, and hybrid systems. *Nanoscale.* 2015; 7(11): 4598-4810.
2. Huang C., Wu S., Sanchez A. M., Peters J. J. P., Beanland R., Ross J. S., Xu X. Lateral heterojunctions within monolayer $MoSe_2$-WSe_2 semiconductors. *Nature materials.* 2014; 13(12): 1096-1101.
3. Geim A. K., Grigorieva I. V. Van der Waals heterostructures. *Nature.* 2013; 499(7459): 419-425.
4. Kresse G., Furthmüller J. Efficiency of ab-initio total energy calculations for metals and semiconductors using a plane-wave basis set. *Computational materials science.* 1996; 6(1): 15-50.
5. Perdew J., Burke P., Ernzerhof M. Generalized Gradient Approximation Made Simple. *Physical review letters.* 1996; 77(18): 3865-3868.
6. Grimme S., Ehrlich S., Goerigk L. Effect of the damping function in dispersion corrected density functional theory. *Journal of computational chemistry.* 2011; 32(7): 1456-1465.
7. Wang V., Xu N., Liu J.-C., Tang G., Geng W.-T.VASPKIT: a user-friendly interface facilitating high-throughput computing and analysis using VASP code. *Computer Physics Communications*. 2021; 267: 108033.
8. Togo A., Tanaka I. First principles phonon calculations in materials science. *Scripta Materialia.* 2015; 108:1-5.
9. Haastrup S., Strange M., Pandey M., Deilmann T., Schmidt P. S., Hinsche N. F., ... Thygesen K. S. The Computational 2D Materials Database: high-throughput modeling and discovery of atomically thin crystals. *2D Materials*. 2018; 5(4): 042002.
10. Parlinski K., Li Z. Q., Kawazoe Y. First-principles determination of the soft mode in cubic ZrO_2. *Physical Review Letters.* 1997; 78(21): 4063.
11. Born M., Huang K. *Dynamic Theory of Crystal Lattice*. Clarendon; 1954.
12. John R., Merlin B. Theoretical investigation of structural, electronic, and mechanical properties of two dimensional C, Si, Ge, Sn. *Crystal Structure Theory and Applications.* 2016; 5(3): 43-55.

Information about the authors

Hvazdouski D.C., Researcher at R&D Lab. 4.4 "Computer-Aided Design of Micro- and Nanoelectronic Systems" of the Belarusian State University of Informatics and Radioelectronics.

Address for correspondence

220013, Republic of Belarus,
Minsk, P. Brovka St., 6,
Belarusian State University
of Informatics and Radioelectronics;
e-mail: gvozdovsky@bsuir.by;
tel. +375-17-293-88-90;
Hvazdouski Dzmitry Chaslavavich

This issue contains articles recommended for publication by the Program and Organizing Committees of the 19th International Workshop on New Approaches to High-Tech: Nano-Design, Technology, Computer Simulations (NDTCS-2021), held in Minsk from 28 to 29 October 2021.

PROGRAM COMMITTEE OF THE SYMPOSIUM

Co-Chairs:

Anatoly Belous, D.Sc., Prof., Cor.Mem. of NAS of Belarus, Deputy General Director of JSC "Integral" – Management Company of "Integral" Holding, Belarus.

Alexander Melker, D.Sc., Prof., Peter the Great Saint Petersburg Polytechnic University, Russia.

Vladimir Labunov, Academician of NAS of Belarus, D.Sc., Prof., Professor of Micro- and Nanoelectronics Department, Head of R&D Lab. "Integrated Micro- and Nanosystems", BSUIR, Belarus.

Members:

Aleksandr Nikitin, PhD., Assoc. Prof., Associate Professor of Department of Theoretical Physics and Heat Engineering, Yanka Kupala State University of Grodno, Belarus.

Alexander Danilyuk, PhD., Assoc. Prof., Associate Professor of Department of Micro- and Nanoelectronics, BSUIR, Belarus.

Alexander Gurskii, D.Sc., Prof., Professor of Information Security Department, BSUIR, Belarus.

Alexander Sigov, Academician of RAS, D.Sc., Prof., President of FSBEIHE "MIREA – Russian Technological University", Russia.

Anatoly Gulai, PhD., Assoc. Prof., Head of Intellectual and Mechatronic Systems Department, Belarusian National Technical University, Belarus.

Anna Krivosheeva, D.Sc., Leading Researcher of R&D Center "Nanoelectronics and Advanced Materials", BSUIR, Belarus.

Dmitri Migas, D.Sc., Prof., Head of Department of Micro- and Nanoelectronics, BSUIR, Belarus.

Hamit Topuz, D.Sc., Prof., Manager of Environmental & Energy Research Center, Head of Department of Natural Sciences, Engineering Faculty, Maltepe University, Turkey.

Hanna Bandarenka, PhD., Assoc. Prof., Head of R&D Lab. "Applied Plasmonics", BSUIR, Belarus.

Igor Abramov, D.Sc., Prof., Professor of Micro- and Nanoelectronics Department, Head of R&D Lab. "Physics of Micro- and Nanoelectronic Devices", BSUIR, Belarus.

Igor Vrublevsky, PhD., Assoc. Prof., Head of R&D Lab. "Materials and Components of Electronics and Superconducting Equipment", Associate Professor of Information Security Department, BSUIR, Belarus.

Jelena Tamuliene, PhD., Senior Researcher at Institute of Theoretical Physics and Astronomy, Physics Faculty, Vilnius University, Lithuania.

Matanat Mehrabova, D.Sc., Assoc. Prof., Leading Researcher, Institute of Radiation Problems of Azerbaijan National Academy of Sciences, Azerbaijan.

Miroslaw Najbuk, M.Sc., Leading Researcher, Computer Science Institute, University of Bialystok, Poland.

Nguyen Thanh Tung, PhD., Assoc. Prof., Vice Director of Institute of Materials Science, Vietnam Academy of Science and Technology, Vietnam.

Nikolai Gaponenko, D.Sc., Prof., Head of R&D Lab. "Nanophotonics", BSUIR, Belarus.

Roman Shamin, D.Sc., Prof., Director of Institute of Physics and Technology, RTU MIREA, Russia.

Sergei Lazarouk, D.Sc., Head of R&D Lab. "Electrochemical nano-structure materials", BSUIR, Belarus.

Serghej Prischepa, D.Sc., Prof., Professor of Information Security Department, BSUIR, Belarus.

Vazgen Melikyan, Cor.Mem. of NAS of Armenia, D.Sc., Prof., Director of Synopsys Armenia Educational Department, NASA Presidium Member, Armenia.

Victor Borisenko, D.Sc., Prof., Professor of Micro- and Nanoelectronics Department, Head of R&D Center "Nanoelectronics and Advanced Materials", BSUIR, Belarus.

Vladimir Borzdov, D.Sc., Prof., Head of Physical Electronics and Nano Technologies Department, Belarusian State University, Belarus.

Yuri Pisetsky, D.Sc., Prof., Dean of Joint Faculty of Information Technologies TUIT-BSUIR, Head of Department of Technologies of Mobile Communication, Tashkent University of Information Technologies named after Muhammad al-Khwarizmi, Uzbekistan.

Xuan-Tu Tran, PhD., Assoc. Prof. of Faculty of Electronics and Communications, Vietnam National University – University of Engineering and Technology, Vietnam.

ORGANIZING COMMITTEE OF THE SYMPOSIUM

Chair:

Vadim Bogush, D.Sc., Prof., Rector of Belarusian State University of Informatics and Radioelectronics (BSUIR), Belarus.

Stanislav Kudzh, D.Sc., Rector of FSBEIHE "MIREA – Russian Technological University", Russia.

Members:

Viktor Stempitsky, PhD., Assoc. Prof., Vice-Rector for R&D of Belarusian State University of Informatics and Radioelectronics (BSUIR), Scientific Supervisor of R&D Lab. "Computer-aided design of micro- and nanoelectronic systems", BSUIR, Belarus.

Ludmila Shichko, M.Sc., Deputy Head of R&D Department, BSUIR, Belarus.

Ivan Lovshenko, M.Sc., Head of R&D Lab. "Computer-aided design of micro- and nanoelectronic systems", BSUIR, Belarus.

Elena Bakunova, Head of Marketing and Science Communication Department, BSUIR, Belarus.

ORGANIZERS OF THE SYMPOSIUM

Belarusian State University of Informatics and Radioelectronics (BSUIR) was founded in 1964 as Minsk Radioengineering Institute. Today, it has become a large educational, scientific and innovation center in Belarus. BSUIR is the national coordinator of research on protection against inadvertent interference and on electromagnetic compatibility of radioelectronics including scientific, technical and organizational support of the State Radio Frequency Commission under the Security Council of the Republic of Belarus. The university comprises 8 faculties and 32 departments that are offering ca. 100 B.Sc., M.Sc., PhD. and postdoc programmes. In addition, there are the Institute of Information Technologies (staff retraining and professional skills upgrading courses), the Minsk Radioengineering College (vocational education training), and the Research and Development Department (RDI activities).

MIREA – Russian Technological University is one of the leaders in the field of training of highly qualified specialists for quickly developing knowledge-intensive branches of science and technology: telecommunications, information and computer technologies, automatic equipment, cybernetics, radio engineering and electronics, chemistry and biotechnologies. The University implements a unique system of training «higher education institution – base chair – base enterprise» which provides high efficiency of educational process and guarantees fast adaptation of graduates to real conditions of modern production environment. Today, MIREA – Russian Technological University has more than 50 base chairs at Research Institutes of the Russian Academy of Sciences, design offices and hi-tech enterprises of the Moscow region.

PARTNERS OF THE SYMPOSIUM

Make life good. LG Electronics and appliances feature innovative technology and sleek designs to suit your life and your style. LG Electronics focused on developing new innovations across the globe. We are committed to providing electronic products that help customers live better. To support this, we wish to continue bringing added value to the lives of consumers. We offer a wide range of products across areas including, TV & Home Entertainment, Kitchen, Laundry, Computers, Air Conditioning & Solar.

JSC "Integral" – Management Company of "Integral" Holding is the major manufacturer of electronic components in the Eastern Europe and provides (a full cycle of development and production of more than 3500 types of microcircuits and semiconductor devices; design standards up to 0.35 microns; a wide range of technological processes: basic CMOS, CMOS with built-in high-voltage units, radiation-resistant CMOS, options for bipolar processes, including radiation-resistant, BiCMOS, BiCDMOS, MOSFET processes for high-power high-speed and high-voltage transistors, etc.)